Ultrahigh Vacuum Studies of the Fundamental Interactions of Chemical Warfare Agents and Their Simulants with Amorphous Silica

Amanda Rose Wilmsmeyer

Dissertation submitted to the faculty of the Virginia Polytechnic Institute and State University in partial fulfillment of the requirements for the degree of

Doctor of Philosophy

In

Chemistry

John R. Morris, Chair

Louis A. Madsen

James M. Tanko

Brian M. Tissue

Edward F. Valeev

August 3, 2012

Blacksburg, VA

Keywords: surface chemistry, chemical warfare agent simulants, hydrogen bonding, ultrahigh vacuum, temperature programmed desorption, infrared spectroscopy

Ultrahigh Vacuum Studies of the Fundamental Interactions of Chemical Warfare Agents and Their Simulants with Amorphous Silica

Amanda Rose Wilmsmeyer

Abstract

Developing a fundamental understanding of the interactions of chemical warfare agents (CWAs) with surfaces is essential for the rational design of new sorbents, sensors, and decontamination strategies. The interactions of chemical warfare agent simulants, molecules which retain many of the same chemical or physical properties of the agent without the toxic effects, with amorphous silica were conducted to investigate how small changes in chemical structure affect the overall chemistry. Experiments investigating the surface chemistry of two classes of CWAs, nerve and blister agents, were performed in ultrahigh vacuum to provide a well-characterized system in the absence of background gases. Transmission infrared spectroscopy and temperature-programmed desorption techniques were used to learn about the adsorption mechanism and to measure the activation energy for desorption for each of the simulant studied. In the organophosphate series, the simulants diisopropyl methylphosphonate (DIMP), dimethyl methylphosphonate (DMMP), trimethyl phosphate (TMP), dimethyl chlorophosphate (DMCP), and methyl dichlorophosphate (MDCP) were all observed to interact with the silica surface through the formation of a hydrogen bond between the phosphoryl oxygen of the simulant and an isolated hydroxyl group on the surface. In the limit of zero coverage, and after defect effects were excluded, the activation energies for desorption were measured to be 57.9 ± 1, 54.5 ± 0.3, 52.4 ± 0.6, 48.4 ± 1, and 43.0 ± 0.8 kJ/mol for DIMP. DMMP, TMP, DMCP, and MDCP respectively. The adsorption strength was linearly correlated to the magnitude of the frequency shift of the ν(SiO-H) mode upon simulant adsorption. The interaction strength was also linearly correlated to the calculated negative charge on the phosphoryl oxygen, which is affected by the combined inductive effects of the simulants' different substituents. From the structure-function relationship provided by the simulant studies, the CWA, Sarin is predicted to adsorb to isolated hydroxyl groups of the silica surface via the phosphoryl oxygen with a strength of 53 kJ/mol. The interactions of two common mustard simulants, 2-chloroethyl ethyl sulfide (2-CEES) and methyl salicylate (MeS), with amorphous silica were also studied. 2-CEES was observed to adsorb to form two different types of hydrogen bonds with isolated hydroxyl groups, one via the S moiety and another via the Cl moiety. The desorption energy depends strongly on the simulant coverage, suggesting that each 2-CEES adsorbate forms two hydrogen bonds. MeS interacts with the surface via a single hydrogen bond through either its hydroxyl or carbonyl functionality. While the simulant work has allowed us to make predictions agent-surface interactions, actual experiments with the live agents need to be conducted to fully understand this chemistry. To this end, a new surface science instrument specifically designed for agent-surface experiments has been developed, constructed, and tested. The instrument, located at Edgewood Chemical Biological Center, now makes it possible to make direct comparisons between simulants and agents that will aid in choosing which simulants best model live agent chemistry for a given system. These fundamental studies will also contribute to the development of new agent detection and decontamination strategies.

Acknowledgements

My completion of graduate school would not have been possible without the support of family and friends every step of the way. First, I would like to thank my husband Kyle, for his daily encouragement, patience, and love. I always knew you were behind me in my pursuits and I am forever grateful for that. I would also like to thank my parents for always encouraging me to do my best and providing me with the confidence to do just that. My brother, Ryan, kept me laughing and always put a smile on my face. I am also thankful for the support of my friend Meghan Rodriguez. Even though we were states apart, we still went though this together, and being able to share the experience made it much more manageable.

The members of the Morris Group and other friends around the department made daily life of graduate school enjoyable. Josh Uzarksi, Dimitar Panayotov, and Wes Gordon taught me more than they probably realize and my success in graduate school began with their mentorship. Erin Davis, Jessica Lu, Will Alexander, Steve Burrows, Alec Wagner, Yafen Zhang, Tommy Rockhold, Josh Abelard, and Guanyu Wang all provided friendship and support in lab and I would not be the scientist I am today without all of their help.

I would also like to thank Dave Simmons and Darrell Link from the engineering machine shop for always allowing me to bounce ideas off of them and their expertise allowed me to do better science. Diego Troya has helped me tremendously in developing a more complete understanding of my research and collaborating with him has been a true pleasure. All of my committee members have been incredibly supportive throughout this journey and were always willing to offer additional support.

Finally, I would especially like to thank my advisor, John Morris. I could not have asked for a better advisor. He challenged me to work harder than I thought I could, but also encouraged me when I felt defeated. He has taught me how to become an excellent researcher and teacher and I thank him for always pushing me forward.

Table of Contents

List of Figures

List of Tables

Index of Acronyms

CH	Chlorohydrin
CWA	Chemical warfare agent
DFP	Diisopropyl fluorophosphate
DIMP	Diisopropyl methylphosphonate
DMCP	Dimethyl chlorophosphate
DMMP	Dimethyl methylphosphonate
DNA	Deoxyribonucleic acid
DPMP	Diphenyl methylphosphonate
FTIR	Fourier transform infrared
GA	Tabun; ethyl *N*,*N*-dimethyl phosphoramidocyanidate
GB	Sarin; isopropyl methylphosphonofluoridate
GCA	Glass capillary array
GD	Soman; pinacolyl methylphosphonofluoridate
HD	Sulfur mustard; bis (2-chloroethyl) sulfide
HV	High vacuum
IR	Infrared
KF	Quick connect
LN_2	Liquid nitrogen
MCT	Mercury-cadmium-telluride
MDCP	Methyl dichlorophosphate
MeS	Methyl salicylate
MMB	Methyl 2-methyl benzoate
MMP	Methyl methylphosphonate
MP2	Møller-Plesset
MPA	Methylphosphonic acid
PID	Proportional-integral-derivative

PW	Polanyi-Wigner
QC	Quantum chemical
RAIRS	Reflection Absorption InfraRed Spectroscopy
TC	Thermocouple
TCCUA	Trichlorosocyanuric acid
TCP	Trichlorophosphate
TG	Thiodiglycol
TMP	Trimethyl phosphate
TPD	Temperature-programmed desorption
SS-NMR	Solid state nuclear magnetic spectroscopy
UHV	Ultrahigh vacuum
VCR	Vacuum coupling radiation
VX	*O*-ethyl *S*-(2-diisopropylaminoethyl) methylphosphonothioate
XPS	X-ray photoelectron spectroscopy/spectrometer
2-CEES	2-chloroethyl ethyl sulfide
2-CEPS	2-chloroethyl phenyl sulfide

Chapter 1

Introduction and Motivation

Thesis Statement

The objective of this research was to develop a fundamental understanding of the interfacial interactions of chemical warfare agents and their simulants with amorphous silicon dioxide.

1.1 Background

The chemistry that occurs at the gas-surface interface plays an important role in the fate of all gas-phase and surface-bound molecules. Compared to the bulk of a material, the surface can be quite heterogeneous in nature. Atoms at the surface have fewer bonding neighbors, creating a different chemical environment for these atoms. The unique chemical and electronic structure of the surface atoms often leads to high chemical activity and influences the fields of catalysis, energy conversion, health care, and environmental protection, among many others.[1-4] However, despite the importance of chemistry occurring at the interface, surprisingly little is known about many different classes of molecule-surface interactions.

The reactions of hazardous vapors, specifically chemical warfare agents (CWAs), with different materials have received significant interest due to recent threats to homeland security and high levels of terrorist activity worldwide.[5] Also, large stockpiles of demilitarized chemical agents present the need to develop an understanding of the environmental fate of these toxins.[6] Additionally, for the rational design of new agent detection methods, the initial, basic interactions of agents with surfaces need to be understood at the molecular level. Furthermore, to develop new decontamination strategies in which chemical bonds are being broken, the types and strengths of these agent-surface chemical bonds should first be well described.

While many researchers have recognized the importance of studying how CWAs react with surfaces, limited studies have been conducted using live agents due to their extremely high toxicity. Scientists often use simulants, chemicals chosen to mimic the chemistry of the live CWAs but lack the toxicity, in attempt to understand the reactivity and fate of agent.[7] However, the degree of similarity between the chemistry of the agents and their respective simulants remains unknown. To begin making simulant-simulant and eventually simulant-agent comparisons, the interactions between chemical warfare simulants and amorphous silica were investigated. Silica was chosen because it is a major component of many militarily and environmentally relevant materials, including quartz, glass, sands, and clays. Furthermore, silica, which is often used as a sorbent or substrate, is typically unreactive.[8-10] Studying the surface chemistry of an unreactive surface serves as the first step in understanding the key differences between simulants and agents.

The experiments described in this work provide for one of the most detailed studies into the fundamental interactions of CWA simulants with silica. The structures of many CWAs and their simulants adsorbed to silica surfaces have not previously been investigated. Also, there is only one previous experimental study that quantitatively reports the adsorption strength of a common simulant with silica.

I conducted my research with the goal of achieving the following three objectives:

1) Determine the adsorption mechanism and measure the desorption energy of nerve agent simulants from amorphous silica.

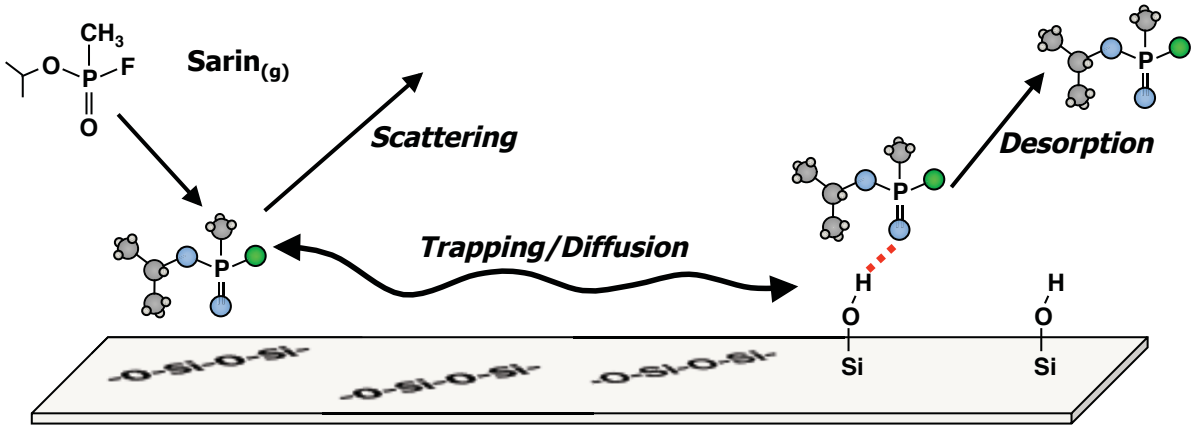

Figure 1.1: Schematic of the nerve agent, Sarin, adsorption on amorphous silica.

2) Determine the adsorption mechanism and measure the desorption energy of mustard agent simulants from amorphous silica.

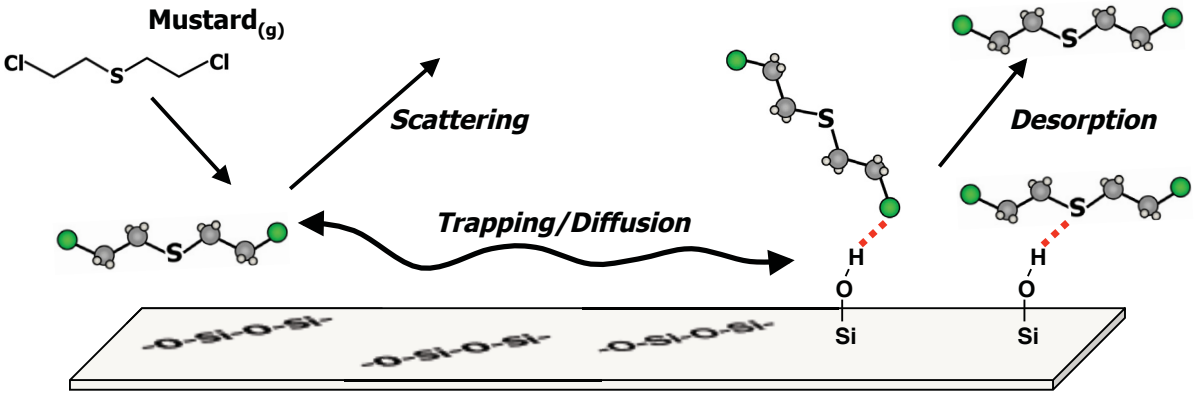

Figure 1.2: Schematic of mustard adsorption on amorphous silica.

3) Directly compare agent and simulant chemistry by designing and constructing a new ultrahigh vacuum surface science instrument suitable for live agent experiments.

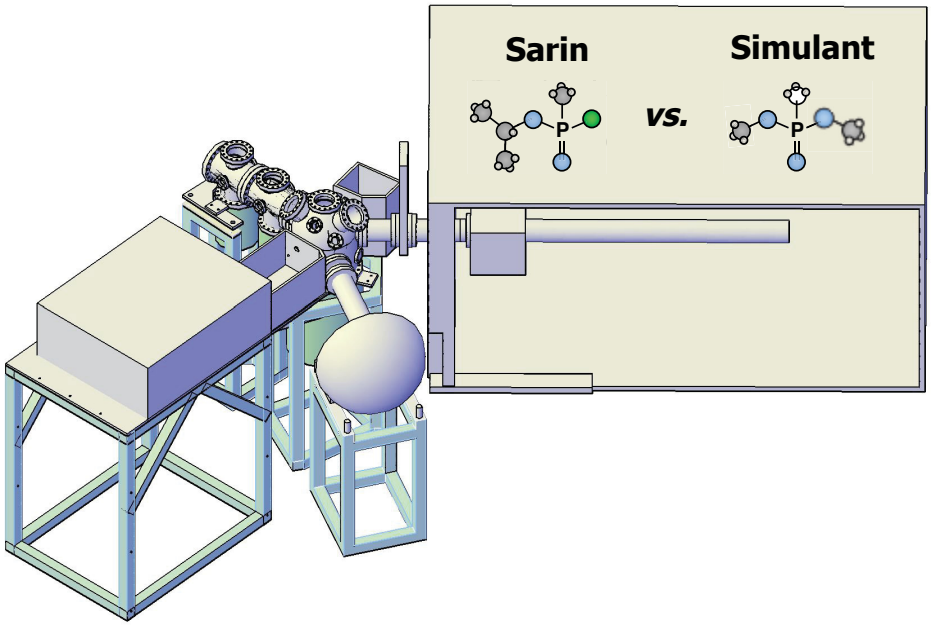

Figure 1.3: Schematic of a new surface science instrument designed for experiments with live chemical warfare agents.

1.1.1. Nerve Agents

Nerve agents are a specific class of CWAs that attack the nervous system. The high toxicity of nerve agents results from their role as irreversible acetylcholinesterase inhibitors. Acetylcholinesterase is the enzyme responsible for breaking down acetylcholine, a neurotransmitter critical for normal function of the nervous system. As a nerve agent is introduced into the body, it binds to a serine residue at the active site of the cholinesterase enzyme as shown in Figure 1.4.[7,11] The phosphorylated enzyme may then lose an alkylic carbonium ion through cleavage of the PO-C bond. At this point, the enzyme is termed "aged", as it is now irreversibly inhibited. Because the agent blocks the active site, acetylcholine can no

longer bind to the enzyme, causing acetylcholine to build to abnormal levels. Initial effects of elevated acetylcholine levels are miosis and rhinorrhea. However, as the acetylcholine levels continue to rise, tremors, respiratory difficulty, and death are imminent.

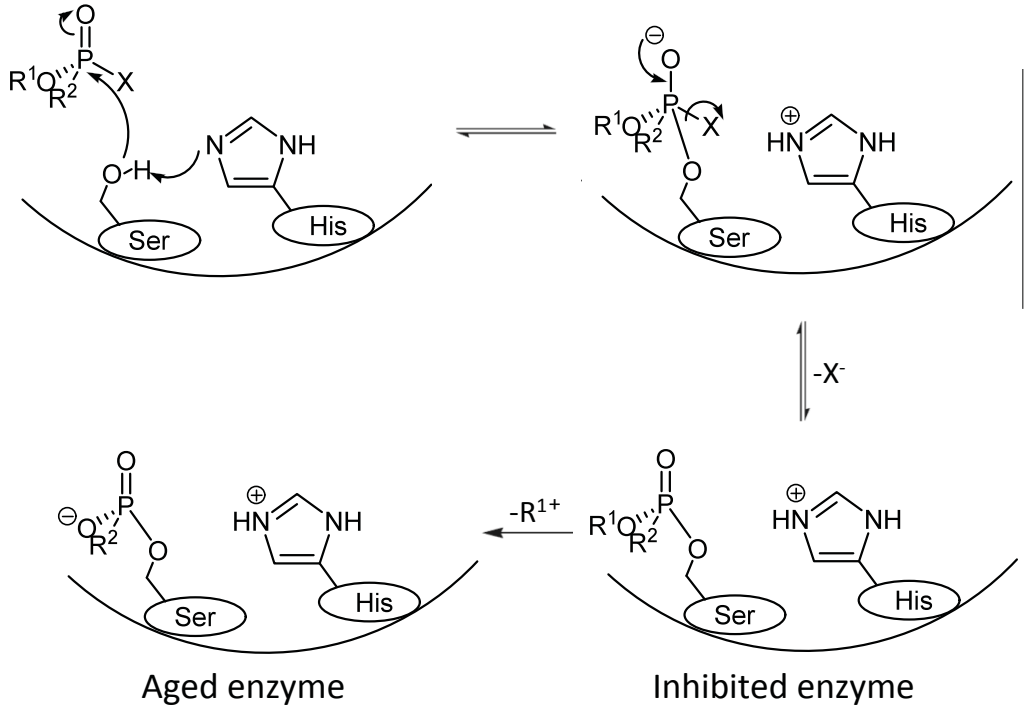

Figure 1.4: Inhibition of acetylcholinesterase at the serine (Ser) residue by an organophosphate nerve agent. Figure adapted from references 7 and 11.

1.1.1.1 History

The high toxicity of certain organophosphates was first noted in 1932 and later utilized by German chemist, Gerhard Schrader in the development of new pesticides. During Schrader's pesticide research, he synthesized Tabun (GA) and Sarin (GB). Noting their extreme toxicity, the samples were sent to the German Ministry Office in 1937, where their potential use as chemical warfare agents began. The synthesis of other G-series agents, G standing for German, shortly followed.

Also investigating newly synthesized insecticides, in the 1950s, the British focused on the development of organophosphonate esters of 2-aminoethanethiols. These efforts led to the

development of a second class of nerve agents called V-agents, V standing for venom or venomous type. VX was considered the most promising of the V-series agents and is often considered the most effective CWA ever produced.

The nerve agents have not been widely used in chemical warfare. However, after chlorine gas was used as a chemical weapon by Germany in WWI, many countries began developing chemical weapons programs primarily for purposes of retaliation and as a deterrent, resulting in the accumulation of large stockpiles. There are reports that Sarin was used by Iraq against Iran during the Iran-Iraq War (1983-1988).[12,13] More isolated incidents with nerve agents have involved the Japanese terrorist group, Aum Shinrikyo.[11,12] Their 1995 attack on a Tokyo subway produced twelve casualties and injured thousands.

1.1.1.2 Physical Properties

Many CWAs are organophosphate compounds. Specifically, the nerve agents are alkylphosphonic acid esters that have the phosphorus (V) atom bound to a hydrocarbon group. They are clear, viscous liquids at room temperature. V-series agents contain a sulfur atom and are alkylphosphonothiolates. The G-series agents contain either a cyanide or fluorine substituent. The structures of four nerve agents are shown in Figure 1.5. Their physical and toxicological properties are presented in Table 1.1

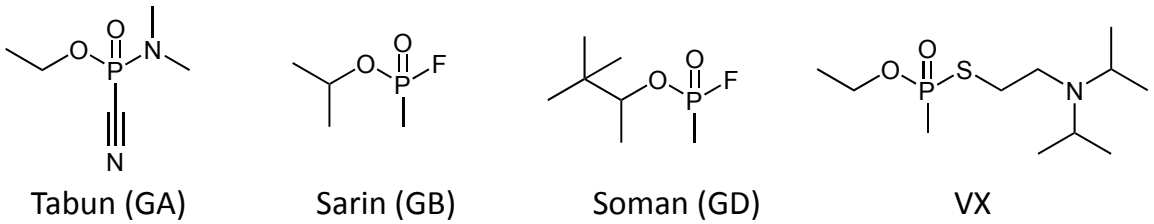

Figure 1.5: Chemical structures of G-series and V-series nerve agents (shown in order of discovery).

Table 1.1: Physical and toxicological properties of nerve agents. LCt_{50} values are the vapor concentrations lethal to 50% of the test population. LD_{50} values are the percutaneous dosages lethal to 50% of the test population.[14,15]

Nerve Agent	Molecular Weight (g/mol)	Melting Point (°C)	Boiling Point (°C)	Vapor Pressure (torr)	LCt_{50} ($mg \cdot min/m_3$)	LD_{50} (mg/ 70 kg person)
GA; Tabun; ethyl *N*,*N*-dimethyl phosphoramidocyanidate	162.1	-49	230	0.037 (@20°C)	400	1000
GB; sarin; isopropyl methylphosphonofluoridate	140.1	-56	158	2.1 (@20°C)	100	1700
GD; soman; pinacolyl methylphosphonfluoridate	182.2	-80	198	0.40 (@25°C)	50	350
VX; *O*-ethyl *S*-(2-diisopropylaminoethyl) methlphosphonothioate	267.4	-20	298	0.0007 (@20°C)	10	6-10

1.1.1.3 Nerve Agent Simulants

In order to study the environmental fate and develop strategies for combating nerve agents, many researchers use CWA simulants. Simulants are molecules designed to possess the same types of bonds of interest and exhibit similar reactivity as the live agent; but are significantly less toxic than the agent due to their inability to bind to the active site and inhibit the activity of acetylcholinesterase. The strategy in choosing simulants is to alter the biochemistry of the molecules while maintaining the important chemical and physical properties. Many different simulants are used, each with a different set of functional groups to mimic the overall reactivity of the agent. However, clearly no one simulant demonstrates the *exact* behavior at the live agent. A simulant is often chosen to mimic either an agent's physical properties, such as vapor pressure and solubility, *or* chemical properties, such as the functional groups. An advantage of using simulants is that the functional groups can be selectively varied, making it possible to study each functionality independently. Because each functionality affects the overall reaction mechanism, by comparing a series of simulants it may be possible to develop

tools for predicting how small changes in structure affect the overall reaction pathway, thereby enabling one to accurately predict how a particular agent will react. The structures of commonly used simulants for the nerve agent Sarin are shown in Figure 1.6. Their physical and toxicological properties are presented in Table 1.2.

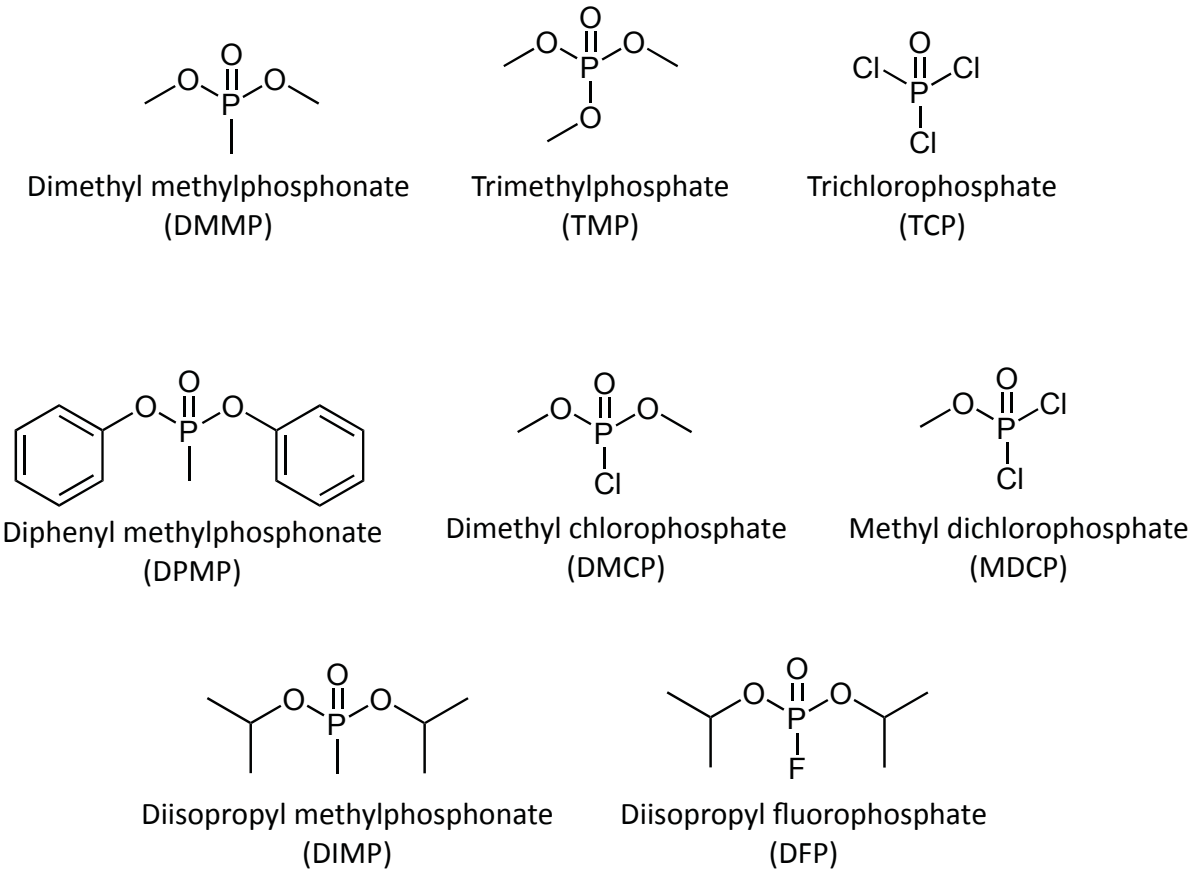

Figure 1.6: Chemical structures of common nerve agent simulants.

Table 1.2: Physical and toxicological properties of selected nerve agent simulants. LD_{50} values are the contact dosages lethal to 50% of the test population of rats.[14,16-18]

Simulant	Molecular Weight (g/mol)	Melting Point (°C)	Boiling Point (°C)	Vapor Pressure (torr @ 25°C)	LD_{50} (mg/kg)
DMMP; dimethyl methylphosphonate	124.08	-48	181	0.96	8210
DIMP; diisopropyl methylphosphate	180.19	<25	121	0.277	826
TMP; trimethyl phosphate	140.08	-46	197.2	0.85	840
DFP; diisopropyl fluorophosphate	184.15	-82	183	0.58	5
GB; sarin; isopropyl methylphosphonofluoridate	140.1	-56	158	2.9	0.10-1.06

1.1.2 Vesicant Agents

A second class of chemical warfare agents is the vesicants, or blistering agents. The blistering agents are strong irritants that target the eyes, skin, and respiratory tissues. Common first symptoms include lacrimation, salivation, coughing, and vomiting. However, these symptoms are rarely observed immediately after exposure. Often times, the effected individuals do not realized they have been exposed to agent until hours later. This latent toxicity increases the agent's impact, because no immediate action is taken to treat the patient or remove them from their toxic environment. The effects of extended exposure are necrosis of the skin and mucous membranes of the respiratory system and ultimately death.

The toxicity of the blistering agents comes from their role as alkylating agents. The mechanism of action for sulfur mustard, a common vesicant, is shown in Figure 1.7. An intramolecular substitution, eliminating chlorine, results in the formation of a cyclic sulfonium ion. This very reactive species can then alkylate a guanine nucleotide of DNA. This modification to DNA makes the vesicants both mutagenic and carcinogenic.[19]

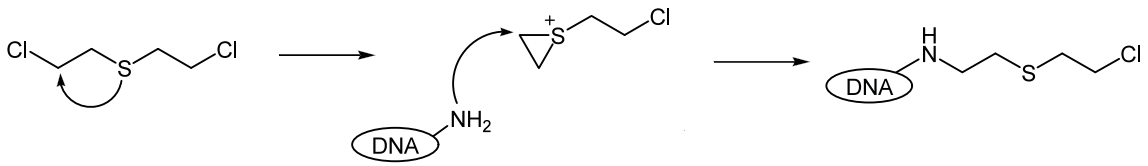

Figure 1.7: Alkylation of DNA by mustard. Adapted from reference 19.

1.1.2.1 History

Unlike many of the nerve agents, the blister agents were developed specifically for chemical warfare. The most common blister agent, sulfur mustard, was first synthesized in 1822 by Despretz. Victor Meyer developed a modified synthesis to produce the higher purity product in 1886. The Germans were the first to use sulfur mustard on the battlefield in July of 1917

against the British near Ypres, Belgium. Mustard was used in WWI, then heavily stockpiled throughout WWII. More recently, Iraq used mustard during the Iran-Iraq war (1983-1988).[13]

1.1.2.2 Physical Properties

Pure sulfur mustard is a colorless, viscous, low-vapor pressure liquid at room temperature. Sulfur mustard also has poor water solubility (0.07% at 10°C), contributing to its consideration as one of the more persistent agents. The common name, mustard gas, comes from the observation that the impure forms used in chemical warfare have an odor similar to the mustard plant. These impure preparations also tend to be brown or yellowish in color.

1.1.2.3 Vesicant Agent Simulants

Again, simulants are used in place of the live agent to make predictions about the environmental fate and decomposition chemistry of the live agent mustard. Figure 1.8 shows the chemical structures of common mustard simulants. Many of the simulants contain both the sulfur and chlorine moieties that are both present in the live agent and are used to mimic the chemical reactivity of the agent. Other simulants, specifically methyl salicylate (MeS), have very little structural or chemical commonalities. However, the similar vapor pressures of mustard and MeS make MeS a good candidate for learning about the physical properties of mustard.

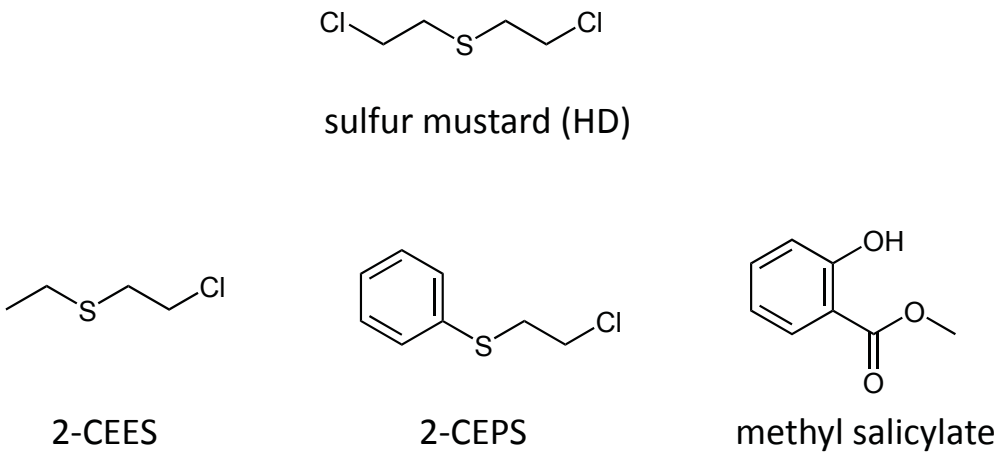

Figure 1.8: Chemical structures of sulfur mustard and common vesicant simulants.

Table 1.3: Physical and toxicological properties of sulfur mustard and common mustard simulants. LD_{50} values are the oral dosages lethal to 50% of the test rat population.[18,20,21]

Molecule	Molecular Weight (g/mol)	Melting Point (°C)	Boiling Point (°C)	Vapor Pressure (torr @ 25°C)	LD_{50} (mg/kg)
HD; mustard; bis(2-chloroethyl) sulfide	159.07	14.45	218	0.11	2.4
2-CEES; 2-chloroethyl ethyl sulfide	124.63	-48.6	156.5	3.4	255
2-CEPS; 2-chloroethyl phenyl sulfide	172.67	17	257	1.9×10^{-2}	--
MeS; methyl salicylate	152.15	-8	223	0.04	887

1.2 CWA Reactions on Surfaces

The reactions of CWAs on surfaces have been studied for applications of agent decontamination and detection, as well as understanding agent fate. Initial efforts for CWA decontamination utilized solution-phase strategies; however, while these methods have been shown to decompose CWAs, solution-phase decontamination is not always a practical approach.[6,7,22] Many of the agent decomposition products are highly toxic themselves. Also, the decontamination solutions are often heavy, difficult to transport, and damaging to the contaminated surfaces.[5] Therefore, more recent efforts have focused on using surfaces as sorbents and decontaminants.

Although many reaction mechanisms involving CWAs have been studied in solution, the reactions on surfaces can be very different. Even though the same reactants are involved, the absence of a solvent can affect reaction rates, energies, and even the reaction mechanism. Using molecular dynamics simulations, Kuo *et al*. have investigated how surfaces can affect the decomposition of Sarin.[23] Under aqueous conditions, Sarin degradation occurs through an SN_2 hydrolysis mechanism with a reaction barrier (ΔG) of 50 kcal/mol. In the presence of a hydrophilic surface, the hydrolysis proceeds through the same mechanism, but with a barrier of only 15 kcal/mol. However, in the presence of a hydrophobic surface, the mechanism changes to SN_1, with the first step being the P-F bond cleavage and the reaction barrier is approximately 60

kcal/mol. The difference in barrier and the change of overall mechanism demonstrates how the presence and the chemical properties of specific surface can have a significant effect on the chemistry.

1.2.1 Metal Oxides

Simulants and live agents have been studied on many bulk metal oxides including Al_2O_3, SiO_2, WO_3, MgO, Y_2O_3 and TiO_2.[24-36] Templeton and Weinberg were the first to investigate the adsorption of a CWA simulant, DMMP, on a metal oxide surface, alumina.[34] They determined there exist two ways for the DMMP to interact with the alumina surface. The phosphoryl group could interact with a Lewis acid site, a coordinatively unsaturated aluminum, or with a Brønsted acid site, a surface hydroxyl. Initially, DMMP adsorbs molecularly through surface hydroxyls. At elevated temperatures (273 to 473K) DMMP binds to Lewis acid sites, resulting in the decomposition of the DMMP as shown in the mechanism depicted in Figure 1.9. The physisorbed DMMP is bound to the surface through the phosphoryl oxygen. Nucleophilic substitution occurs at the central phosphorus atom followed by the dissociative adsorption of a bridging methyl methylphosphonate (MMP) species. A methoxide lost from the DMMP combines with a proton abstracted from a surface hydroxyl to form methanol. As the temperature is increased above 573 K, the MMP surface species further dissociates to form a tridentate methylphosphonate species and methanol by an analogous mechanism.

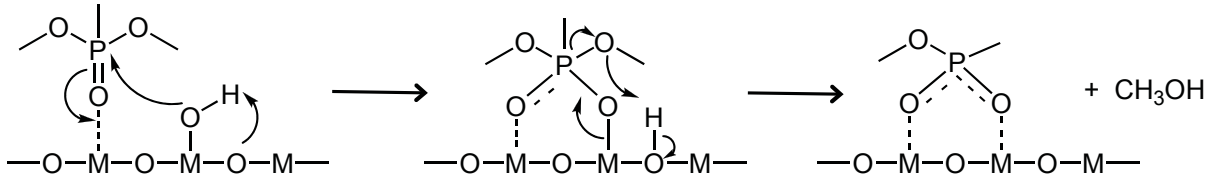

Figure 1.9: Decomposition of DMMP on a metal oxide surface. Adapted from reference 35.

Templeton and Weinberg extended the study described above by examining the adsorption of two other Sarin simulants, diisopropyl methylphosphonate (DIMP) and diphenyl methylphosphonate (DPMP) (structures provided on page 8).[35] They observed that the alkoxy substituent played an important role in the type of adsorption mechanism and subsequent decomposition reactions. After the initial bridging phosphonate species is formed, continued decomposition can occur through nucleophilic substitution at the alkyl carbon of the alkoxy group. The importance of this mechanism depends on the strength of the C-O bond. For the simulants studied, the continued decomposition mechanism was most prevalent for DIMP, followed by DMMP and DPMP respectively. These trends correlate with the ease of C-O bond cleavage, with the isopropyl being easiest and the phenoxy being the most difficult. The differences in C-O bond cleavage are largely attributed to the C-O bond strength. This bond may be significantly affected by the electron donating properties of the other substituents, with the more electron donating substituents contributing electron density that strengthens the C-O bond. Templeton and Weinberg's experiments emphasize that even relatively small changes to simulant structure can have an effect on the overall reaction mechanism and must be considered when using simulants to make predictions about agent chemistry.

A major difference between many simulants compared to the live agents is the lack of the P-F functionality. Although the fluorine is often replaced by a functional group of similar electronegativity, a methoxy or chloride for example, the rate of hydrolysis may be greatly affected. Kanan, Lu, and Tripp have conducted a study looking into these possible differences.[37] They studied the adsorption of DMMP, TMP, and MDCP (structures provided on page 8) on tungsten oxide using Fourier-transform infrared (FTIR) spectroscopy. An important conclusion of their study is that replacing a Cl with a methoxy influences the hydrolysis reaction. Of the

three simulants studied, only MDCP was readily hydrolyzed with water vapor or adsorbed water upon adsorption to the oxide surface. Thus, the question stands that if replacing chorine with a methoxy affects the reaction, how does replacing fluorine with chlorine affect the hydrolysis? One might hypothesize that fluorine, being the most electronegative element and significantly more reactive, would increase the rate of hydrolysis. However, the question remains unanswered and further emphasizes the need to study the live agents themselves to truly understand reaction pathways. A new surface science instrument discussed in Chapter 5 was developed with the aim of understanding these fundamental interactions between live agents and surfaces.

To conduct side-by-side studies of agent and simulant, some researchers have taken a computational approach. Bermudez has conducted quantum chemical studies to compare the adsorption of DMMP and Sarin on different metal oxide surfaces.[38,39] These studies show that the adsorption of both molecules proceeds through the same mechanism (refer to Figure 1.9). However, the binding strengths are significantly different. On alumina, the adsorption energies of DMMP and Sarin were calculated to be -57.5 and -49.2 kcal/mol, respectively.[39] However, to confirm these energies, validate the computational models, and begin to understand why the values are so different, further *experimental* studies comparing of DMMP and Sarin are essential.

A handful of studies have indeed focused on the reactions of CWAs with metal oxide surfaces.[40] Wagner *et al*. has studied the decomposition reactions of VX, GD, and HD with the nanosized metal oxides, CaO, MgO, and TiO_2 using solid state nuclear magnetic resonance (SS-NMR) spectroscopy with the aim of identifying reaction products and measuring reaction rates.[41-43] The overall reaction mechanisms, shown in Figure 1.10 on the following page, for a given agent are generally the same for each of the metal oxides investigated, with minor differences in the reaction rates and ratio of products.

While the SS-NMR work provided valuable information about the surface-bound decomposition products and reaction rates, there are still many unanswered questions about this chemistry. For example, the effects of surface structure, surface cleanliness, and the presence of background gases are not considered. Furthermore, these experiments do not characterize any gas-phase products formed during the decomposition reactions. For a more complete picture of the fundamental chemistry of agents on surfaces, further experiments are required.

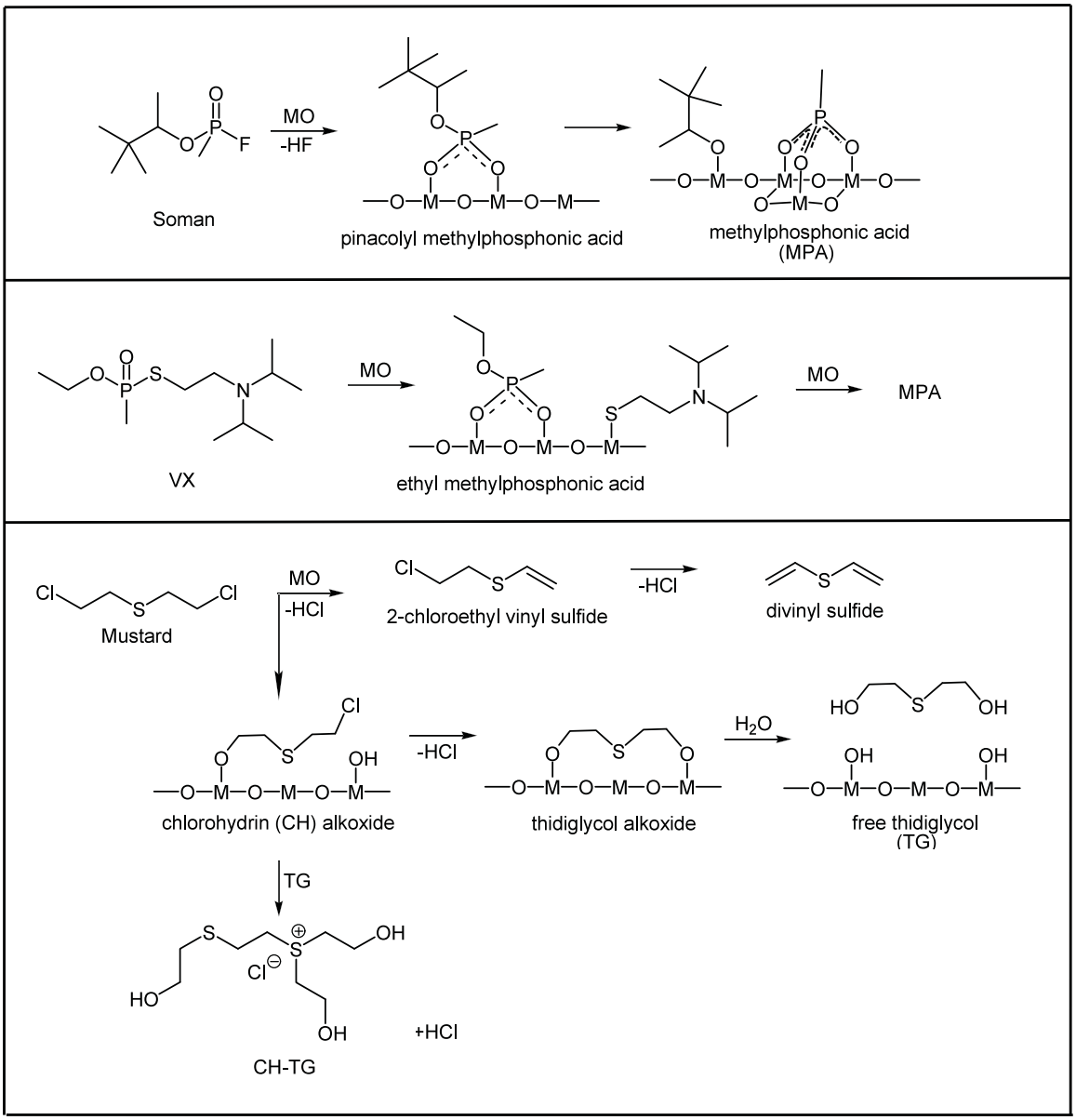

Figure 1.10: Decomposition pathways of the CWAs, GD, VX, and HD, on a metal oxide surface. Adapted from references [41-43].

1.2.2 Heterogeneous Catalysts

The metal oxides mentioned above have been shown to decompose agents; however, their potential use for the sustained decomposition of agent is limited. For many of the reactions, the decomposition reactions are stoichiometric and an extremely stable surface species is formed that requires temperatures in excess of 1000 K for removal.[34,44] This strongly bound surface species essentially blocks the reactive sites and the surface becomes quickly poisoned. Therefore, the field has pushed towards the development of heterogeneous catalysts for the sustained decomposition of agents.

A number of heterogeneous catalysis systems have been shown to be effective for the decomposition of CWA simulants.[7,45,46] Many of these heterogeneous catalysis systems consist of noble metal clusters on oxide supports. Bulk gold is a noble metal and very inert; however, gold nanoparticles demonstrate surprisingly high catalytic activity. Supported gold catalysts have been used for the complete oxidation of alkanes and carbon monoxide.[47,48] The performance of these catalysts depends largely on the size and shape of the Au nanoparticles, which is strongly affected by the structure of the oxide support and the interactions at the gold-oxide interface.[49]

Systems studied related to CWAs include alumina-supported Pt catalysts, which decompose both Sarin and DMMP,[50] and titania-supported gold nanoparticles, which have been shown to catalytically decompose DMMP.[45] However, due to the experimental challenges of conducting experiments with agent, there is no in-depth study into the catalytic decomposition of these toxins. The efforts described later in this document are motivated by the need for a fundamental understanding of agent chemistry on surfaces. Rather than begin our studies with these complex catalysts systems, we started our experiments with a relatively simple, inert surface.

1.3 Silica

Silica, SiO_2, is a material that is very prevalent in our surroundings; however, surprising little is known about the molecular adsorption from the gas phase onto this material. Silica was chosen for the experiments presented here for several key reasons. Firstly, it is a common component of many military and environmentally relevant materials. Understanding the fundamental interactions of different gases, especially toxic gases like CWAs, with this material is essential in learning the fate of these gases. Do CWAs stick to a silica surface? If they do stick, what are the dominating interactions? Additionally, non-reactive surfaces, including silica, are often used for the development of biosensors and prefiltering strategies for agent detection.[26,51] Developing a detailed knowledge of the how agent interacts with materials where non-covalent interactions, such as hydrogen bonding, dominate is key for the further development of these technologies.

Synthetic forms of silica can be produced through liquid or vapor-phase methods. The liquid-phase processes are used to produce silica gels and precipitated silica. Vapor-phase processes produce fumed, or pyrogenic silica. In this method, nonporous silica is formed by the flame hydrolysis of a silica precursor, often times $SiCl_4$.

1.3.1 Silica Structure

In the SiO_2 crystal structure, the Si atom is in the center of a tetrahedron with *sp3* hybridized orbitals. Each silicon is bonded to four oxygens, and each oxygen is bonded to two silicon atoms. The oxygens have two unpaired p electrons on the $2p_y$ and $2p_z$ orbitals and the silicon has a vacant d orbital. Silica is a solid with a high melting point (1700 °C). The refractive index is in the range of 1.5-1.6,

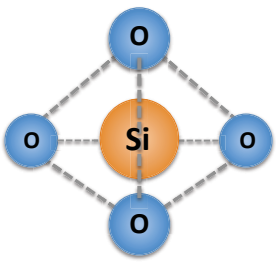

Figure 1.11: Tetrahedral crystal structure of silica.

depending on the extended crystal structure. In amorphous silica, there is no long-range order of a crystal structure; however, local ordering of the SiO_2 tetrahedron is retained.

Yaroslavsky and Terenin were the first to prove the existence of hydroxyl groups on silica, by recording IR spectra of porous glass.[52] Four types of surface hydroxyl groups can be present on silica as shown in Figure 1.12.[53] Free hydroxyl groups are characterized as isolated species on the surface with no other hydrogen-bonding groups within 3.1 Å. Geminal hydroxyls are two hydroxyl groups on the same silicon atom. Vicinal hydroxyls are hydroxyl groups on separate silicon atoms, but are located at distances shorter than 2.8 Å, making it possible for them to hydrogen bond with one another. Terminal hydroxyl groups can be found at the end of a chain of vicinal hydroxyls.

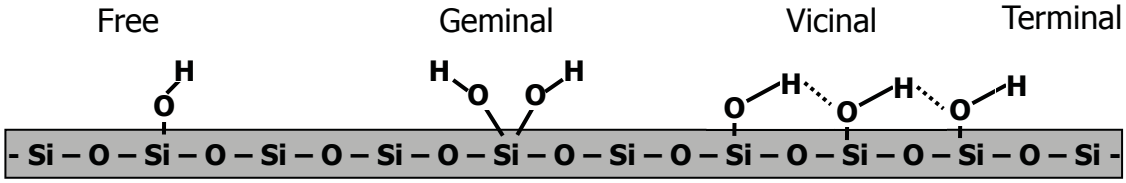

Figure 1.12: Schematic of the four types of hydroxyl groups that can be formed on silica: free, geminal, vicinal, and terminal hydroxyls.

The history of a silica sample can have a significant effect on the concentrations and types of hydroxyl groups present.[54] The maximum hydroxylation level of silica has been measured to be 4.6 OH/nm^2. At this concentration, the average distance between free OH groups is 0.76 nm; the spacing of these OH groups may affect the number of hydrogen bonds a given adsorbate can form with the surface. Upon heating the surface to 150°C in vacuum, vicinal hydroxyls are eliminated via condensation reactions as shown below in Figure 1.13. Further

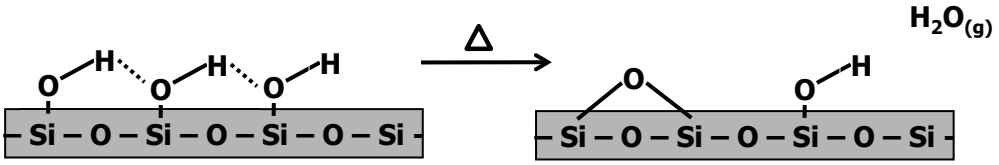

Figure 1.13: Condensation of vicinal hydroxyl groups by heating above 150°C.

heating above 450°C begins the irreversible loss of free hydroxyl groups. At 1200°C, the surface is completely dehydroxylated. The resulting dehydroxylated silica surface is highly reactive, and the dissociative chemisorption of water, ammonia, and methanol has been observed.[55-57] The table below summarizes the work of Zhuravlev and shows the concentration of hydroxyl groups and average distance between free OH groups as a function of sample pretreatment temperature.

Table 1.4: Concentration of hydroxyl groups as a function of silica pretreatment temperature.[54]

Temperature of vacuum pretreatment (°C)	Total OH groups (OH/nm^2)	Free OH groups (OH/nm^2)	Geminal OH groups (OH/nm^2)	Vicinal OH groups (OH/nm^2)	Average distance between two free OH groups (nm)
180-200	4.60	1.20	0.60	2.80	0.76
300	3.55	1.65	0.50	1.40	0.73
400	2.35	2.05	0.30	0	0.74
500	1.80	1.55	0.25	0	0.84
600	1.50	1.30	0.20	0	0.92
700	1.15	0.90	0.25	0	1.05
800	0.70	0.60	0.10	0	1.35
900	0.40	0.40	0	0	1.79
1000	0.25	0.25	0	0	2.26
1100	0.15	0.15	0	0	2.91
1200	0	0	0	0	--

1.3.2 Adsorption to Silica

Surface hydroxyl groups are key for silica's adsorption capacity.[8-10] Compared to the other metal oxides, the silica surface is relatively neutral. Lewis acid sites, which are present on many common metal oxides (Al_2O_3, TiO_2, MgO, etc.), and drive many adsorption and decomposition reactions, are not present on fully oxidized silica. Therefore, much of silica's surface chemistry is dominated by its hydroxyl groups. The formation of hydrogen bonds between surface silanol groups and many small molecules has been observed. Interestingly, for a given adsorbate, hydrogen bonds formed to isolated silanols groups are stronger than those formed with carbinol groups.[58] In the silanol group, the silicon has an unfilled *d* shell that makes

the silanol proton more positive than that of the carbinol, despite carbon being more electronegative. Infrared spectroscopy data supports this trend, as observed by a greater perturbation of the O-H stretching frequency for the adsorbates adsorbed to silanols groups.

The enthalpies of adsorption have been measured experimentally and calculated computationally for hundreds of adsorbates. However, the reported adsorption energy for a given adsorbate can significantly vary, depending on the experiment. For example, the adsorption energy of a single water molecule on silica has been reported as -6 kcal/mol[59] and a high as -14 kcal/mol,[60] a difference of more than a factor of two. The adsorption energy for benzene has been measured to be anywhere from 5 to 40 kcal/mol. This energy difference, in the case of benzene, is largely attributed to the degree of hydroxylation and emphasizes the importance of having a well-characterized surface. The adsorption of molecules specifically related to CWAs will be discussed in more detail in Chapters 3 and 4.

My research focuses on understanding the interactions of chemical warfare agents and their simulants with amorphous silica. Currently, there have been no experiments reported that have investigated how live CWAs interact with silica, a material ubiquitous in our surroundings. Additionally, many questions remain regarding the adsorption of CWA simulants onto this material.

Others have used IR spectroscopy as a tool to learn about the adsorption of gas-phase molecules on particulate samples including silica. For example, the following IR spectrum shows the adsorption of methanol onto an amorphous silica sample.

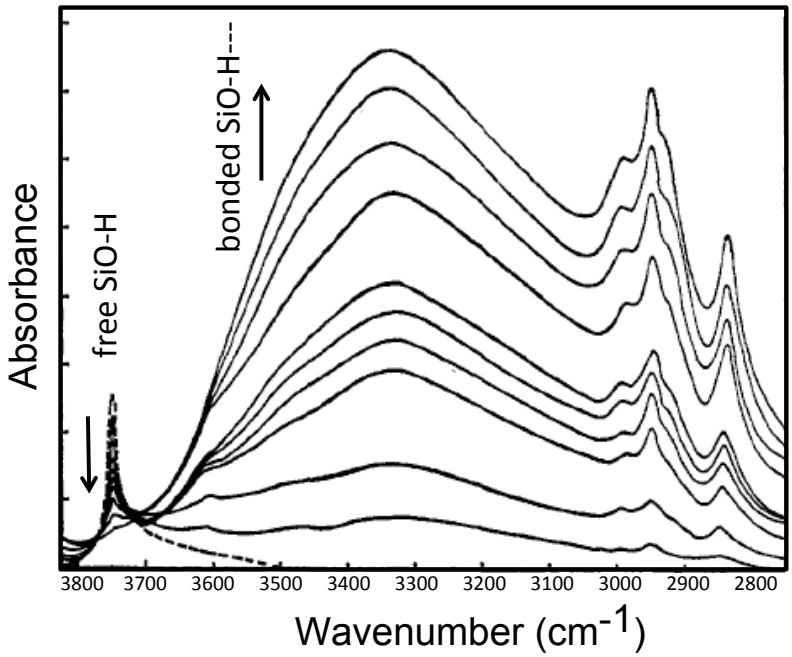

Figure 1.14: IR spectra of amorphous silica exposed to methanol.[61] Reprinted with permission from Borello *et al. J. Phys. Chem. B.* 1967*, 71(9)*, 2945-2951. Copyright 1967 American Chemical Society.

The IR data shows, that upon methanol exposure, methanol adsorbs to the surface as evidenced by the increase of the signature C-H stretches (3000-2800 cm^{-1}) of methanol. Also, changes to the silica surface are observed. Free silica hydroxyl groups (3748 cm^{-1}) are consumed and the formation of a broad peak centered at 3340 cm^{-1} indicates the presence of a hydrogen-bonded species. These changes in the IR spectra provide information about the bonding geometry and indicate that methanol forms a hydrogen bond with the silanols groups. Also, the shift in frequency of the O-H mode, has been shown to be indicative of the strength of the adsorbate-surface interactions.[62-64] Exploiting the powerful nature of this technique, I have also used IR spectroscopy, combined with temperature-programmed desorption techniques, to conduct experiments that provide insight into the fundamental interactions of CWA simulants with silica, as well as provide the tools for completing parallel experiments with live agents.

1.4 Summary and Overview of Thesis

Developing a complete understanding of the uptake, bonding, and chemistry of CWAs on surfaces is essential for the design of new sorbents, sensors, and decontamination strategies. Many researchers use CWA simulants, chemicals chosen to mimic either the chemical or physical properties of agent without the high toxicity, to make predictions about the chemistry of live agents. However, few studies have been conducted that investigate how these structural and chemical differences affect the overall surface chemistry. The goal of this thesis is to understand how small changes in simulant structure affect the overall chemistry, then correlate that knowledge to the chemistry of live agent. Additionally this work describes tools developed for studying many types of surface chemistry using live agents.

The experimental approach for the work provided here is described in detail in Chapter 2. In order to learn about the fundamental chemistry at the gas-surface interface, experiments were conducted in an ultrahigh vacuum (UHV) environment. As described previously, the degree of surface hydroxylation and the presence of water can have a significant affect on the overall surface chemistry. Completing experiments in UHV ensures that only the molecules of interest are interacting (simulant and surface) and common background gases such as water are eliminated. The key analytical instrumentation and methods are also described. These methods are among the first developed for measuring the desorption energies of adsorbates from nanoparticulate samples in UHV.

Chapter 3 describes the interactions of nerve agent simulants on silica. A carefully selected series of organophosphonates were studied to learn how very small changes in chemical structure affect the hydrogen-bond formation to an amorphous silica surface. Infrared spectroscopy (IR) and temperature-programmed desorption (TPD) experiments were used to

determine the structure of adsorbed simulant and measure the activation energy for desorption, which has previously been reported for only one common CWA simulant.

The interactions of a second class of CWAs, the vesicants, with silica are described in Chapter 4. The simulants chosen for this work are some of the most commonly used in the field; however, their chemical structures are radically different from one another. The only commonality is their vapor pressure, a key physical property affecting agent fate. Again, IR and TPD experiments were used to investigate the adsorption mechanism and measure the desorption energy.

While studying appropriately chosen simulants allows us to make predictions about agent chemistry, there are limited studies that make direct comparisons between agents and their simulants. The few experimental studies that do exist are conducted in solution or only identify reaction products. Therefore, a major thrust of my research efforts was the design and construction of a new UHV surface science instrument capable of handling live CWAs and is described in Chapter 5. The experiments that can be conducted with this instrument can provide the fundamental understanding required for improving decontamination and detection strategies.

The studies provided here contribute to the detailed knowledge of the interactions of toxic gases with a surface. No simulant behaves exactly like the live agent. However, by completing systematic studies investigating how changes in the chemical and physical properties affect chemistry, we can better predict how the agent would behave. Furthermore, by completing the same types of experiments with live agent, we can make direct simulant-agent comparisons to learn which simulants best mimic agent chemistry.

Chapter 2

Experimental Approach for Simulant-Surface Studies

2.1 Vacuum Considerations

The goal of this work is to develop a basic understanding of the interactions at the gas-surface interface. In order to study chemistry at such a fundamental level, we need a very clean, well-characterized system. By conducting our experiments in an ultrahigh vacuum (UHV), typically maintaining pressures ~10^{-9} torr, we achieve a system in which we have high control over the surface, gas, and their environment.

The ability to maintain surface cleanliness plays an important role when trying to understand reactions occurring at the gas-surface interface. Contamination may lead to the absence of a reaction that would typically occur, reactions with the contaminants, or alternate pathways opened up by the presence of the contaminant. At atmospheric pressure (760 torr) and assuming a unit sticking probability, a 1-cm^2 sample can become contaminated with a monolayer in just one nanosecond. At a vacuum of 10^{-6} torr, this time is increased to one second, a significant increase, but still not enough time to conduct an experiment. Increasing the vacuum level to a pressure of 10^{-9} torr, the time to form a monolayer is extended to 1000 seconds, which approaches a reasonable time to complete an experiment while maintaining a clean sample.

A second important aspect in studying fundamental gas-surface interactions is to have a well-characterized gas. In addition to beginning the experiment with a pure gas or vapor, it is important that this gas only has the opportunity to react with the surface and not with itself or other materials in the vacuum system. To quantify the number of gas collisions, we consider the mean free path, or the average distance a gas molecule will travel before colliding with another gas molecule.

$$\lambda = \frac{1}{\sqrt{2} n \pi \xi^2} \qquad 2.1$$

The mean free path, λ, can be calculated using equation 2.1, where n is the number density and ξ is the molecular diameter. Combining the above equation and the ideal gas law, (equation 2.2) we can see that the mean free path is inversely proportional to pressure.

$$PV = nRT \qquad 2.2$$

P = pressure
V = volume
n = number density
R = gas constant
T = temperature

At a pressure of 10^{-9} torr, which is typical for our experiments, the mean free path is approximately 50 km. This long distance ensures that we have minimal gas-phase collisions and that the molecule of interest, in this case CWA simulant, reaches our sample's surface before colliding with a background gas molecule. A table containing key parameters a different vacuums level is shown in table 2.1.

Table 2.1: Vacuum Properties for N_2 at 20°C.[65]

Pressure (torr)	Number Density (cm^{-3})	Mean Free Path (cm)	Surface Collision Frequency ($cm^{-2}s^{-1}$)	Time for Monolayer Formation (s) *
760	2.7×10^{19}	7×10^{-6}	3×10^{23}	3.3×10^{-9}
1	3.5×10^{16}	5×10^{-3}	4×10^{20}	2.5×10^{-6}
1×10^{-3}	3.5×10^{13}	5×10^{0}	4×10^{17}	2.5×10^{-3}
1×10^{-6}	3.5×10^{10}	5×10^{3}	4×10^{14}	2.5×10^{0}
1×10^{-9}	3.5×10^{7}	5×10^{6}	4×10^{11}	2.5×10^{3}

*Assumes unit sticking coefficient.

The last key reason to conduct experiments under UHV conditions is that several analytical techniques can only be employed under low pressures. The mass spectrometer, for example, requires vacuum because the fragments produced in the ionizer must pass through the

quadrupole without colliding with any other molecules that would change its flight path. To properly conduct X-ray photoelectron spectroscopy, the electrons ejected from the sample require a collision-free path back to the detector for an accurate measure of their energy. Furthermore, the hot filaments used in both of these instruments oxidize readily at high pressures. Lastly, infrared spectroscopy, while it does not require vacuum, operates best under a dry environment.

The UHV instrument described in this chapter was utilized to develop a fundamental understanding of interactions of chemical warfare agent simulants with metal and mineral oxide surfaces. It was designed and constructed by Joshua Uzarski and a detailed description of the instrument construction can be found in his dissertation.[66] His initial experiments were aimed at learning the adsorption isotherms for a series of CWA simulants on silica with reflection absorption infrared spectroscopy (RAIRS) as the primary analytical tool. The work described in much of this dissertation expands on his initial studies with the goal of learning the adsorption mechanism and desorption energies of simulants from silica. This chapter describes the experimental approach and instrumental modifications completed to optimize our system for new thermal desorption experiments.

2.2 Main Chamber

The experiments described here were conducted within a stainless steel UHV chamber which is pumped with a 2000 L/s turbomolecular pump (Pfeiffer, HiMag® 2400) backed by an oil-free scroll pump (Ulvac, DIS-250). The scroll pump foreline can be isolated from the turbomolecular pump with a pneumatic right angle valve (Kurt J. Lesker, SA0100PVQF). The main chamber pressure is monitored with a full range gauge (Pfeiffer, PKR 251) and nude ion gauge (Kurt J. Lesker, G8120). A suite of analytical instruments is coupled to the chamber to

develop an in-depth understanding of the chemistry at the gas-surface interface. A schematic of the chamber is shown in Figure 2.1.

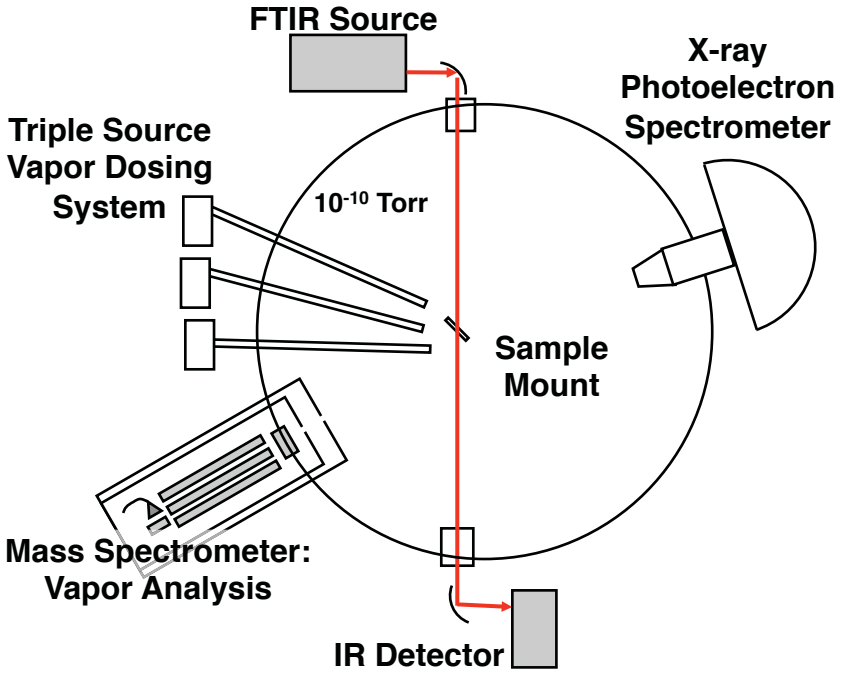

Figure 2.1: Schematic of UHV instrument. The sample, held at the center of the main chamber, can be exposed to different gases via three different vapor dosers. The sample is analyzed with *in situ* IR spectroscopy and mass spectrometry, as well as pre- and post-experiment x-ray photoelectron spectroscopy.

To protect the equipment in the case of a power outage or pump failure, the machine is interfaced to a custom-made interlock box controlled by Labview. The interlock is an interface between experimental components, such as pressure gauges and valves, and a computer program designed to continually monitor the state of the system. If, at anytime, the pressure rises above internal set points, pressure sensitive analytical equipment turns off, the pumps spin down, and the foreline valves close.

2.3 Sample Preparation

One of the most significant changes to the UHV system from its original design was made to the sample holder. To conduct the experiments for this work, we needed to incorporate

heating and cooling with fine temperature control. Previous UHV and HV experiments have successfully achieved these capabilities by pressing nanoparticles into a conductive mesh material that can be resistively heated and cooled and we have taken a similar approach.[25,67]

The sample of interest for this work was high-surface area silica. Approximately 5 mg of fumed silica nanoparticles (Spectrum) with a surface area of 200 m^2/g and average particle diameter of 12 nm was pressed into a tungsten mesh grid (Tech-Etch) with a pressure 2 x 10^8 N/m^2. The tungsten mesh is 0.0508 mm thick with holes of 0.20 x 0.20 mm, spaced 0.254 mm apart. These grid specifications allow for ~75% IR transmittance for a typical pressed sample. The grid is clamped between two nickel brackets. The brackets are fit onto an off-the-shelf copper lead and thermocouple (TC) feedthrough (Kurt J. Lesker, TFT1KY2C302). On the vacuum-side, alumel and chromel wires are spot-welded to the TC leads and near the top of the tungsten mesh. A photograph and schematic of the assembled sample support are shown in Figures 2.2 and 2.3.

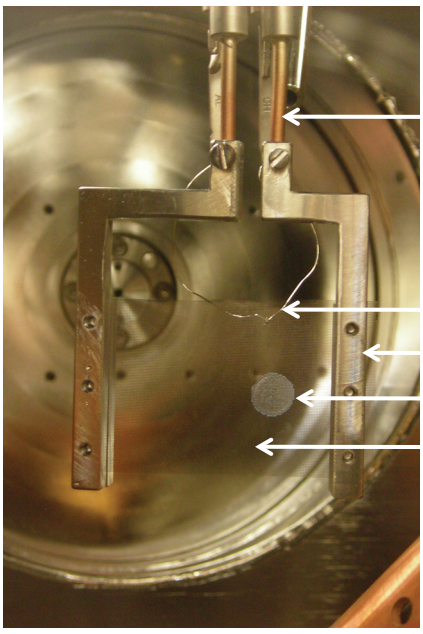

Figure 2.2: Schematic of sample mount showing a nanoparticulate silica sample pressed into a tungsten mesh grid. Silica spot is 7 mm in diameter.

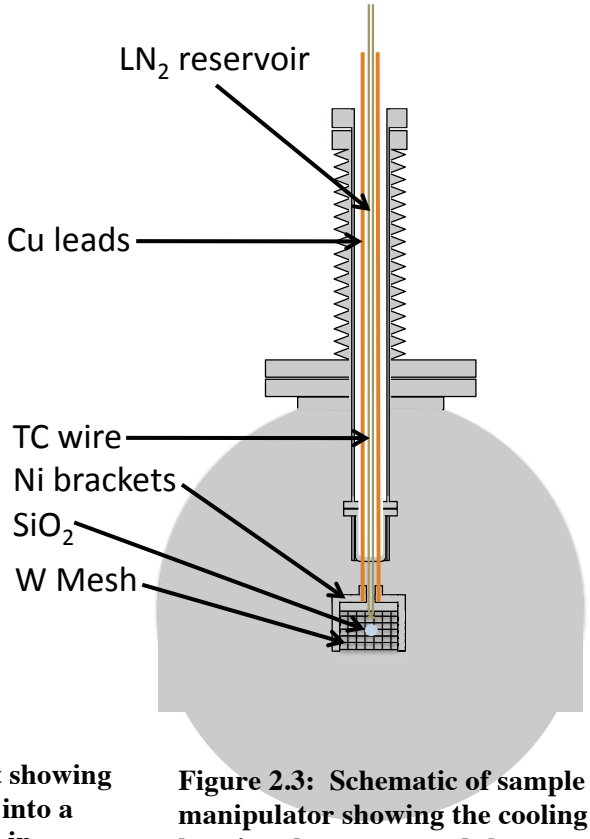

Figure 2.3: Schematic of sample manipulator showing the cooling reservoir housing the copper and thermocouple leads.

The atmospheric side of the feedthrough contains connections to control sample heating and cooling and to monitor the surface temperature. The copper leads are silver soldered to 0.09" thick insulated coppers that were attached to a 50 A power supply which controls the surface temperature with a proportional-integral-derivative device (PID). The TC leads were spot-welded to insulated chromel and alumel wires which were connected to the PID. A custom nipple attaches the feedthrough to an x-y-z manipulator stage with rotation (McAllister). The nipple also serves as a liquid nitrogen (LN_2) reservoir for sample cooling. For experiments that require sample cooling, the reservoir is purged overnight to immediately prior to sample cooling with house nitrogen to ensure a dry environment. The dry environment is important to prevent water from freezing in the ceramic seals of the vacuum feedthrough once liquid nitrogen is added. A crack of these seals required the chamber to be vented, and the feedthrough with all of its attachments to be replaced.

Immediately prior to conducting an experiment, the silica is pretreated by heating the mesh up to 700K using a 0.2 K/s ramp. Heating at this temperature is sufficient to desorb any adsorbed water or remaining simulant from a prior experiment. A large percentage of the vicinal hydroxyls (see section 1.3.1) are eliminated at this temperature, leaving just the isolated hydroxyls that are the focus of these studies. Figure 2.4 provides IR spectra of a newly installed silica sample before and after pretreatment at 700K showing the removal of physisorbed water and hydrocarbon contamination.

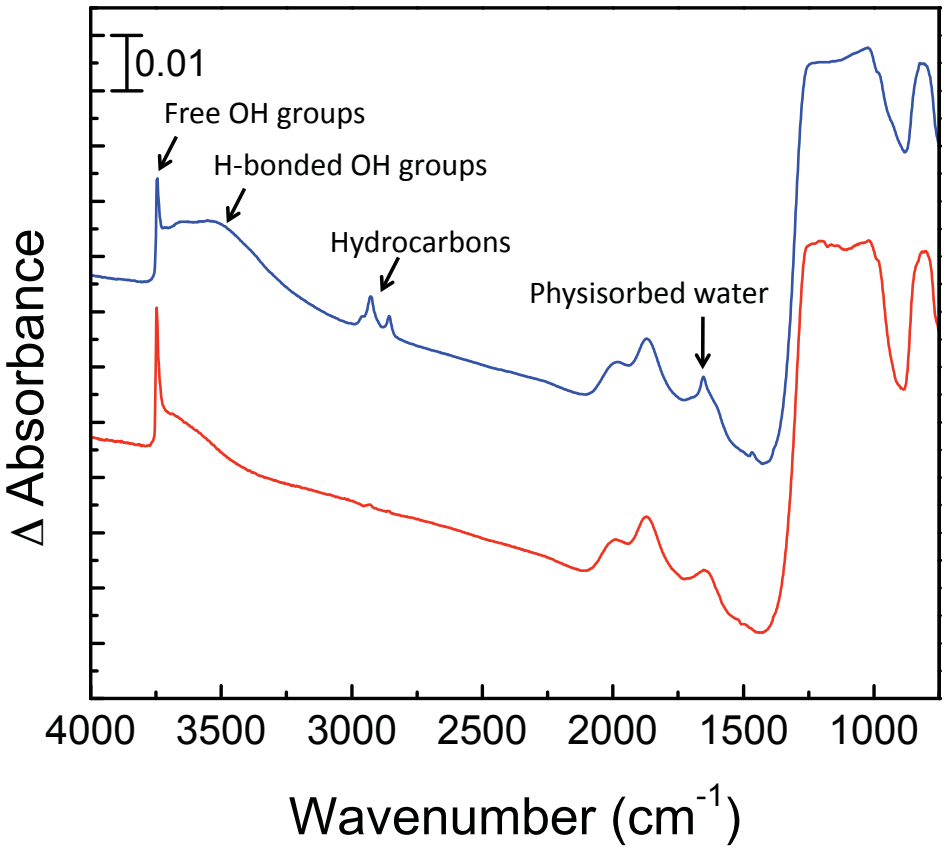

Figure 2.4: IR spectra recorded before (top spectrum in blue) and after (bottom spectrum in red) pretreatment of the silica sample.

2.4 Simulant Dosing

A directional doser was designed and constructed to provide a high, well-controlled flux of simulant molecules to the silica sample. The overall schematic for the doser is shown in Figure 2.5.

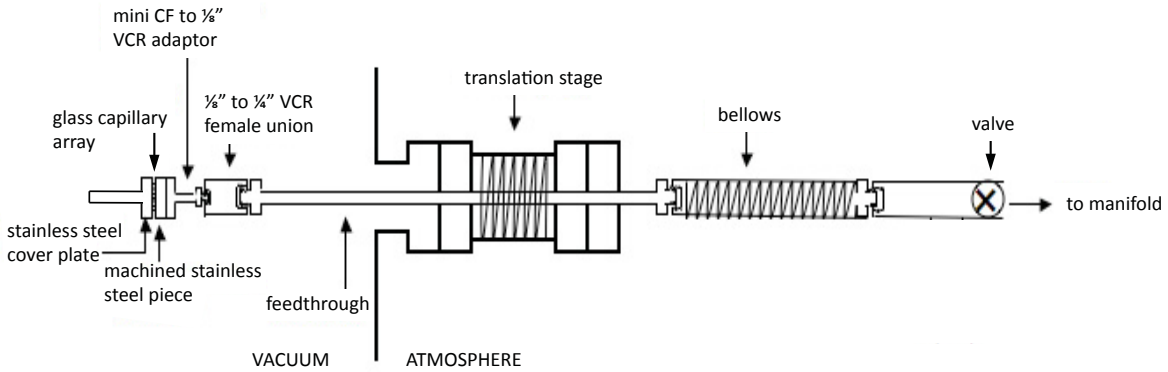

Figure 2.5: Schematic of stainless steel directional doser.

The core component of the design utilizes a custom length gas/liquid feedthrough with modifications on the vacuum side. A thin stainless steel cylinder was machined to seat a glass capillary array (GCA) near the end of the doser. The GCA (Photonis) has 10-micron pores with a center-to-center spacing of 12 microns. A cover plate with a press fit ¼" OD stainless steel tube secures the GCA in place and also increase the directionality of the doser. The entire dosing assembly is mounted on a z-translation stage (McAllister, BLT27C-4) The translation stage allows us to move the doser to within one mm of the sample during dosing.

On the atmospheric side, the doser is attached with vacuum coupling radiation (VCR) fittings to a custom manifold. The manifold is composed of stainless steel tubing and bellows sealed valves (Dibert Valve, SS-4BG-V51). It is typically kept under high vacuum and after dosing it is evacuated with a sorption pump (MDC Vacuum, SP-150) then pumped on with a 60 L/s ion pump (Duniway Stockroom, rebuilt Vairan 911-5034). The pressure is monitored with a full range gauge. A schematic of the manifold is shown in Figure 2.6.

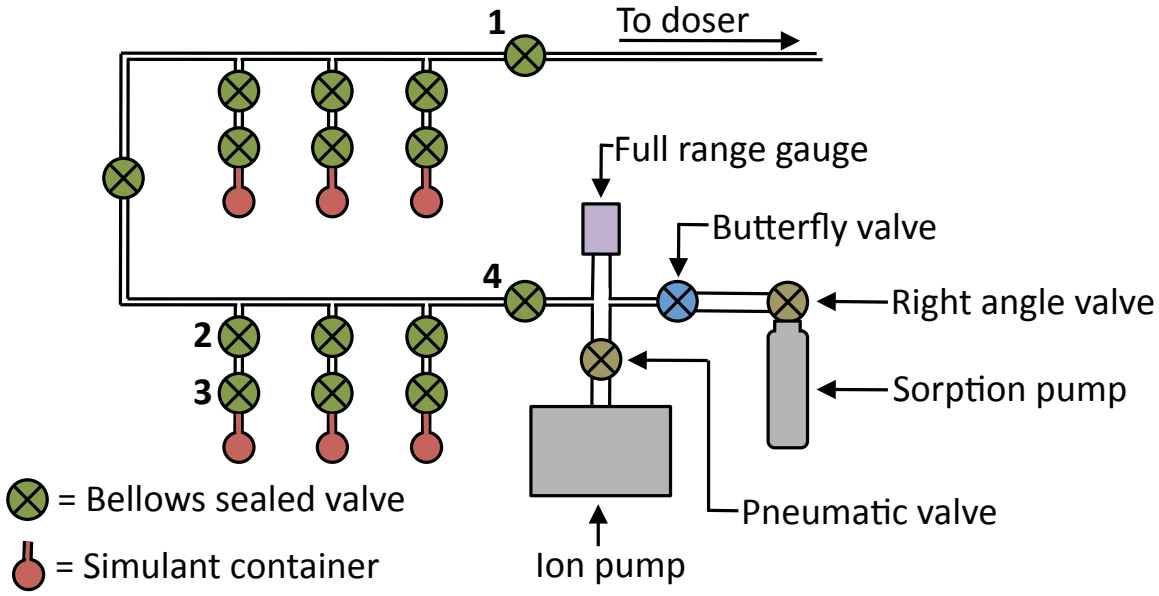

Figure 2.6: Schematic of dosing manifold.

Simulants are either contained in glass bulbs terminated with a glass to metal seal or stainless steel canisters with VCR fittings. The glass bulbs are preferred because the simulant can be viewed during purification; however, the stainless steel canisters are used for more toxic simulants where a break in the glass bulb would cause a safety risk in the lab. In the fume hood, approximately 1 mL of simulant is added to a clean glass bulb or stainless steel canister and attached to a bellows sealed valve that is in the closed position. This assembly is then attached to the manifold and immediately purified via three freeze-pump-thaw cycles. Purity is tested with a mass spectrometer attached to the main UHV chamber. Between experiments with different simulants, the manifold is baked-out with heating tape and backfilled with house nitrogen to clean the dosing lines.

To dose a simulant, the manifold is initially evacuated to a pressure of less than 1×10^{-6} torr. Then, the valve at the back of the doser (shown in Figure 2.5) is opened. A very minor pressure increase is typically observed from trapped gas in the valve and immediately drops back down to baseline pressures within about 5 seconds. Next, pumping by the ion pump is isolated by closing valve #4. Then, valve #1 in Figure 2.6 is closed. This valve ultimately regulates simulant flux into the chamber. Next, both valves above the simulant are opened (valves #2 and #3). Upon opening these valves, there should be no increase in pressure in either the main chamber or ion pump portion of the manifold. Next, valve #1 is slowly opened while closely monitoring the main chamber pressure. Typically, simulant dosing is done while maintaining the main pressure at $\sim 1 \times 10^{-6}$ torr. For higher vapor pressure materials, all of the valves between the glass bulb can be throttled to reduce the conductance of the doser and better manage the main chamber pressure.

To end dosing, the valve at the back of the doser (Figure 2.5) is closed to quickly reduce the main chamber pressure. Next, valve #3 (Figure 2.6) is closed in preparation of evacuating the manifold. First, the sorption pump is cooled with liquid nitrogen. The ion pump is further isolated by closing the pneumatic valve so that it can be kept running during the initial pump out. To rough out the entire manifold, valve #1 is opened and the right angle valve at the sorption pump is opened. Once the pressure reaches 1 x 10^{-3} torr, the right angle valve at the sorption pump is closed as the pneumatic valve above the ion pump is opened. At this stage, the manifold has been evacuated and is ready to begin an additional experiment.

After conducting experiments using more toxic simulants, specifically 2-chloroethyl ethyl sulfide (2-CEES) and 2-chloroethyl phenyl sulfide (2-CEPS), additional safety precautions are taken to clean the system. In addition to baking-out the dosing lines as described previously, the pumping portion of the manifold is also cleaned. Specifically, the stainless steel between the right angle and butterfly valves (Figure 2.6) is wrapped in heat tape and baked-out, backfilled with house N_2 to scrub the walls, then immediately evacuated. Next, the butterfly valve and right angle valves are closed. The seal between the right angle valve and the rest of the manifold is broken and sorption pump is immediately taken to the fume hood for bake-out and replacement of the sieves.

In addition to the stainless steel directional doser, two more dosers are located on the UHV chamber. The first is a directional glass capillary array doser ideally suited for oxidizing gases. A detailed description of the doser can be found in Larry Fiegland's dissertation.[68] The second doser is a variable sapphire-plate precision leak valve (Duniway Stockroom, VLVE-1000) which can be used to backfill the chamber. Having these multiple dosing systems allows us to co-dose different gases. For example, an experiment focusing on how humidity affects

reaction pathways could be conducted by dosing the simulant while simultaneously dosing water. Also, the military is currently developing different decontamination formulas and the components of these formulas could be co-dosed to explore decomposition pathways.

2.5 Infrared Spectroscopy

Transmission Fourier Transform Infrared Spectroscopy (FTIR) was utilized to characterize the surface before, after, and during dosing. IR spectroscopy provides information regarding the vibrational modes of molecules on the surface. Different functional groups vibrate at characteristic frequencies and the molecular identity can be determined based on the energy of these modes.

IR spectroscopy was conducted with a Nicolet Nexus 670 Fourier Transform IR spectrometer. The spectrometer is coupled to the UHV instrument and is purged with dry air. Within the spectrometer is a SiC mid-IR source, aperture wheel, and Michelson interferometer with a KBr beamsplitter. The IR beam is directed outside of the spectrometer into a nitrogen purged optics enclosure. The optics enclosure contains a flat mirror (Bruker Optics IM190-GH) and parabolic mirror (Bruker Optics IM137-GH; f=250mm) to focus the beam onto the silica sample in the center of the chamber. Wedged KBr windows enable the beam to pass into the UHV chamber. After the beam is focused on the sample, it begins to diverge as it leaves the chamber and passes into second nitrogen purged optics box. Within this box, a parabolic mirror (Bruker Optics IM137-GH; f=250mm) collimates the beam and the beam is directed to a flat mirror (Bruker Optics IM190-GH) and second parabolic mirror (Bruker Optics IM151-GH) that focuses it onto a LN_2 cooled mercury-cadmium-telluride (MCT-A) detector which has a 750-4000 cm^{-1} range. A schematic showing the IR beam path is shown in Figure 2.7. The IR spectra

described in this thesis were recorded using the following spectrometer settings: 1.89 cm/s scanner velocity, 32 mm aperature, 128 scans, and 4 cm^{-1} resolution.

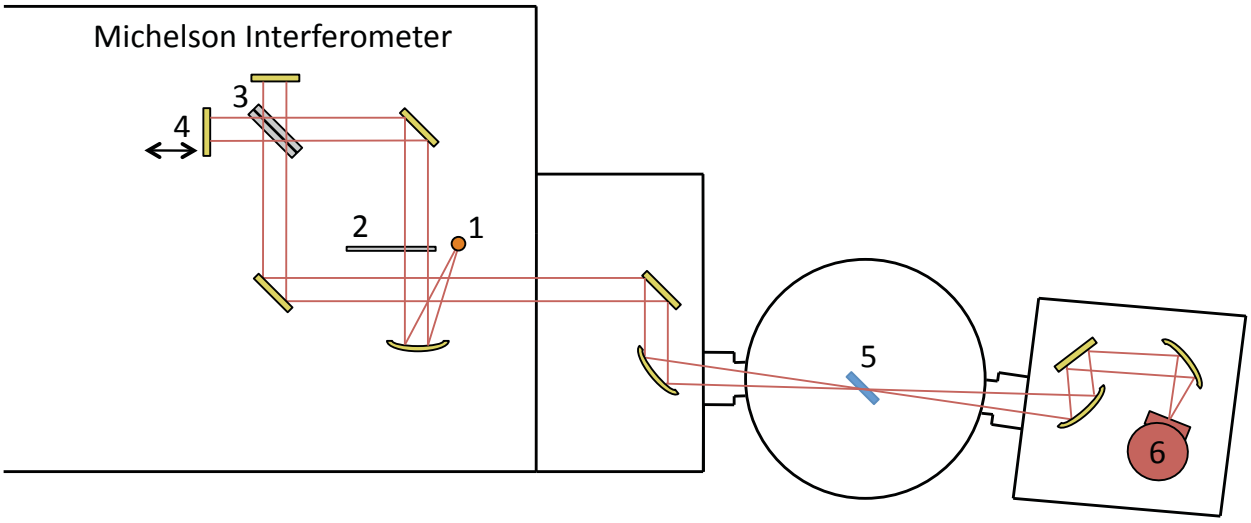

Figure 2.7: Schematic of IR beam path. Labeled components are as follows: 1) SiC source, 2) aperture wheel, 3) KBr beamsplitter, 4) moving mirror, 5) sample surface, 6) MCT detector.

2.6 Mass Spectrometry

The next key instrumental component is a quadrupole mass spectrometer, which has a 2-1000 amu range with 1 amu resolution (Extrel, MAX1000880APP3/4P8). The mass spectrometer allows us to detect gas-phase molecules in the main chamber, specifically those desorbing from the surface. The axial ionizer of the mass spectrometer breaks apart the gas-phase molecules into characteristic fragments that are separated based on their mass-to-charge ratio by the quadrupole rods (19 mm diameter). The fragments are then detected with a channel electron multiplier. Because the mass spectrometer is essentially a number density detector that provides a signal proportional to the number of molecules in the area of the ionizer, the signal is also proportional to the rate that molecules are leaving the surface.

Essential to optimal operation of the mass spectrometer, is the tuning of the ion optics. If the ion optics are not tuned correctly, the mass fragments will not have the appropriate flight path to reach the detector. A schematic of the ion optics is shown in Figure 2.8. First ions are formed via interactions with high-energy electrons (10-100 eV). The ions are

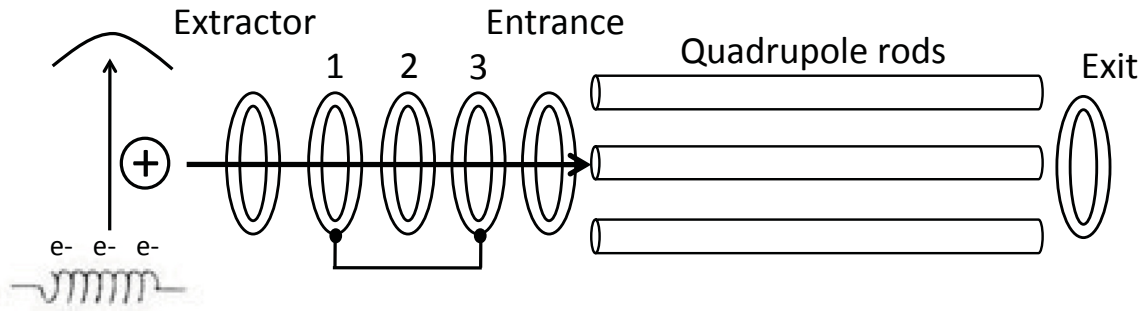

Figure 2.8: Components of quadrupole mass spectrometer.

pulled out of the ion region with the extractor lens, which is held at a small negative voltage. Next the ions travel through three Einzel lenses that help focus the ions as they approach the quadrupole. Einzel lenses 1 and 3 are set to a gentle negative voltage to slow down the ions before they enter the quadrupole mass filter, while lens 2 accelerates the ions. Additional lenses are in place immediately before and after the mass filter, which help focus and pull the ions through the filter. The tune parameters used in the collection of all mass spectral data presented in this work are provided in table 2.2. A mass spectrum over the range of 2 to 100 amu of the background in the chamber using the tune parameters in table 2.2 is shown below. The background gases include water (18 amu), nitrogen (28 amu) and carbon dioxide (44 amu).

Table 2.2: Mass spectrometer tune parameters.

Optics	Setting
Electron Energy	-70 V
Electron Emission	2.00 mA
Ion Region	9 V
Pole Bias	0
Extractor Lens	-13 V
Lens 1&3	-10 V
Lens 2	-90 V
Quadrupole Entrance Lens Min/Max	-10 V/-250V
Quadrupole Exit Lens	-200 V
Dynode Voltage	4000 V
Multiplier Voltage	1750 to 2000 V

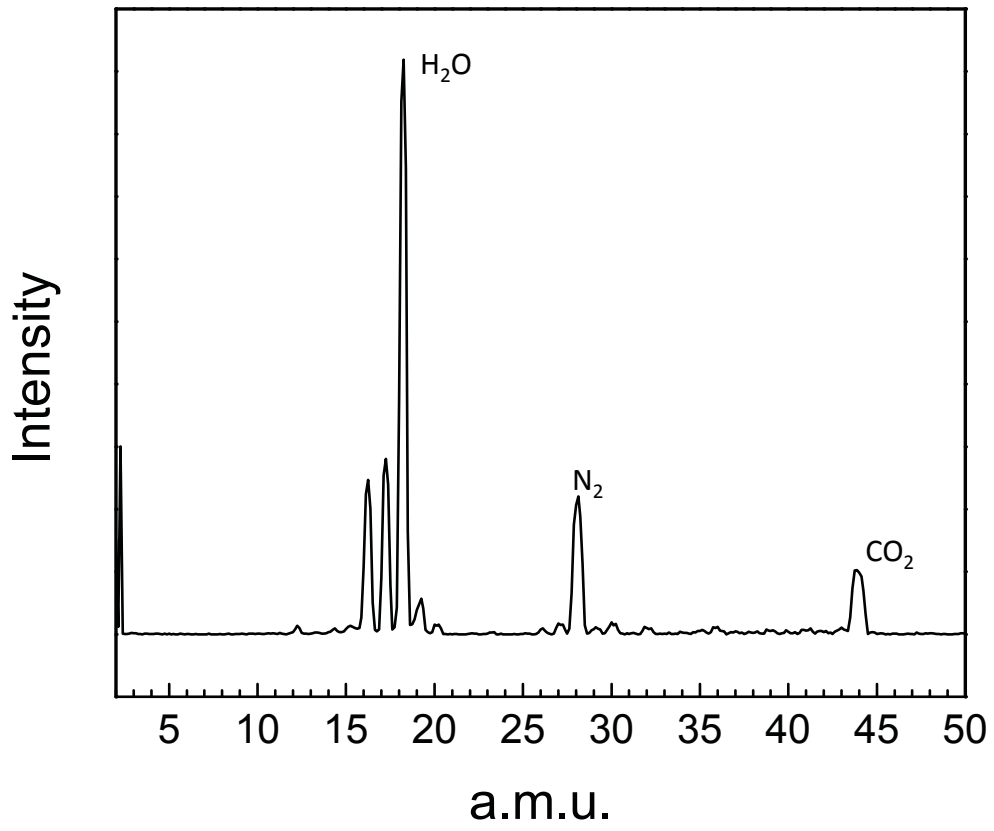

Figure 2.9: Mass spectrum of the instrument background, showing peaks for key background gases, water, nitrogen, and carbon dioxide. Spectrum is offset from baseline for clarity.

There can be many times during an experiment when the pressure in the main chamber is higher than what is allowable to operate the mass spectrometer. To overcome this problem, the mass spectrometer is doubly differentially pumped. The approach to differential pumping, is to drop the pressure in stages by separating the instrument into compartments separated by an aperture. By incorporating this pumping strategy we can have higher pressures in the main chamber ($>10^{-6}$ torr) while still maintaining UHV conditions at the mass spectrometer. A schematic of the mass spectrometer and differential pumping setup is pictured below.

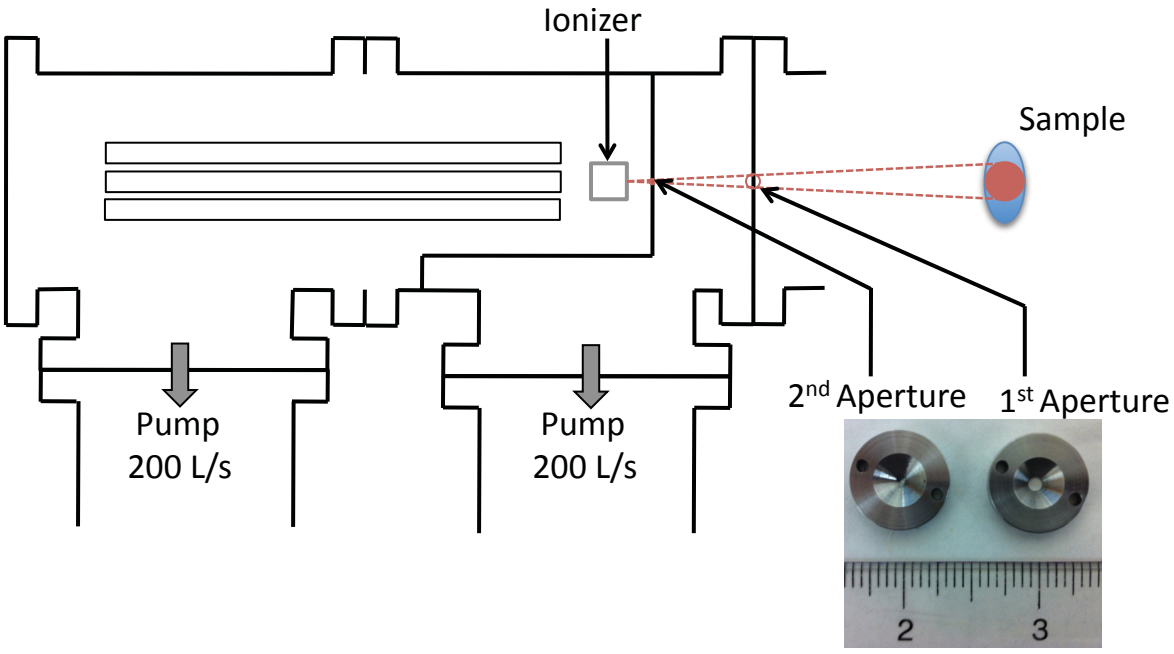

Figure 2.10: Schematic of mass spectrometer arm. The mass spectrometer is separated from the main chamber by two apertures. The apertures provide a differential pumping setup and ensure that molecules from the surface are selectively detected.

The first stage is constructed of a custom cross and is pumped by a 200 L/s turbo pump (Edwards) backed by a scroll pump (Ulvac, DIS 250). The first stage is separated from the main chamber by a 0.106" diameter aperture. The second stage of pumping also houses the mass spectrometer and is pumped by a 200 L/s turbomolecular pump (Pfeiffer) backed by the same Edwards scroll pump. The first and second stages are separated by a 0.185" diameter aperture (ideally this would be a 0.019" diameter aperture as shown in figure 2.10). The pressure in the mass spectrometer chamber is monitored by a full range gauge (Pfeiffer). If at anytime this gauge reads over $1x10^{-7}$ torr, Labview is programmed to turn off the mass spectrometer.

A second advantage of the apertures is exploited during temperature-programmed desorption studies (TPD). During a TPD experiment, the sample is heated and desorbed species are detected by the mass spectrometer. However, during a typical experiment, other regions of the sample holder are also heated. By installing apertures of the appropriate diameter, only molecules desorbing from the silica sample are detected. The aperture sizes were determined by treating the ionizer as a point and using trigonometry to determine the aperture radius based on the sample size and distance from the ionizer. Desorbed species from other regions cannot reach the mass spectrometer based on geometric constraints. Initial TPD experiments conducted without apertures showed significant desorption from regions other than the silica sample as shown in Figure 2.11 (data shown as open circles). The experiment without apertures shows two clear peaks. The shape of the higher temperature peak is typical for zero-order desorption kinetics and would be expected for multi-layer desorption from the sample mount. After installing the apertures and repeating the experiment (data shown as filled circles), the second peak was completely eliminated leaving only the peak showing desorption from the silica surface. A disadvantage of the small apertures is the signal is reduced by

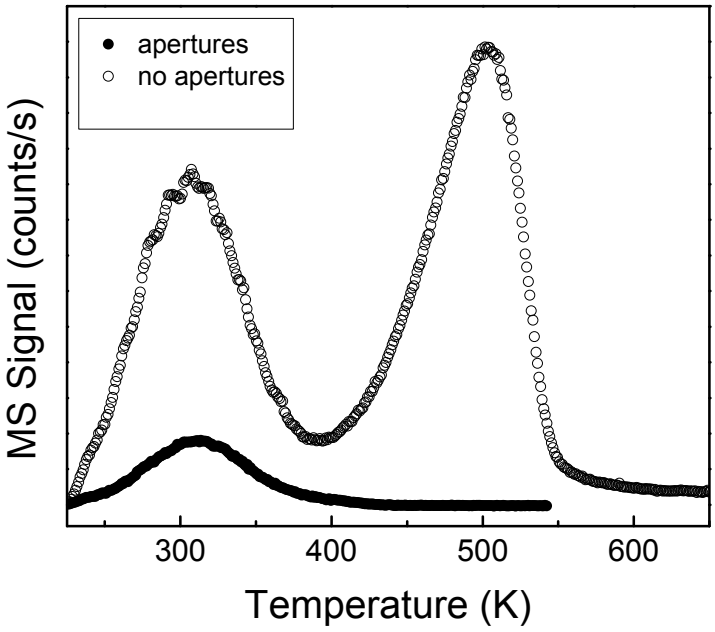

Figure 2.11. TPD spectra before (open circles) and after (closed circles) the installation of the apertures. The peak centered at 305 K is assigned to species desorbing from silica, while the peak at higher temperatures is due to desorption from the sample holder.

about a factor of five; however our signal-to-noise ratio is still more than sufficient for analysis. Also worth noting, is that desorption begins immediately upon sample heating, indicating that we may be missing data from the early section of the TPD profile. Therefore, for later experiments, the sample was further cooled <200K immediately before beginning the TPD ramp.

2.7 X-ray Photoelectron Spectroscopy

The last major analytical technique utilized with the UHV system is an x-ray photoelectron spectroscopy (XPS). An X-ray source (Phi, Model 04-500) emits monochromatic photons that have enough energy to eject core-level electrons called photoelectrons. The photoelectrons are detected with a hemispherical energy analyzer (Phi, Model 10-360). The binding energy (E_B) of these photoelectrons is very specific to the element and even oxidation state of where they came from and can be calculated from Equation 2.3 where

$$E_B = h\nu - E_K - \Phi \qquad 2.3$$

$h\nu$ is the photon energy, E_k is the energy of the ejected photoelectron and ϕ is the work function.

The spectrometer used with the instrument described here has a dual anode source (Perkin Elmer, 04-500), generating radiation of 1253.6 eV or 1486.6 eV with the Mg Kα or Al Kα filaments, respectively. Ejected photoelectrons are then detected with an 11.2" radius hemispherical energy analyzer with a single channeltron electron multiplier (Perkin Elmer, 10-360).

2.8 Summary

For our studies investigating the fundamental gas-surface interactions we conduct nearly all of our experiments in a UHV environment. Working in UHV maintains a clean, well-characterized surface. The sample can be cooled to 125K and resistively heated to temperatures above 1000K. The directional doser provides a high flux of simulant molecules directly to the

silica sample. Adsorbates on the surface are monitored with transmission IR spectroscopy. And desorbed species during TPD are monitored with a differentially pumped spectroscopy. This experimental approach allows us to develop a better understanding of how different gases interact with amorphous silica. The next two chapters describe the fundamental interactions of simulants for two different classes of CWAs, nerve and blister agents, with a nanoparticulate silica surface.

Chapter 3

Adsorption and Desorption of G-Agent Simulants from Amorphous Silica

3.1 Introduction

The focus of this research is to develop a fundamental understanding of the interfacial interactions between chemical warfare agents and amorphous silica. Few labs have the capabilities to study the live agents due to their extremely high toxicity, resulting in the lack of literature describing the fundamental reactions of these compounds. Researchers often use simulants, chemicals that mimic the chemistry of the live agent but lack the toxicity, in attempts to understand the reactivity and fate of Sarin.[7] However, the degree of similarity between the chemistry of the agents and their respective simulants remains unknown. To learn how small changes in chemical structure affect the surface chemistry, we have studied a series of five commonly used simulants for Sarin with the specific goals of learning the types and strengths of the interactions between the simulant and silica surface.

3.1.1 Silica Surfaces

Silica is commonly used as a sorbent where adsorption occurs primarily through hydrogen-bonding interactions between the adsorbate and surface hydroxyl groups.[8-10,69] For this fundamental study of silica, we have chosen to investigate adsorption to free hydroxyl groups. The vicinal hydroxyls can be eliminated via condensation reactions with heating in ultrahigh vacuum conditions as described in Chapter 1.[8]

3.1.2 G-Agent Simulants

Simulants provide an approach to study the environmental fate and potential strategies for combating nerve agents, without needing to worry about their nerve agent activity. Chemical simulants possess many of the same types of bonds and exhibit similar reactivity as the live agents; however simulants are significantly less toxic due to their inability to bind to the active site and inhibit the activity of acetylcholinesterase.[7] Many different simulants are used, each with a different set of functional groups to mimic the reactivity of the agent. By using simulants, the functional groups can be selectively varied, making it possible to study each functionality independently. Each functionality can affect the overall reaction mechanism and by comparing a series of simulants it may be possible to predict the overall reaction pathway.

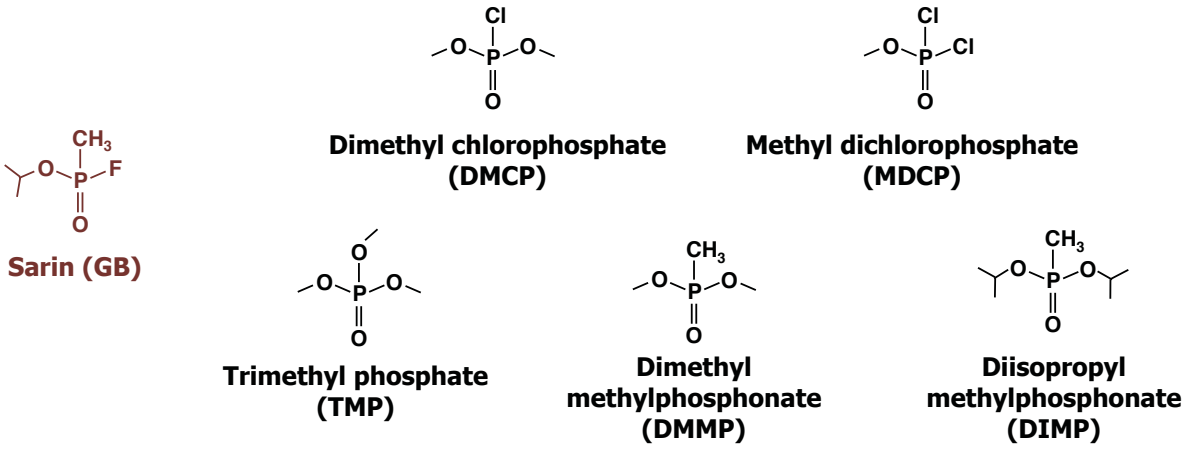

Figure 3.1: The structures of nerve agent, sarin, and the five nerve agent simulants chosen for this work.

Dimethyl methylphosphonate (DMMP) is the most commonly used simulant for nerve agents. DMMP, like the agents and all of the other selected simulants, contains the important phosphoryl group that influences much of the Sarin surface chemistry. The similar volatilities of DMMP and Sarin also contribute to the popularity of DMMP as a simulant choice. Diisopropyl methylphosphonate (DIMP) contains three functional groups identical to Sarin, including the

larger isopropyl group. Dimethyl chlorophosphate (DMCP) and methyl dichlorophosphate (MDCP) both contain a phosphorous-halogen (chlorine) bond and were chosen to mimic the effect of the fluorinated live agent. Trimethyl phosphate (TMP), although containing only the phosphoryl substituent of Sarin, is only one functional group different than both DMCP and DMMP. These minor substituent differences provide an ideal simulant set for studying how small structural changes affect overall organophosphate chemistry.

3.1.3 G-Simulant Adsorption on Silica

The adsorption of organophosphonate compounds on silica has been studied previously, both experimentally and theoretically. Henderson *et al*. performed TPD and Auger electron spectroscopy (AES) experiments of DMMP on hydrated and dehydrated silica.[25] Their experiments indicated that on the heavily hydrated silica, ~8-10% of DMMP is chemisorbed, which results in the formation of surface-bound methylphosphate and methanol. For the dehydrated silica, all of the DMMP was found to adsorb molecularly. Henderson and White also determined the adsorption strength of the molecularly adsorbed DMMP monolayer using TPD. Assuming first-order desorption kinetics and a preexponential factor of $10^{13}s^{-1}$, they reported an activation energy for DMMP desorption of 70.7 kJ/mol.

Kanan and Tripp have contributed to this work by investigating the relative adsorption strength of four common Sarin simulants.[70] In work by the Tripp group, TMP, DMMP, MDCP, and trichlorophosphate (TCP) were exposed to high-surface area silica. These simulants each have a different number of methoxy groups, making it possible to focus on how molecular structure affects hydrogen bonding. They proposed that adsorption strength directly depends upon the number and types of hydrogen bonds made between the simulant and surface hydroxyls. There are two plausible simulant functionalities capable of forming a hydrogen bond

with the surface silanols; the phosphoryl oxygen and methoxy oxygen. Kanan and Tripp suggested hydrogen bonds form between the surface silanols and the simulant methoxy groups. In their work, infrared spectroscopy was used to analyze the type of adsorbed species and which types of hydrogen bonds were formed. The relative adsorption strength was measured by the frequency shift of the SiO-H stretching mode. As an adsorbate hydrogen bonds to the SiO-H groups, the O-H bond lengthens and the vibrational frequency shifts to lower energies. They speculated that the more strongly adsorbed species would have a larger frequency shift. Their IR data show that DMMP underwent the largest frequency shift, suggesting that of the simulants studied, DMMP adsorbed the most strongly. However, experiments conducted to learn the surface temperature required for simulant desorption suggested a different trend. TCP, MDCP, DMMP, and TMP completely desorbed from the silica surface at room temperature 150°C, 300°C, and 400°C, respectively, suggesting that TMP adsorbed most strongly. Based on the temperature required for simulant desorption, the number and types of hydrogen bonds suggested by the Tripp group are shown in the figure below.

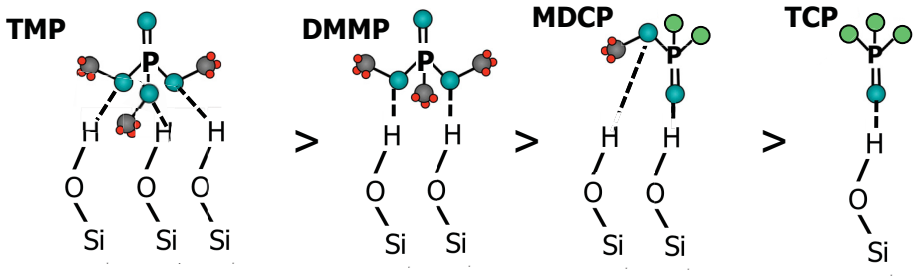

Figure 3.2: Tripp e*t al.* suggested that simulant adsorption strength depends on the number and types of H-bonds formed. [70]

Bermudez has also investigated the types and strengths of the interactions between organophosphonates and amorphous silica; however, from a computational approach.[38] A primary advantage to using computations is that direct comparisons can be made to the live

agent, without the needing to consider the safety aspect. Bermudez's calculations show that TCP, DMMP, and Sarin all adsorb to two surface silanols through the phosphoryl functionality, contrary to Tripp's observation that DMMP adsorption occurs through the two methoxy groups. Bermudez also calculated the adsorption strength of these adsorbates bonded to a $Si_5O_7H_8$ cluster at the B3LYP/6-31$^+$G(2d,2p) level (with a 3-21G(d) basis set for the P atom). For the optimized structures, the adsorption strengths for TCP, DMMP, and Sarin were 43.5, 83.7, and 83.3 kJ/mol respectively. The adsorption strength for DMMP adsorbed through the two methoxy groups, which was the adsorption structure suggested by Tripp, was calculated to be 56.9 kJ/mol. This difference in energy for the different adsorption structures may indicate that the model surfaces were not representative of the silica used in Tripp's work. However, for DMMP adsorbed to thin films, as in Tripp's work, the IR data shows a significant shift (35 cm^{-1}) of the phosphoryl stretch upon adsorption.[70,71] This frequency shift suggests that DMMP hydrogen bonds through the phosphoryl functionality. Also important to note is the nearly identical adsorption strength of DMMP and Sarin, suggesting that DMMP may indeed be an excellent Sarin simulant to use for hydrogen-bonding systems.

Exploring possible causes for the different observations of Tripp and Bermudez, Taylor used molecular dynamics computer simulations to investigate the interaction of DMMP with amorphous silica as a function of surface hydration.[72] Taylor's group observed that the surface hydroxyl concentration significantly affected the types of bonds formed between DMMP and the surface. For high hydration levels of 3.0, 4.0, and 4.5 OH/nm^2, they observed that 77% of the hydrogen bonds formed between the phosphoryl oxygen and surface hydroxyl and just 19% with between the methoxy oxygen and surface hydroxyl; 4% of the adsorbates formed bonds between the phosphoryl oxygen and surface hydroxyl and the methoxy oxygen and surface hydroxyl. At

the lowest hydroxyl concentration investigated, 2.0 OH/nm^2, which is often typical for UHV conditions, they observed that 53% of the hydrogen bonds were formed through the phosphoryl group, while 41% occurred between a methoxy oxygen and the surface, and 6% formed hydrogen bonds through both the methoxy and phosphoryl oxygens. The increase in adsorption via the methoxy oxygen at low surface hydration may be due to additional van der Waals interactions of the incoming methoxy groups.

Tripp *et al*. estimated the surface hydroxyl concentration of the silica used in their work to be 1 OH/nm^2, which, according to the simulations of Taylor and co-workers, suggests adsorption occurs through both the methoxy and phosphoryl groups. However, with this low silanol concentration, it seems unlikely that the average DMMP molecule would be able to form two hydrogen bonds with the surface. That is, the O-P-O spacing is ~3 Å and the average Si-OH spacing at 1 OH/nm^2 is ~10 Å. Even more unlikely than DMMP adsorbing to two silanols is that at this low coverage, the silanols are oriented in a way such that a simulant like TMP can form three hydrogen bonds with the surface, as suggested in the Tripp work.

Also studying the adsorption of simulants on silica, Nadler et al. investigated the adsorption of diisopropyl fluorophosphates (DFP) on high surface area silica using diffuse reflectance infrared spectroscopy.[73] Their study is one of the few in the literature that used a fluorinated simulant. They observed that DFP hydrogen bonds to the silica surface through the phosphoryl oxygen, as suggested by a 41 cm^{-1} red shift of the ν(P=O) mode of DFP compared to the liquid phase. Even with the typically reactive fluorine substituent, they observed no DFP hydrolysis on the surface of silica.

While many groups have investigated the fundamental interactions between select organophosphates and silica, many questions still remain. The adsorption energy of DMMP, for

example, on silica has been reported as 56.9, 70.7, and 83.7 kJ/mol depending on the adsorption structure and method of analysis. In addition to the variation of adsorption strength reported in the literature, only a very qualitative analysis of the relative adsorption strength of different simulants has been reported. To learn how small variations in structure affect the surface chemistry, we have investigated the specific types and strengths of the bonds formed between a series of key organophosphates and amorphous silica.

3.2 Experimental Details

The experimental approach and instrument setup is described in detail in Chapter 2. Experimental details specific to the studies with the organophosphate simulants are provided here.

3.2.1 Materials

Aerosil silica nanoparticles, with a surface area of 200 m^2/g and average particle diameter of 12 nm were purchased from Spectrum chemical. The G-series simulants, DMMP (97%), TMP (99+%), DMCP (96%) and MDCP (85%) were purchased from Sigma-Aldrich. DIMP (95%) was purchased from Alfa-Aesar. All simulants were purified via three freeze-pump-thaw cycles prior to use. Liquid nitrogen (LN_2) and ultra high purity nitrogen were obtained from Airgas.

3.2.2 Preparation of Silica Surface

Silica samples were prepared by pressing approximately 5 mg of silica nanoparticles into a 50 μm thick tungsten mesh grid (Tech-Etch). As described in section 2.2, the mesh was then clamped between nickel brackets attached to the copper leads of a vacuum feedthrough. The sample flange was mounted onto the UHV manipulator and the chamber was evacuated to UHV pressures. The silica sample was aligned with the IR beam path and line of sight for the mass

spectrometer. Immediately prior to each experiment, the mesh was annealed for 5 minutes at 700 K, as monitored by a type K thermocouple spot-welded to the top of the mesh. Based on similar nanoparticle types, this sample pretreatment process produces a surface hydroxyl density of 2.0 OH/nm^2. [8,10] The sample was then cooled by filling the sample reservoir with LN_2 until the desired surface temperature for dosing, 300 or 225 K, was reached. Before exposure to simulant, IR reference scans were collected of both a blank spot of the mesh and the silica sample spot.

3.2.3 Surface Exposure

Simulants were stored in glass bulbs attached to bellows-sealed valves welded on a stainless steel manifold. Immediately prior to dosing, the scroll pump ballast backing the main turbo pump was opened and the stainless steel directional doser with glass capillary array was positioned near the center of the silica sample spot. During initial experiments with DIMP, this distance was approximately 50 mm; however minor modifications to the doser decreased this distance to 3 mm. To begin dosing, the dosing valve was opened, the manifold was isolated from the pumping system, and the simulant was introduced into the chamber at a constant flux. During the exposure, the main chamber pressure was maintained at 1 x 10^{-6} torr.

3.2.4 IR Data Acquisition

Transmission IR spectroscopy was performed with a Nicolet Nexus 670 FTIR spectrometer coupled to the UHV chamber. The light from a SiC globar source was focused at the center of the silica sample, then traveled through an external optics box where the light was focused into a LN_2 cooled mercury telluride cadmium detector. Each spectrum recorded during dosing was the average of 128 scans collected at 4 cm^{-1} resolution, with a 32 mm aperture and 1.89 cm/s scanner velocity. During TPD, the spectra were averages of 16 scans and the same previous settings. The spectra presented in this work are shown as difference spectra. For

characterization of the silica sample itself, a blank spot on the mesh was used to provide a reference spectrum. For surface characterization during dosing, a spectrum of the clean silica sample was used as the reference. During TPD studies, the simulant-dosed silica was the reference.

Gas-phase spectra for each of the simulants were collected for reference using a Nicolet Nexus 470 FTIR spectrometer with a home-built high-pressure flow cell. For these measurements, nitrogen was passed through a glass bulb containing ~5 mL of simulant which transported the simulant vapor into the flow cell. Each spectrum is the average of 256 scans collected at 4 cm^{-1} resolution with a 30 mm aperture and 1.89 cm/s scanner velocity.

3.2.5 Mass Spectral Data Acquisition

An axial ionizer mass spectrometer (Extrel) was used to collect all mass spectral data. Data were recorded during simulant dosing to identify major cracks and to confirm the purity of the source. During dosing, mass spectral data were recorded over the mass range of 15-160 amu. The filament, multiplier, and dynode were set at 2.0 mA, 1750 V, and 4000 V respectively. During desorption experiments, mass spectral data were recorded for the five most intense fragments and the multiplier and dynode were increased to 2000V and 5000V, respectively.

3.2.6 Temperature-Programmed Desorption

Two different TPD approaches were employed for these studies. The first approach was a heating rate variation method. For these TPD experiments, the simulant, DIMP, was dosed at room temperature for 90 minutes at a constant flux. After dosing, the sample was cooled to 195 K and the sample was then heated at one of 5 different linear ramp rates: 0.2, 0.4, 0.6, 1.0, and 2.0 K/s using a Honeywell PID and custom power supply. After all detectable adsorbates had

desorbed from the surface, the mass spectrometer settings were reduced to standby conditions and the LN_2 reservoir was purged with house nitrogen to keep the UHV ceramic seals dry.

The second TPD approach varied the initial coverage while using a constant ramp rate. For the coverage dependent studies, all simulants were dosed onto a 225 K silica surface. A key step in the surface preparation for these TPD studies was implemented to ensure a uniform adsorbate distribution prior to TPD. As shown by Zubkov[74] *et al*., who performed TPD of N_2 on highly porous surfaces, a uniform distribution of adsorbate is required for accurate interpretation of the resulting spectra. It was determined that a uniform distribution was achieved if the tail edges of the TPD spectra collected at a 0.2 K/s ramp rate were aligned, indicating the adsorbates were mobile enough to locate the strongest adsorption sites. If the tail edges were not aligned, the annealing temperature was increased. The sample was annealed to 250 K for MDCP, 275 K for DMCP, and 300 K for TMP, DMMP, and DIMP.

To begin the TPD with different initial coverages, the sample was annealed for different lengths of time (between 1 second up to 15 minutes). Immediately following annealing, the sample temperature was dropped to 195 K. At this time, the doser was pulled back as to not obstruct the path between the sample and the mass spectrometer, the sample was realigned to provide the best possible line of sight with the mass spectrometer, and a new silica IR background spectrum was recorded.

The TPD was conducted using a 0.2 K/s ramp controlled with a Honeywell PID and custom power supply. This relatively slow ramp provided sufficient time for molecules to diffuse throughout the silica sample before desorbing. IR and mass spectral data were recorded throughout the temperature ramp until the surface temperature reached 450 K. After the adsorbates had desorbed from the surface, the mass spectrometer settings were reduced to

standby conditions, the sample was returned to room temperature, and the LN_2 reservoir was purged with house nitrogen to keep the UHV ceramic seals dry.

3.2.7 Quantum Chemical Calculations

In addition to detailed experimental studies, quantum chemical (QC) calculations of selected organophosphates were performed. Minimum-energy geometries were calculated at the MP2/6-31G* level and Mulliken charge analysis was performed at the MP2/cc-pVTZ level. The interaction energy of each simulant with a silanol was also computed at the MP2/cc-pVTZ//MP2/6-31G* level accounting for basis set superposition error. All calculations were performed by Professor Diego Troya of Virginia Tech.

3.3 Results and Discussion

3.3.1 IR analysis

IR spectroscopy is a powerful technique that allows us to identify different functional groups on the surface. By studying the IR spectra, it is often possible to determine the adsorption mechanism of a simulant on silica. Also, the specific vibrational frequencies can offer information about the local environment of the adsorbate. Therefore, to learn the types of adsorbate-surface interactions, *in-situ* IR was used to monitor how the surface changed upon simulant adsorption/desorption. The IR spectra show vibrational modes due to the adsorbed simulant itself, as well as changes in the silica surface induced by the simulant.

3.3.1.1 Characterization of Nanoparticulate Silica Sample

The silica sample was characterized with IR spectroscopy prior to simulant dosing. Figure 3.3 shows the IR spectrum of the silica sample with a blank spot on the mesh used as the background.

The key functionality of the silica surface is the silanol group. For our UHV conditions

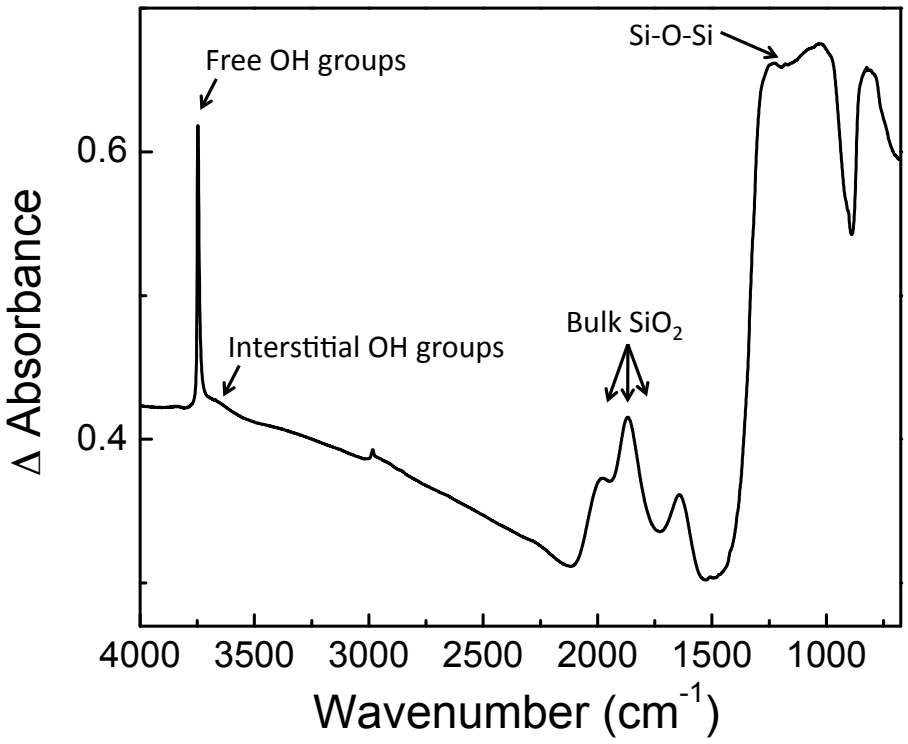

Figure 3.3: IR spectrum of the cooled silica sample at 225 K (pretreated at 700K for 5 minutes). The background spectrum is of a blank spot of the mesh.

and sample pretreatment, the silanol coverage is estimated to be 2 OH/nm^2.[8,10] The peak at 3748 cm^{-1} is assigned to the free, non-hydrogen-bonded hydroxyl vibration. Following how this mode changes upon simulant adsorption offers valuable insight into the adsorption mechanism. The small shoulder at 3670 cm^{-1} is assigned to interstitial hydroxyl groups. These are also free hydroxyls, however their location within pores between the packed silica particles makes them sterically unavailable for adsorption. The minor peaks at 2998, 2959, 2933, and 2857 cm^{-1} are indicative of C-H stretches from a minor, unavoidable amount of hydrocarbon contamination incorporated into the silica sample. The three peaks at 1980 cm^{-1}, 1872 cm^{-1}, and 1648 cm^{-1} are due to overtones and combination modes of bulk silica vibrations. The most intense IR absorption from 1300-1000 cm^{-1} is due to the asymmetric stretches of the bulk Si-O-Si. The corresponding symmetric stretch is centered at 826 cm^{-1}.[9,10,75,76]

3.3.1.2 DMMP Adsorption

IR spectra of the cooled silica sample (225K) were recorded during initial DMMP dosing. Figure 3.4 shows the IR difference spectrum of the silica sample after 24 minutes of DMMP dosing. The gas-phase spectrum of DMMP is also provided for reference. From the IR data, it is

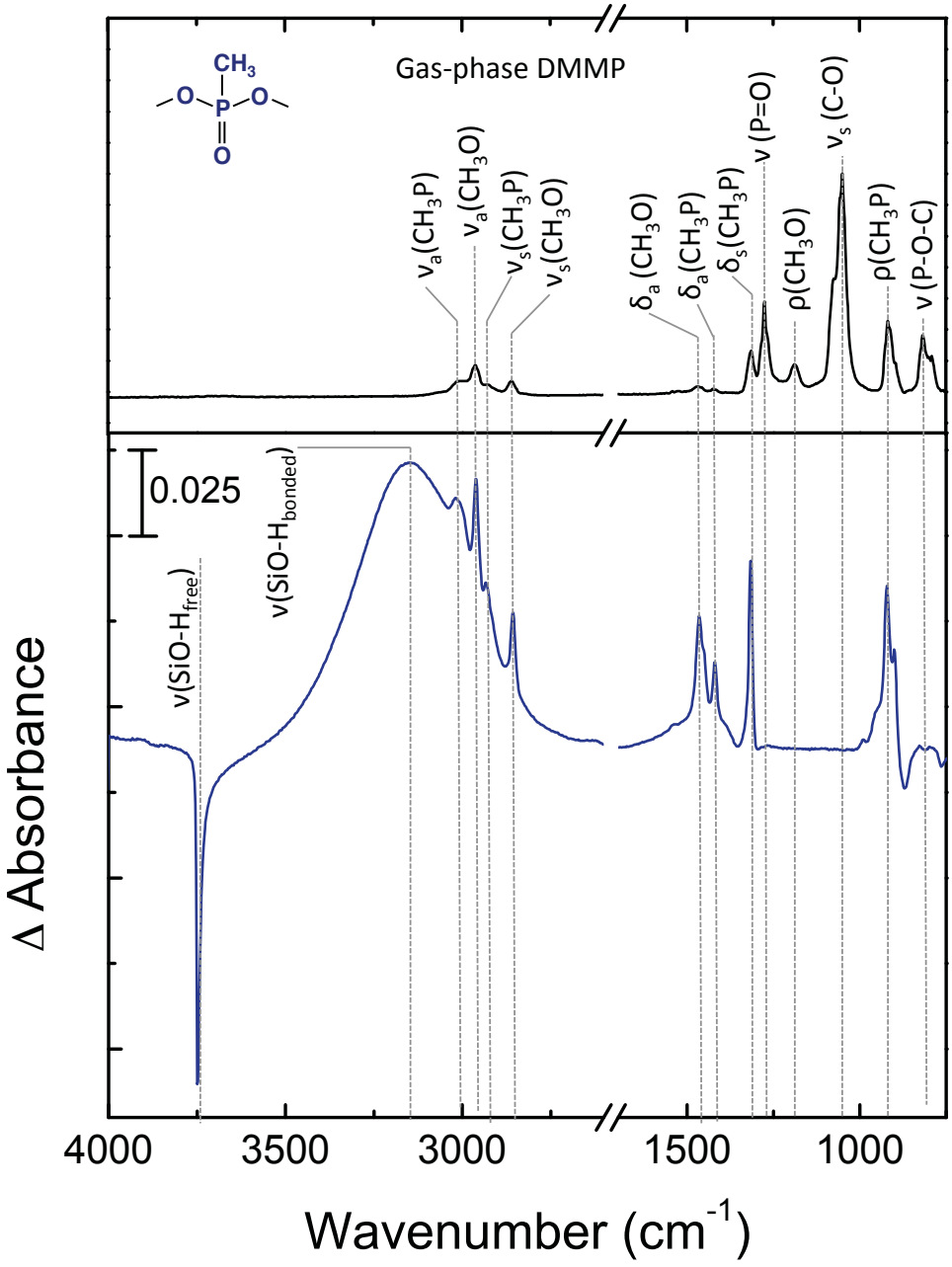

Figure 3.4: IR difference spectrum of DMMP adsorbed to a 225 K silica sample after 24 minutes of dosing. The background spectrum is of the silica sample prior to simulant exposure.[77]

clear that DMMP adsorbs to the surface as evidenced by the development of characteristic vibrational modes of DMMP that grow in intensity during sample exposure. The asymmetric and symmetric C-H stretches of the methoxy groups appear at 2961 and 2857 cm^{-1} respectively.[26,33,77] The $\delta_a(CH_3O)$ and $\delta_s(CH_3O)$ peaks are observed at 1465 and 1452 cm^{-1}. The $\delta_a(CH_3P)$ and $\delta_s(CH_3P)$ peaks appear at 1420 and 1316 cm^{-1}. Notable peaks that are present in the gas-phase spectrum of DMMP, but are absent in the DMMP on silica sample, are the phosphoryl stretching mode (1275 cm^{-1} in the gas phase) and the asymmetric and symmetric C-O stretches (1074 and 1050 cm^{-1} in the gas phase). These peaks are not observable on our silica sample because the silica itself absorbs very strongly between 1300-1000 cm^{-1}.

The IR data provide information about the adsorbate, DMMP, but also show how the silica surface changes upon DMMP adsorption. The sharp, negative peak at 3748 cm^{-1} indicates, that upon simulant adsorption, free hydroxyl groups are consumed. These free hydroxyl groups are converted to hydrogen-bonded hydroxyls, as evidenced by the simultaneous growth of the positive broad peak at 3148 cm^{-1}, which indicates that the adsorbates interact with the surface through hydrogen bonding.

The vibrational frequencies of the characteristic modes of the DMMP molecule, provide information about which functional groups participate in hydrogen bonding with the silica. A shift in the peak frequency of a particular vibration (relative to the gas phase) indicates that the electron density within the region of the molecule associated with the transition dipole moment has changed due to its interaction with the surface. Often times, the mode that has undergone the largest frequency shift is the one participating in the bond. Comparing the gas-phase spectrum to the spectrum of DMMP adsorbed to silica, we see that all major peaks are in identical positions, to within our experimental resolution. Two scenarios may explain this

observation; DMMP does not adsorb through a functionality observed in the IR, such as the phosphoryl group, or the DMMP is very weakly physisorbed to the surface, which may not affect the vibrational frequencies of IR active modes. However, the large red-shift of the hydrogen-bonded mode suggests a strong interaction between DMMP and the silica surface.[38,70,78]

IR spectra were recorded throughout the TPD process and selected spectra are shown in Figure 3.5. The background spectrum is the DMMP-dosed silica sample. During desorption, the peak for the free Si-OH groups becomes positive while the peak for the hydrogen-bonded OH groups become negative, showing that the surface hydroxyls become unoccupied as the surface is heated. There is also a shift of the hydrogen-bonded peak location to higher wavenumbers as the surface is heated. This peak can be very sensitive to surface temperature and coverage. To

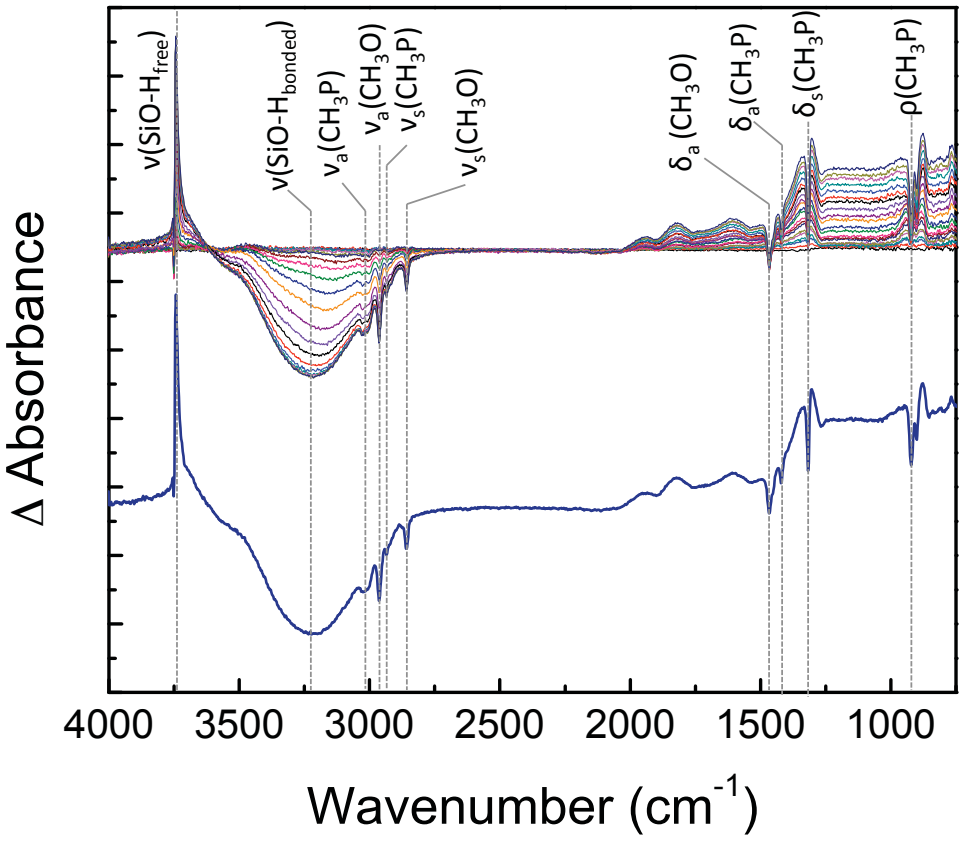

Figure 3.5: IR spectra of DMMP-dosed sample during TPD. The final spectrum taken during the heating is offset for clarity.

assign the frequency of the $\nu(OH)_{bonded}$ mode, the location during simulant dosing is used because at this stage, temperature and coverage are consistent for all of the simulants studied. All of the signature peaks for DMMP also decrease in intensity as the DMMP desorbs. The broad positive peaks in the region of 2000 to 1550 cm^{-1} and the baseline increase at lower wavenumbers are due to heating effects of the silica sample and are observed even when there is no DMMP initially on the surface. The IR data show that upon both DMMP adsorption and desorption, the characteristic DMMP peaks are essentially unshifted from the gas phase indicating that DMMP adsorption and desorption are both molecular. The IR data provides no evidence for decomposition products being formed on the surface.

Table 3.1. Mode assignments for DMMP in the gas phase and adsorbed to silica. (* modes are unobservable in the adsorbed phase due to strong silica absorption.)

Mode	$DMMP_{(g)}$	$DMMP_{(ads)}$
$Si(O-H)_{free}$	--	3748
$Si(O-H)_{bonded}$	--	3147
$\nu_a(CH_3P)$	3013	3014
$\nu_a(CH_3O)$	2962	2965
$\nu_s(CH_3P)$	2933	2934
$\nu_s(CH_3O)$	2859	2856
$\delta_a(CH_3O)$	1468	1466
$\delta_s(CH_3O)$	1457	1452
$\delta_a(CH_3P)$	1424	1421
$\delta_s(CH_3P)$	1313	1316
$\nu(P=O)$	1275	*
$\rho(CH_3O)$	1188	*
$\nu_a(C-O)$	1074	*
$\nu_s(C-O)$	1050	*
$\rho(CH_3P)$	918	925

Two plausible structures for DMMP molecularly adsorbed on silica are shown in Figure 3.6, where hydrogen bonding occurs through either the phosphoryl oxygen or methoxy oxygen functionality. In the gas-phase DMMP spectrum, the asymmetric and symmetric stretching modes of the CH_3O groups are observed at 2962 and 2859 cm^{-1} respectively. In the case of DMMP adsorbed to silica, the $\nu_a(CH_3O)$ and $\nu_s(CH_3O)$ modes are located at 2965 and 2856 cm^{-1}. Mitchell *et al*. have shown that when DMMP adsorbs to other metal oxides including Al_2O_3, MgO and La_2O_3, the methoxy environment changes, which causes a red-shift of the methoxy stretching modes.[31] Their work demonstrates that the stretching frequencies of these modes are sensitive to their environment. Upon DMMP adsorption, the $\nu_a(CH_3O)$ and $\nu_s(CH_3O)$ modes shift only 3 cm^{-1}, which suggests that the methoxy groups are not significantly changed upon DMMP adsorption and that the methoxy groups are not participating in hydrogen bonding.

The second adsorption structure involves hydrogen bonding through the phosphoryl group. The gas-phase location of the ν(P=O) peak is at 1275 cm^{-1}. The phosphoryl peak for the adsorbed DMMP cannot be observed because our thick silica sample results in a very intense Si-O-Si peak, which overwhelms any adsorbate signal in the region of the phosphoryl stretch. However, previous work investigating the adsorption of DMMP on thin films shows the ν(P=O) peak at 1237 cm^{-1}, a red shift of 38 cm^{-1} from the gas phase.[71] This frequency shift suggests that DMMP adsorption to silica occurs via hydrogen bonding through the phosphoryl oxygen.

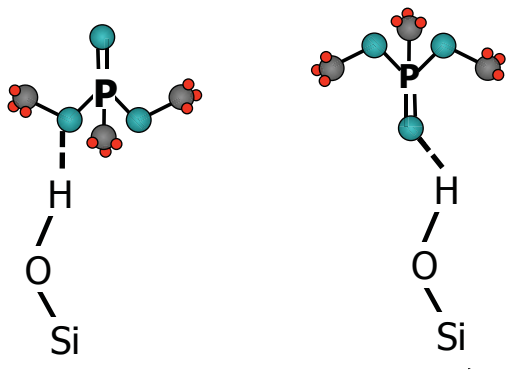

Figure 3.6: Two potential structures of DMMP adsorbed to an isolated surface silanol through a hydrogen bond formed with either the methoxy or phosphoryl oxygen.

As DMMP hydrogen bonds to the surface, the O-H bond of the surface silanol is weakened, resulting in a red shift from the free OH peak position. The direction of this peak shifts can be easily hypothesized using Hooke's law for a harmonic oscillator,

$$\nu = \frac{1}{2\pi}\sqrt{\frac{k}{\mu}} \qquad 3.1$$

where ν is the vibrational frequency, μ is the reduced mass, and k is the spring constant, which is proportional to the bond strength. As the bond strength decreases, the vibrational frequency also decreases. To explore how different functionalities affect the strength of hydrogen bonding, the adsorption characteristics of other simulants was also investigated.

3.3.1.3 DIMP Adsorption

IR spectra of the cooled silica sample (225K) were recorded during initial DIMP exposure. Figure 3.7 shows the IR difference spectrum of the silica sample after 24 minutes of DIMP dosing. The gas-phase spectrum of DIMP is also provided for reference. The conversion of the free OH groups at 3748 cm^{-1} to the hydrogen-bonding species at 3089 cm^{-1} is again observed supporting the adsorption mechanism in Figure 4-8. However, for DIMP, the hydrogen-bonded peak is further red-shifted, correlating to a more strongly adsorbed species. This difference in adsorption strength was also observed qualitatively by dosing the silica sample at different surface temperatures. DIMP readily adsorbs at room temperature while DMMP adsorption is barely visible by IR spectroscopy on the room temperature surface. The modes for the C-H stretches are significantly more intense than in the DMMP spectrum, as DIMP has additional methyl groups.

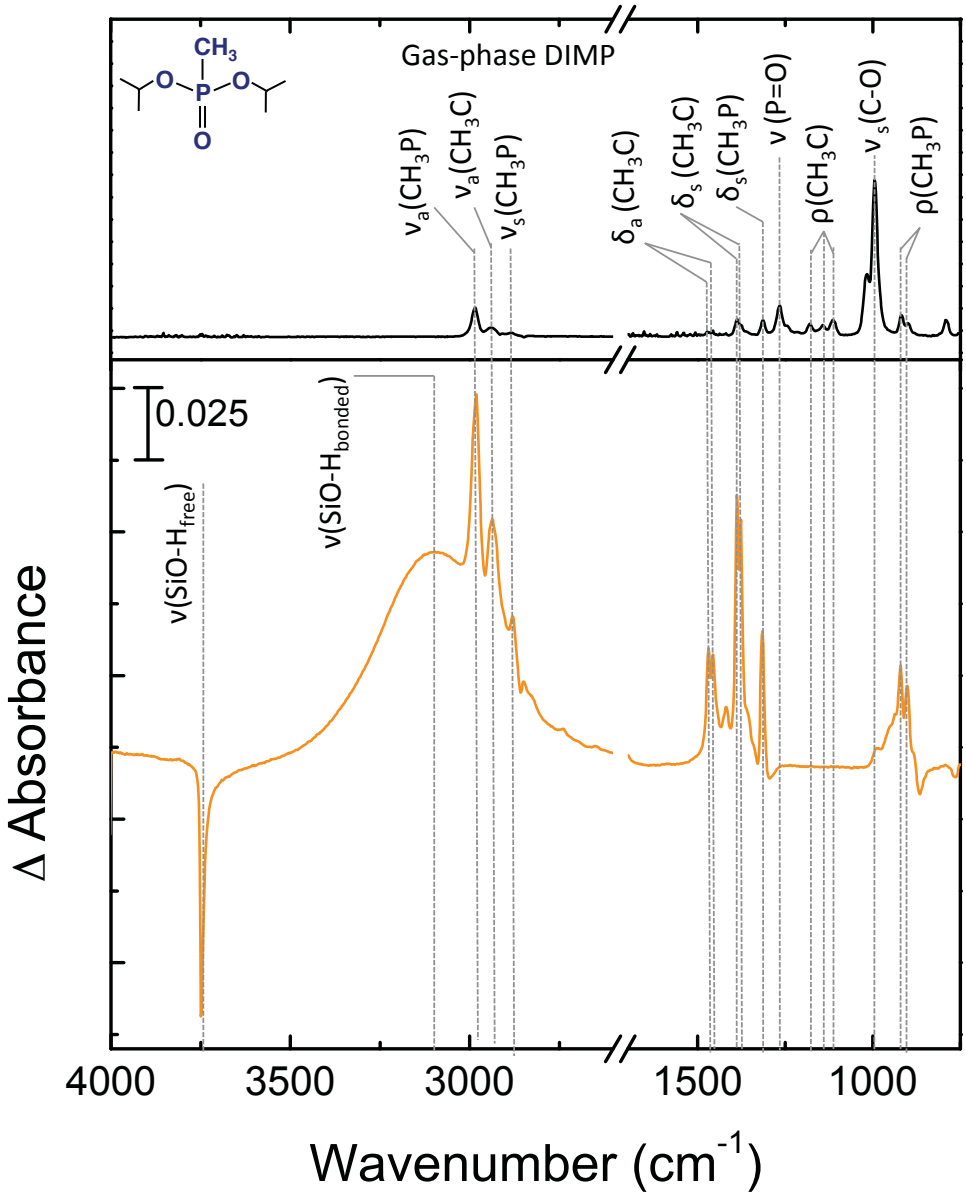

Figure 3.7: IR spectrum of DIMP adsorbed to a 225 K silica sample after 24 minutes of dosing. The reference spectrum is of the silica sample prior to simulant exposure.

Again we look to the IR data from the TPD experiments, as shown in Figure 3.8, to make DIMP peak assignments and learn how DIMP adsorbs to the surface. When the surface is heated, all of the DIMP peaks become negative as the adsorbate leaves the surface. As in the case for DMMP, the ν(P=O) peak, which is observed at 1266 cm^{-1} in the gas phase, is unobserved in the adsorbed state. The minimal shifts of all other DIMP peaks relative to the gas

phase shows that the adsorption and desorption occur molecularly. Also, the absence of a shift of the ν(C-H) mode, suggests that adsorption is not occurring through the ester functionality, leaving the phosphoryl oxygen as the most likely hydrogen-bond acceptor.

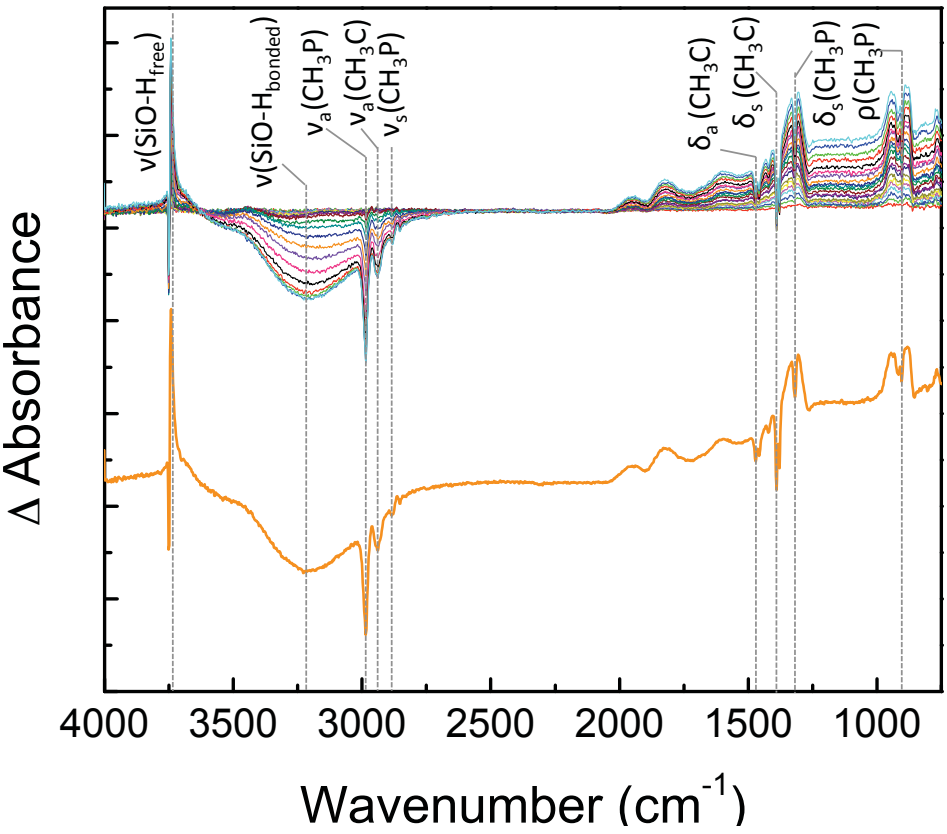

Figure 3.8: IR spectra of DIMP-dosed sample during TPD. The final spectrum taken during the heating is offset for clarity.

Table 3.2. Mode assignments for DIMP in the gas phase and adsorbed to silica.(* modes are unobservable in the adsorbed phase due to strong silica absorption.)

Mode	$DIMP_{(g)}$ [79]	$DIMP_{(ads)}$
$Si(O-H)_{free}$	--	3748
$Si(O-H)_{bonded}$	--	3089
$\nu_a(CH_3P)$	2985	2982
$\nu_a(CH_3C)$	2940	2937
$\nu_s(CH_3P)$	2883	2880
$\delta_a(CH_3C)$	1473	1470
$\delta_a(CH_3C)$	1457	1457
$\delta_s(CH_3C)$	1387	1388
$\delta_s(CH_3C)$	1377	1377
$\delta_s(PH_3C)$	1314	1316
ν(P=O)	1266	*
$\rho(CH_3C)$	1180	*
$\rho(CH_3C)$	1143	*
$\rho(CH_3C)$	1113	*
ν_a(C-O)	1017	*
ν_s(C-O)	995	*
$\rho(CH_3P)$	918	921
$\rho(CH_3P)$	900	902

3.3.1.4 TMP Adsorption

IR spectra of the cooled silica sample (225K) were recorded during initial TMP exposure. Figure 3.9 shows the IR difference spectrum of the silica sample after 24 minutes of TMP dosing. The gas-phase spectrum of TMP is also provided reference. Comparing the gas-phase TMP spectrum to the TMP-dosed silica sample, TMP has clearly adsorbed to the surface and the free hydroxyls of silica have been consumed and converted into a hydrogen-bonded species. Unlike the spectra for DMMP and DIMP, the vibrational freqency of the phosphoryl stretching mode is observable which is suggested to be the mode responsible for hydrogen bonding. In the gas phase, the ν(P=O) mode is observed at 1291 cm^{-1}; upon adsorption to silica, this peak

undergoes essentially no shift and is observed at 1292 cm^{-1}. However, at the cold silica temperature, a large percentage of simulant may be frozen on the surface. The observation that none of the functionalites capable of hydrogen bonding undergo a frequency shift upon adsorption agrees with this picture and emphasizes the importance of annealing our sample before conducting desorption studies.

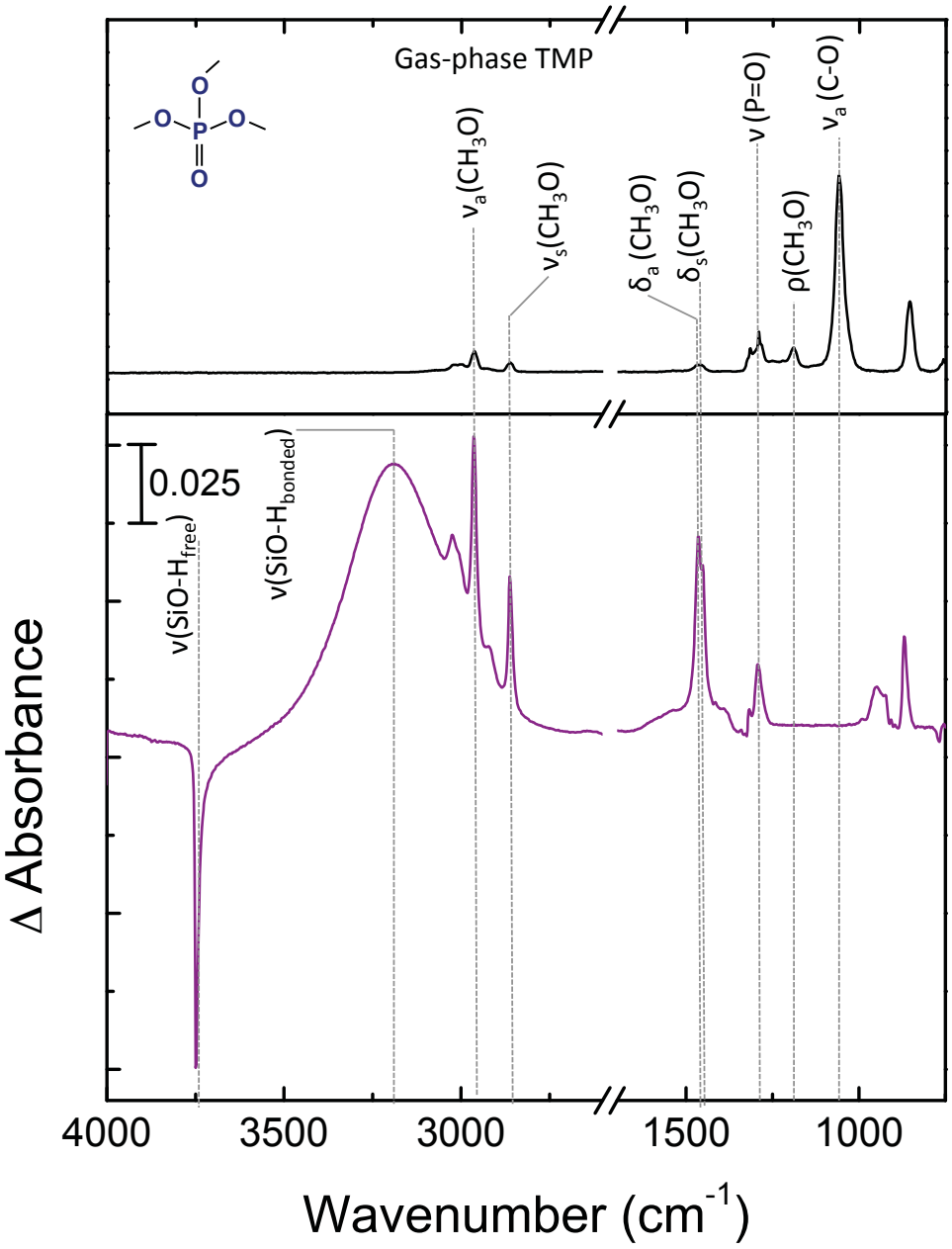

Figure 3.9: IR difference spectrum of TMP adsorbed to a 225 K silica sample after 24 minutes of dosing. The reference spectrum is of the silica sample prior to simulant exposure.

During the TPD experiment, IR data were collected as the sample was heated and TMP desorbed from the surface. During simulant desorption, the OCH_3 stretching and deformation modes are unshifted from their gas-phase locations as observed for the other simulants. However, upon desorption, the phosphoryl stretch is significantly red-shifted by 17 cm^{-1} suggesting that this is the functionality responsible for hydrogen bonding to the surface silanol groups. Previous work investigating TMP adsorption on thin films of silica have shown similar frequency shifts with the ν(P=O) peak being observed at 1268 cm^{-1}, a shift of 23 cm^{-1}.[26,71] As observed for both DMMP and DIMP, TMP molecularly adsorbs to the surface through the formation of a hydrogen bond between the free OH group and phosphoryl oxygen.

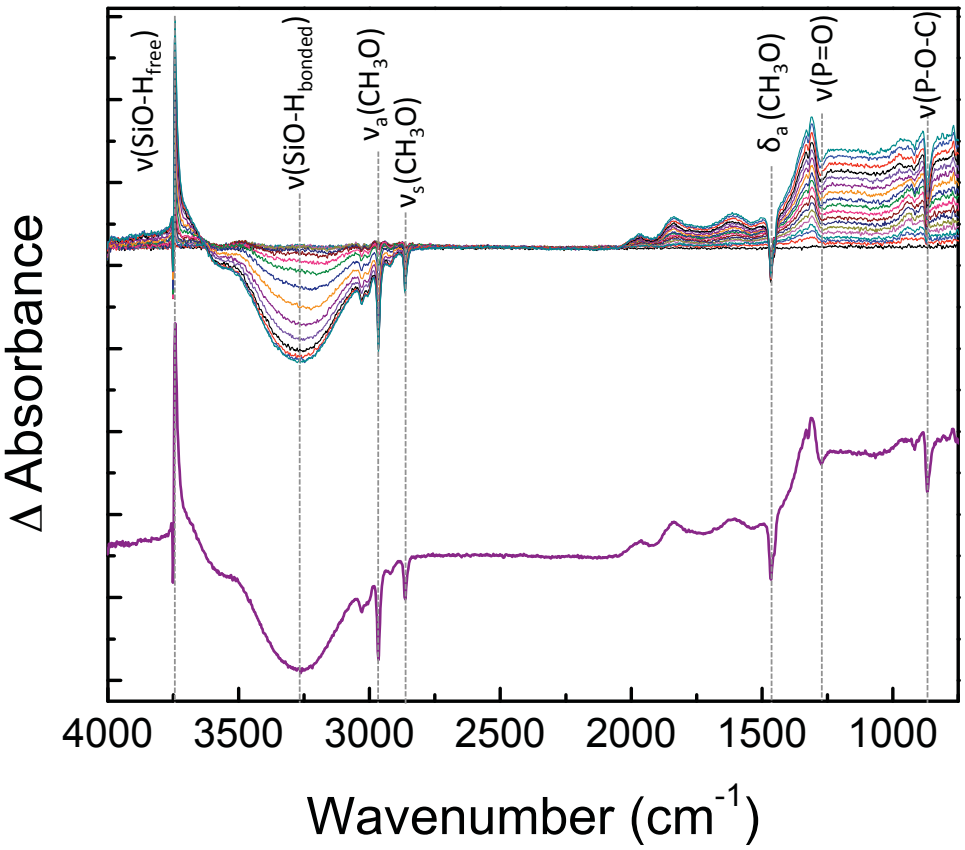

Figure 3.10: IR spectra of TMP-dosed sample during TPD. The final spectrum taken during the heating is offset for clarity.

Table 3.3. Mode assignments for TMP in the gas phase and adsorbed to silica.(* modes are unobservable in the adsorbed phase due to strong silica absorption.)

Mode	$TMP_{(g)}$	$TMP_{(ads)}$
$Si(O-H)_{free}$	--	3748
$Si(O-H)_{bonded}$	--	3190
$\nu_a(CH_3O)$	2964	2963
$\nu_s(CH_3O)$	2862	2862
$\delta_a(CH_3O)$	1465	1464
$\delta_s(CH_3O)$	1453	1454
$\nu(P=O)$	1291	1274
$\nu_a(C-O)$	1059	*
$\nu(P-O-C)$	855	869

3.3.1.5 DMCP Adsorption

A major difference between the simulants presented thus far and Sarin is the lack of the halogen functionality in the simulants. To explore how a halogen affects the adsorption properties, DMCP was also investigated. IR spectra of the cooled silica sample (225K) were recorded during initial dosing DMCP. Figure 3.11 shows the IR difference spectrum of the silica sample after 24 minutes of DMCP dosing. The gas-phase spectrum of DMCP is provided for reference. The conversion of the free OH group at 3748 cm^{-1} to the hydrogen-bonding species at 3324 cm^{-1} shows that DMCP forms a hydrogen bond with the surface.

Again, there are minimal shifts of the stretching and deformation modes of the methoxy groups relative to the gas phase. The phosphoryl group stretch which is at 1309 cm^{-1} in the gas phase, is slightly red shifted to 1302 cm^{-1} even during the initial adsorption. The observation of this shift even at very cold temperatures may be possible if DMCP is more weakly adsorbed than TMP, which would increase the relative mobility of DMCP on the surface.

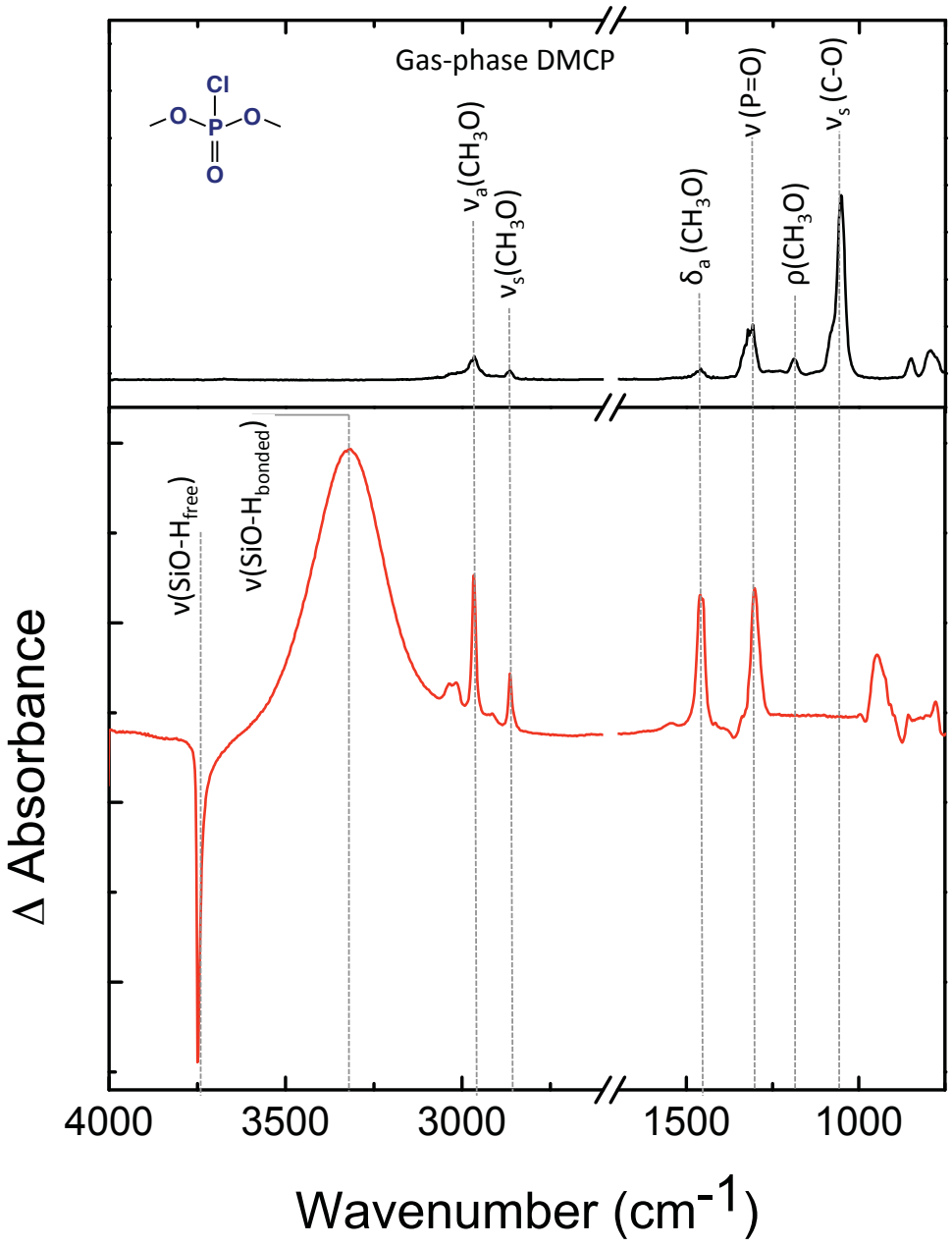

Figure 3.11: IR spectrum of DMCP adsorbed to a 225 K silica sample after 24 minutes of dosing. The reference spectrum is of the silica sample prior to simulant exposure.[77]

During the TPD shown in Figure 3.12, the free hydroxyl groups are regenerated as DMCP desorbs. All of the stretching and deformation modes of the methoxy groups remain in the same frequency positions, which indicates molecular adsorption and desorption. The phosphoryl stretch is even further red-shifted from its initial adsorption location to 1270 cm^{-1}

showing that the phosphoryl functionality of DMCP is the one that is most perturbed upon adsorption.

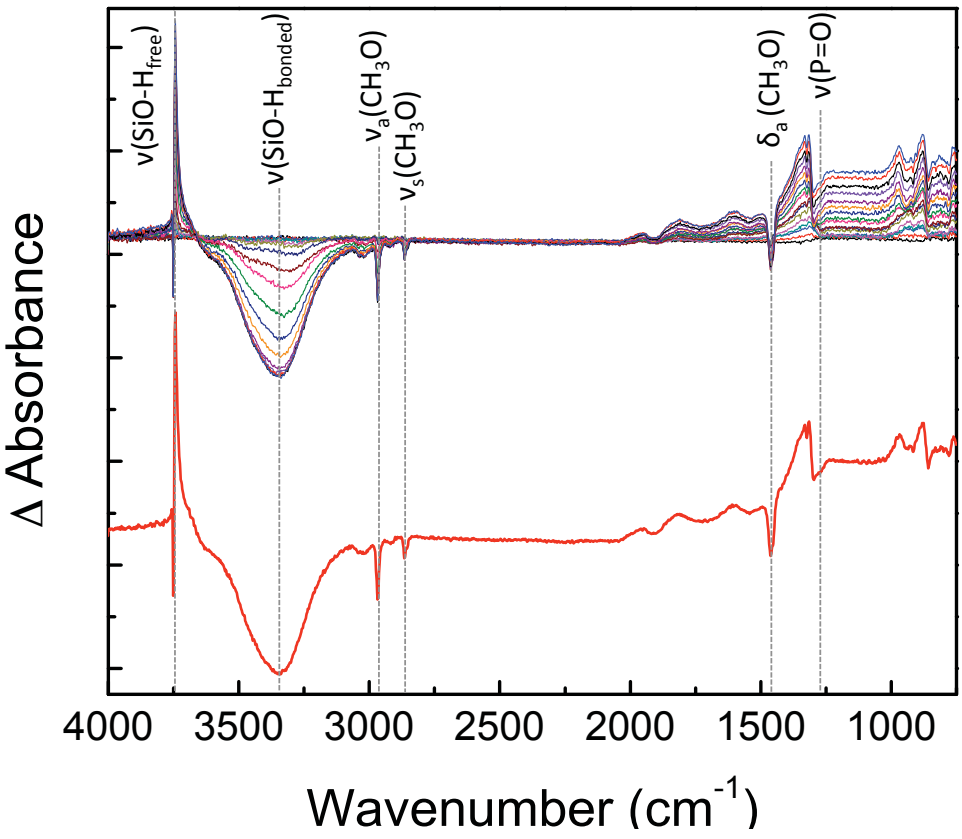

Figure 3.12: IR spectra of DMCP-dosed sample during TPD. The final spectrum taken during the heating is offset for clarity.

Mode	DMCP$_{(g)}$	DMCP$_{(ads)}$
Si(O-H)$_{free}$	--	3748
Si(O-H)$_{bonded}$	--	3324
ν$_a$(CH$_3$O)	2966	2968
ν$_s$(CH$_3$O)	2864	2862
δ$_a$(CH$_3$O)	1461	1461
δ$_s$(CH$_3$O)	1454	1454
ν(P=O)	1309	1270
ρ(CH$_3$O)	1190	*
ν$_s$(C-O)	1052	*
ν(P-O-C)	850	-

Table 3.4. Mode assignments for DMCP in the gas phase and adsorbed to silica.(* modes are unobservable in the adsorbed phase due to strong silica absorption.)

3.3.1.6 MDCP Adsorption

A second simulant with the halogen functionality chosen for this study was MDCP. IR spectra of the cooled silica sample (225K) were recorded during MDCP dosing. Figure 3.13 shows the IR difference spectrum of the silica sample after 24 minutes of MDCP dosing. The gas-phase spectrum of MDCP is also provided for reference.

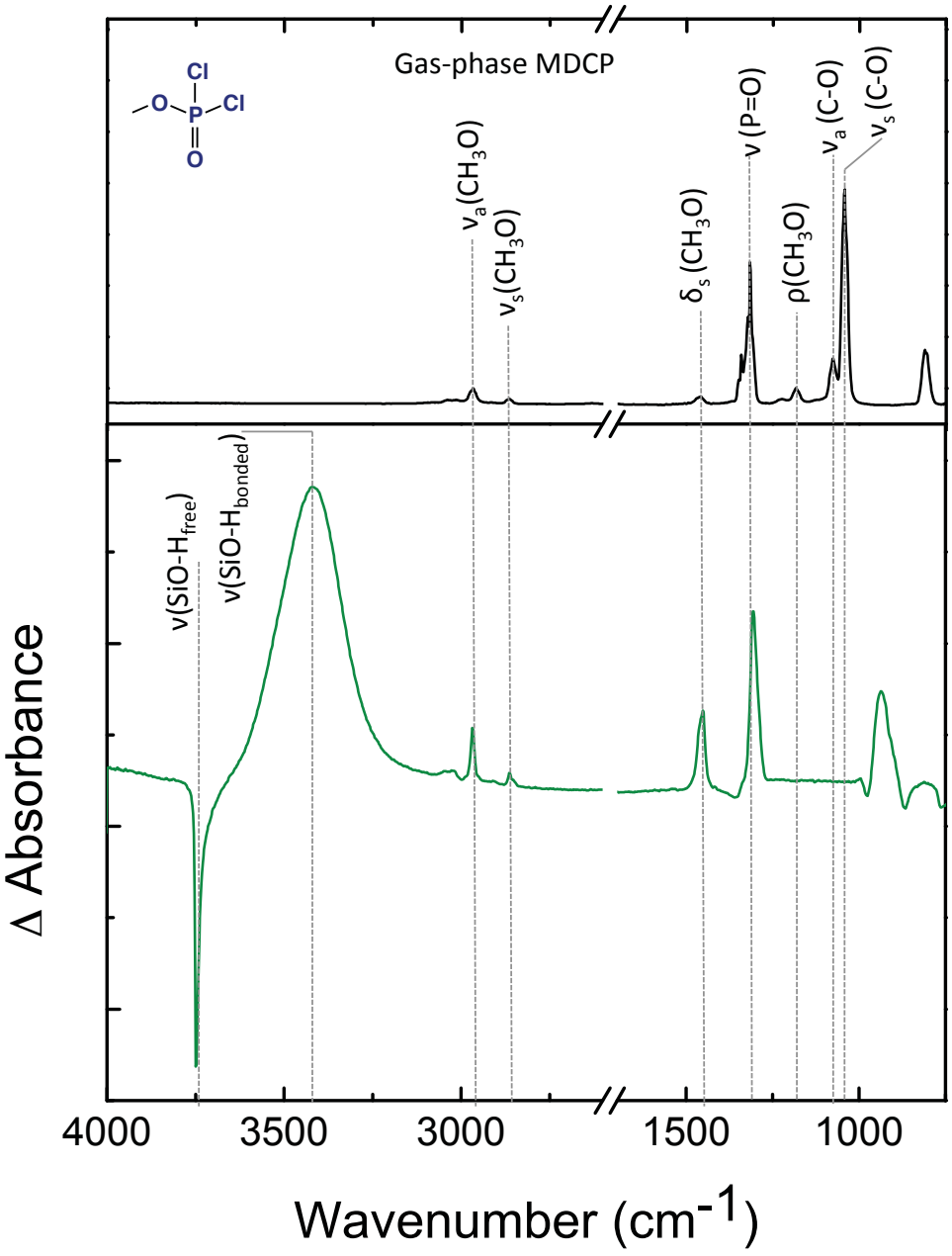

Figure 3.13: IR spectrum of MDCP adsorbed to a 225 K silica sample after 24 minutes of dosing. The reference spectrum is of the silica sample prior to simulant exposure.

Upon MDCP dosing, the free hydroxyl groups of silica at 3748 cm^{-1} are converted to a hydrogen-bonded species, which is red shifted to 3421 cm^{-1}. The modes of the methoxy group are shifted by only a few wavenumbers. The phosphoryl stretch is red-shifted from the gas phase by 9 cm^{-1}, from 1316 cm^{-1} to 1307 cm^{-1}, suggesting hydrogen-bond formation with the phosphoryl oxygen.

Using the TPD data for final peak assignments, the phosphoryl stretch is slightly further red shifted to 1304 cm^{-1}. All other MDCP modes remain near their gas-phase positions, which shows that MDCP adsorbs and desorbs molecularly.

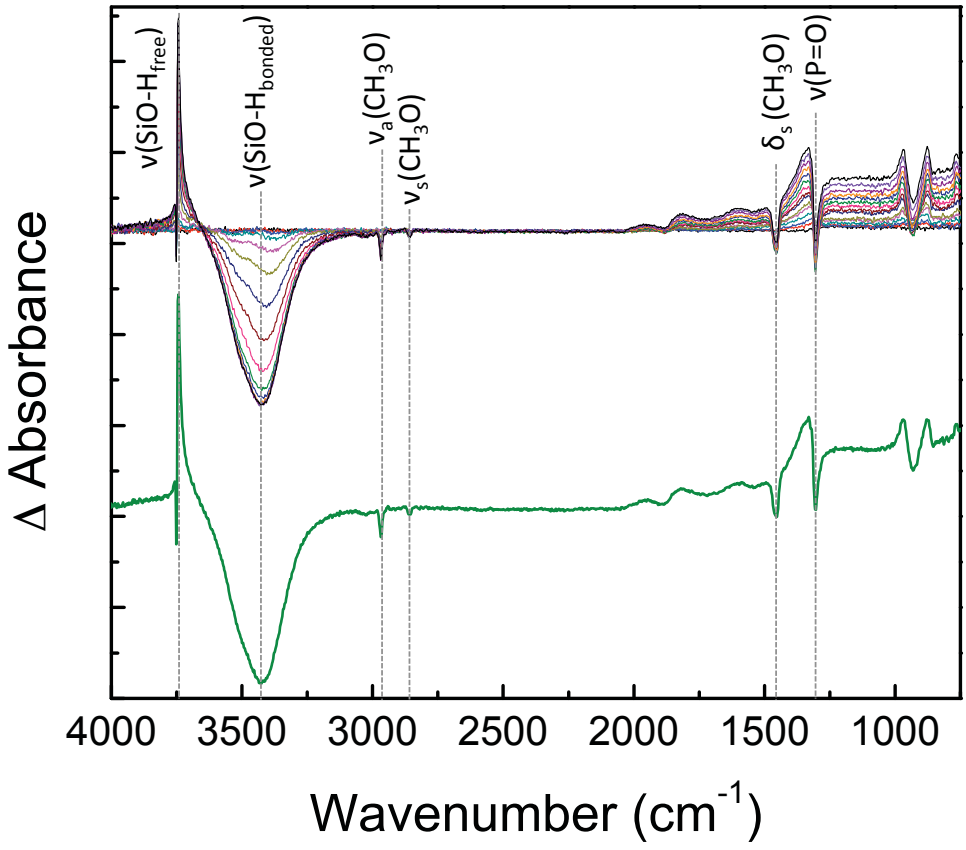

Figure 3.14: IR spectra of MDCP-dosed sample during TPD. The final spectrum taken during the heating is offset for clarity.

Table 3.5. Mode assignments for MDCP in the gas phase and adsorbed to silica.(* modes are unobservable in the adsorbed phase due to strong silica absorption.)

Mode	$MDCP_{(g)}$	$MDCP_{(ads)}$
$Si(O\text{-}H)_{free}$	--	3748
$Si(O\text{-}H)_{bonded}$	--	3421
$\nu_a(CH_3O)$	2967	2970
$\nu_s(CH_3O)$	2866	2859
$\delta_s(CH_3O)$	1452	1452
$\nu(P{=}O)$	1316	1304
$\rho(CH_3O)$	1184	*
$\nu_a(C\text{-}O)$	1077	*
$\nu_s(C\text{-}O)$	1044	*
$\nu(P\text{-}O\text{-}C)$	812	-

As observed for the other organophosphates presented, MDCP hydrogen bonds to the free surface hydroxyls of the silica through the simulants' phosphoryl oxygen.

3.3.1.7 Simulant Comparisons

To learn the rate of uptake of simulant on silica, the consumption of the free OH groups was monitored while dosing each simulant for 24 minutes while maintaining a constant pressure in the chamber of 1 x 10^{-6} torr. Figure 3.15 shows the integrated absorbance of the free OH peak (3800 to 3625 cm^{-1}) from the IR difference spectra as a function of dosing time. Fitting the data to the integrated first-order rate law shown in equation 4.2, provides an observed rate constant for adsorption.

$$\Delta A = Be^{-kt} \qquad 3.2$$

A is the integrated absorbance of the free OH peak, *B* is the preexponential factor, *k* is the observed rate constant, and *t* is time. From the kinetic data, all of the *k* values are between 1.1 x 10^{-3} and 1.8 x 10^{-3} s^{-1}, with no clear relationship between rate of uptake and adsorption strength. It is likely that at the cold silica surface temperature of 225 K, any simulant that hits the surface,

sticks to the surface. While this approach is helpful in obtaining a high local concentration of simulant, it makes kinetic analysis very difficult. Differences in the rate constants observed here are likely due to slightly different simulant fluxes.

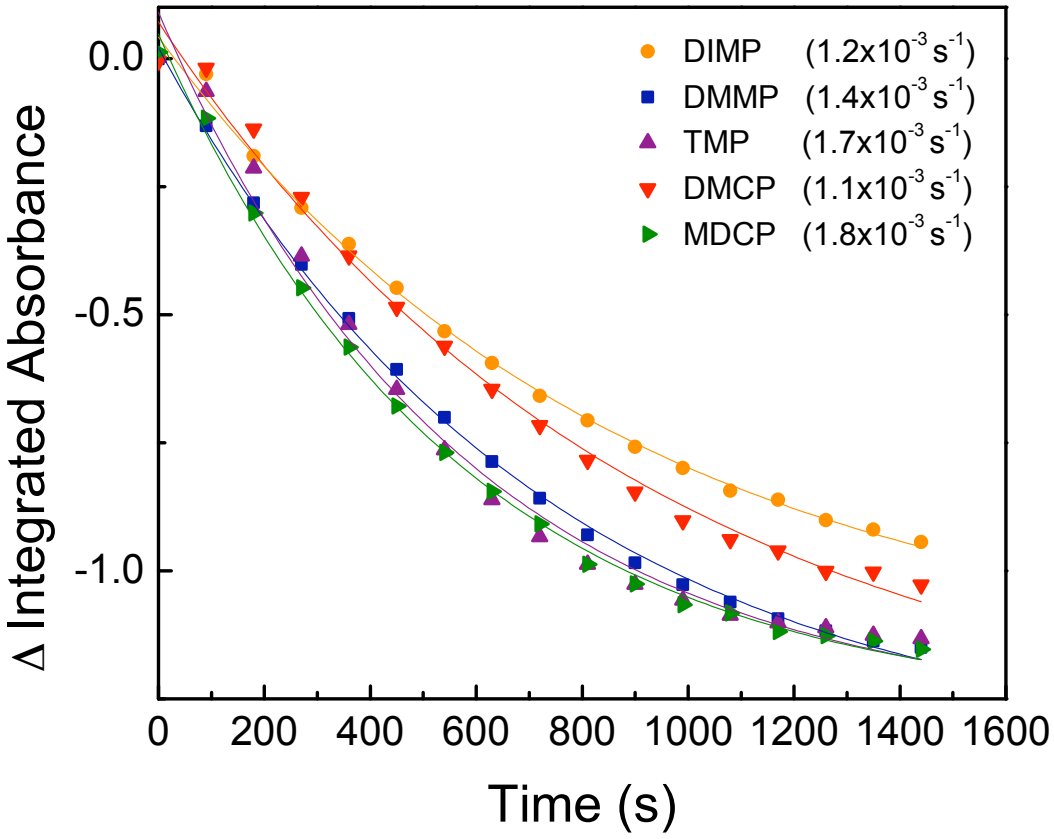

Figure 3.15: Integrated absorbances of the free hydroxyls of the silica surface as a function of dosing time. Solid lines are fits of the first order rate law. k_{obs} values are given in parentheses.

While the IR data show no clear difference in the behavior of the free hydroxyl group upon simulant adsorption, there is an observable difference in the peak for the hydrogen-bonded hydroxyl peak. When hydrogen bonding occurs, the ν(OH) mode is red-shifted to different frequencies for each simulant. In 1937, Badger and Bauer observed that the magnitude of this shift was linearly related to the hydrogen-bonding strength.[80] Many research groups have observed this relationship in solutions for a variety of different hydrogen-bond donor and

acceptor molecules. However, the relationship has yet to be investigated quantitatively for hydrogen-bonding systems at the gas-surface interface. Figure 3.16 shows the IR spectra of the silica sample with each of the G-series simulants. For the different simulants, there is a clear difference in the magnitude of the ν(O-H) shift from the free to hydrogen-bonded species. If the Badger-Bauer relationship applies here, it can be expected that the relative adsorption strengths to silica is DIMP>DMMP>TMP>DMCP>MDCP.

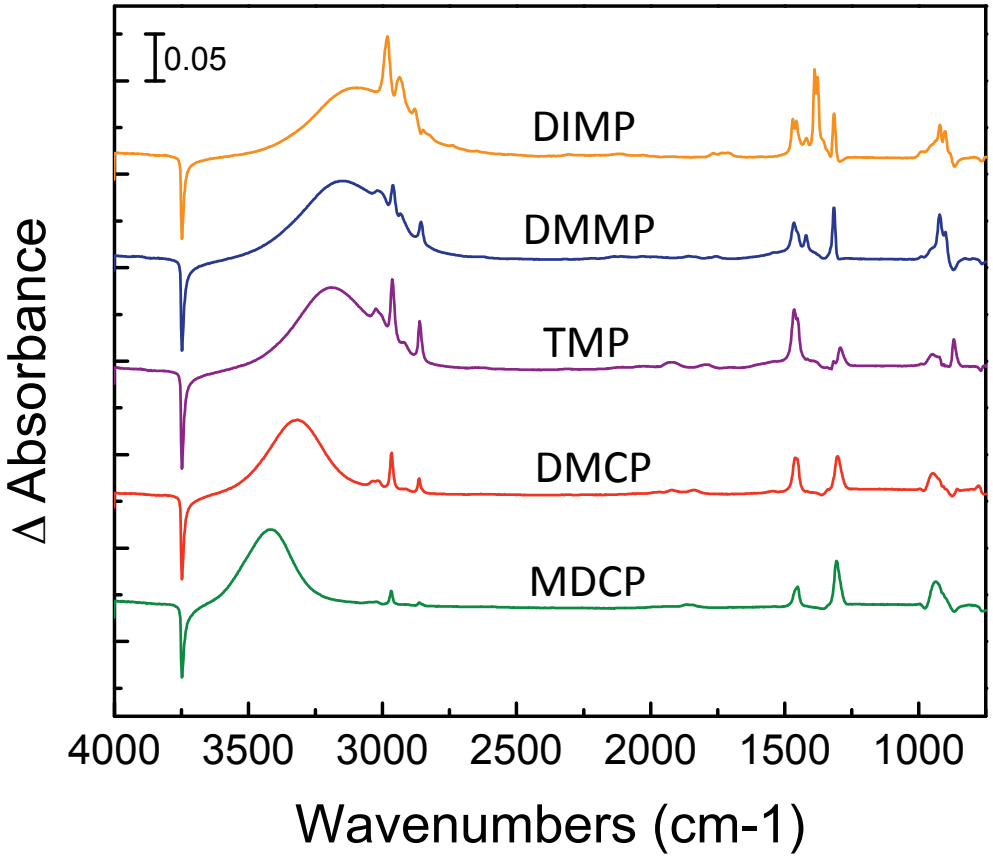

Figure 3.16: IR spectra of 225 K silica surface dosed with each simulant for 24 minutes.

3.3.2 Temperature-Programmed Desorption Studies

To quantitatively measure the simulant activation energy for desorption, TPD experiments were conducted. TPD experiments can also offer information regarding reaction order and surface heterogeneity. For all of the TPD experiments, the mass spectrometer was used to measure simulant desorption rate. Figure 3.17 on the following page shows the full mass spectra for each simulant. Mass spectral data recorded during simulant dosing and desorption were nearly identical for a given simulant, with the only significant difference being overall signal intensity. The identical cracking pattern and ratio of peak intensities is consistent with the molecular desorption of the simulants from the silica surface. While, all major cracks had the same behavior, only the most intense fragment was used in the data analysis.

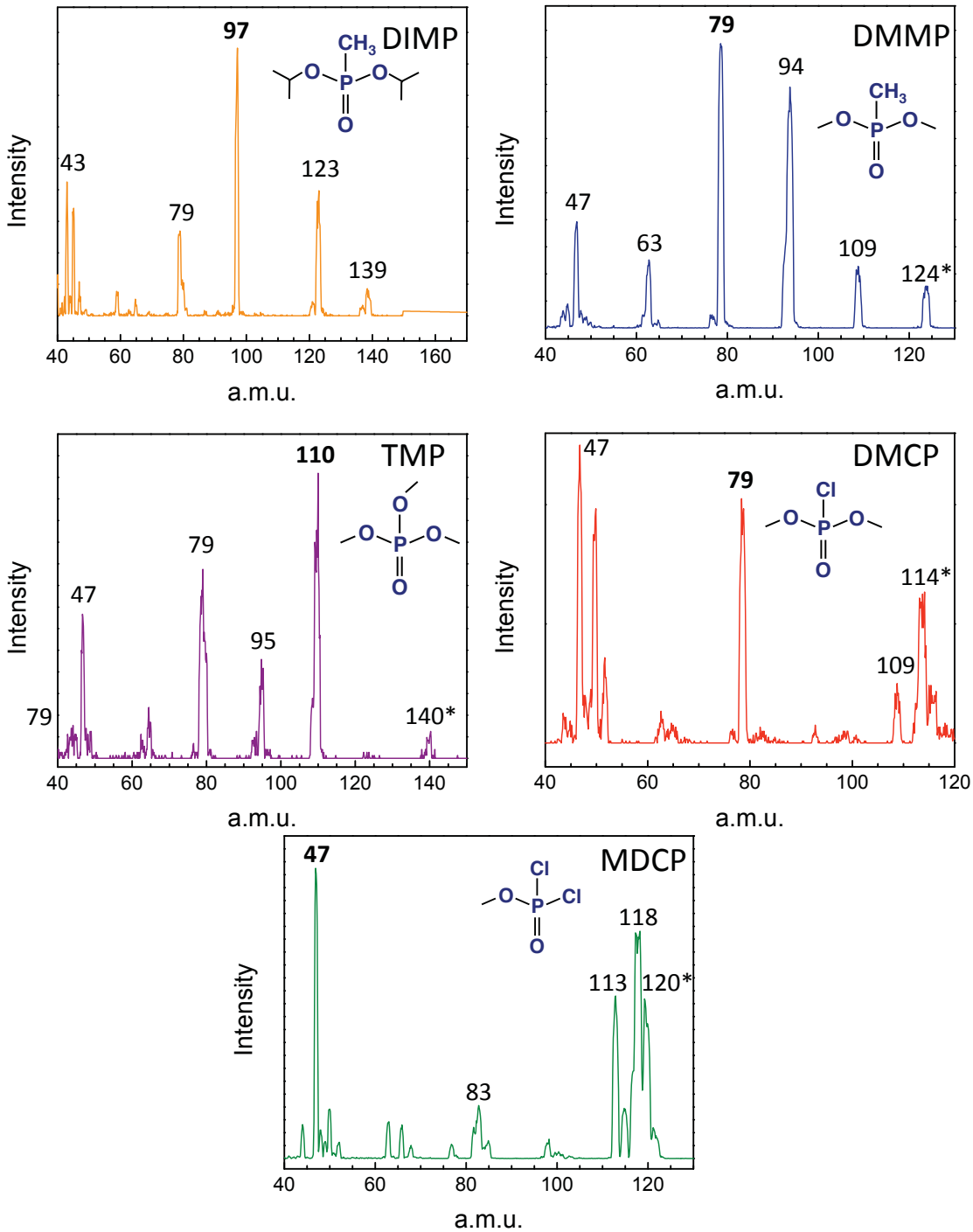

Figure 3.17: Mass spectra of the organophosphonate simulants. The most intense fragment for each simulant, denoted by bold text, was used in data analysis. The starred mass is the parent ion.

3.3.2.1 Redhead Analysis

One of the most popular TPD approaches to measure desorption energy utilizes a Redhead analysis of the desorption data.[81] In the Redhead approach, multiple TPD experiments are conducted beginning with same initial adsorbate coverage and the surface is heated at different linear ramp rates. The only data needed from the experiment is the temperature of the maximum desorption rate, T_p, or the peak of the spectrum. The desorption rate, r_d, can be expressed by an n^{th} order rate law given by equation 3.3, where Θ is coverage, t is time, and k_n is the rate constant.

$$r_d = -\frac{d\Theta}{dt} = k_n \cdot \Theta^n \qquad 3.3$$

Using the rate constant, k_n, given by the Arrhenius equation (equation 3.4)

$$k_n = \nu_n \cdot \exp\left(-\frac{\Delta E_d}{RT}\right) \cdot \Theta^n \qquad 3.4$$

affords the Polanyi-Wigner (PW) equation (equation 3.5) where ν is the prefactor, E_d is desorption energy, and R is the gas constant.

$$r = -\frac{d\Theta}{dt} = \nu_n(\Theta) \cdot \exp(-\frac{\Delta E_d(\Theta)}{RT}) \cdot \Theta^n \qquad 3.5$$

Because the surface is heated at linear rate, equation 3.6 is substituted into the PW equation where β is equal to the heating rate.

$$dt = \frac{1}{\beta} \cdot dT \qquad 3.6$$

Rearrangement and taking the natural log of both sides of equation 3.4 results in equation 3.7

$$\ln\frac{T_p^2}{\beta} = \frac{\Delta E_d}{RT_p} + \ln\frac{\Delta E_d}{\nu \cdot R} \qquad 3.7$$

By making a plot of $\ln(T_p^2/\beta)$ vs. $1/T$, the desorption energy is determined from the negative slope of the best fit line and the prefactor is calculated from the y-intercept.

Our first TPD experiments were conducted with DIMP adsorbed to a room temperature silica sample. The initial coverage was identical for each trial. Figure 3.18 shows five TPD spectra of DIMP on silica conducted at different heating rates. With increasing ramp rate, the T_p, the temperature of maximum desorption shifts to higher temperatures. The more time an

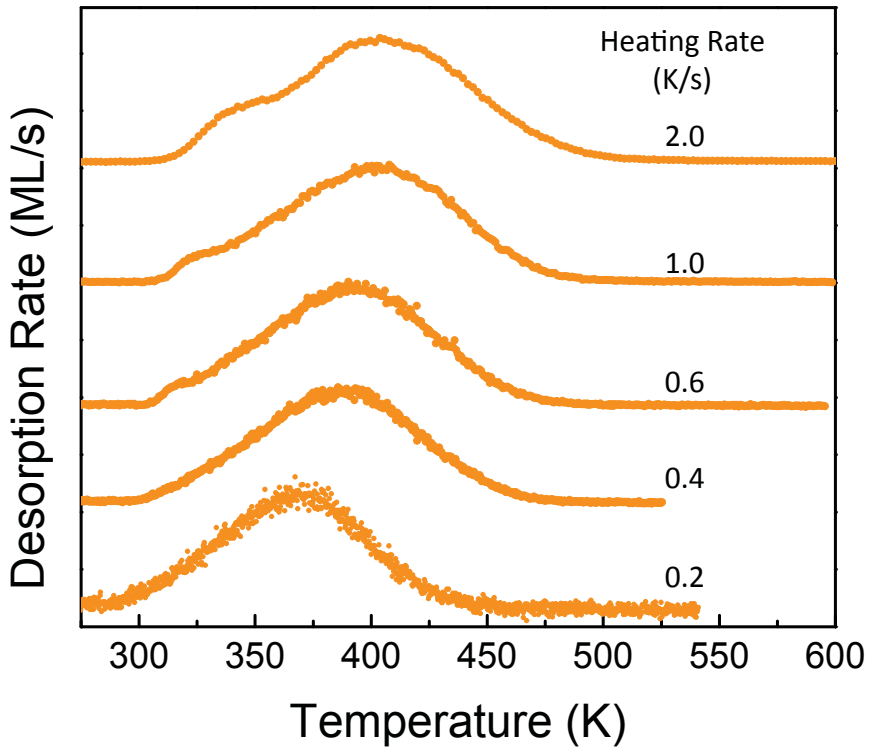

Figure 3.18: TPD profiles of DIMP adsorbed to room temperature silica. The initial coverage was kept the same for each run, while the heating rate was varied.

adsorbate spends at a given temperature, the higher the probability is for the adsorbate to desorb. In addition to the peak shift, a second peak begins to appear as the heating rate increases. For the two slowest rates, 0.2 and 0.4 K/s, each spectrum contains only a single peak, as expected for

desorption from one type of surface site. Beginning at 0.6 K/s, an early shoulder begins to develop. This shoulder continues to grow in intensity as the heating rate is increased. Typically in TPD experiments, a second peak indicates that there are two distinct adsorption strengths, such as multilayer vs. monolayer or step vs. terrace surface sites. However, the multiple features are typically present over a range of ramp rates, as opposed to the data of Figure 3.18 where they are only observed at the faster ramp rates.

Kubkov et al. conducted TPD experiments investigating the adsorption, diffusion, and desorption of nitrogen from thin (<1 μm) and thick (>1 μm) films of amorphous water. [74] They conducted TPD experiments on both films at heating rates of 0.006, 0.06, 0.6, and 6 K/s and the resulting spectra are shown in Figure 3.19. For the thin films, single peaks were observed for all heating rates and the desorption profiles followed Polanyi-Wigner kinetics for all but the fastest heating ramp. However, for the thick film, single peak behavior was only observed for the two slowest ramps and desorption followed Polanyi-Wigner kinetics for only the slowest ramp. They attribute these observations to diffusion-limited kinetics in thick films.

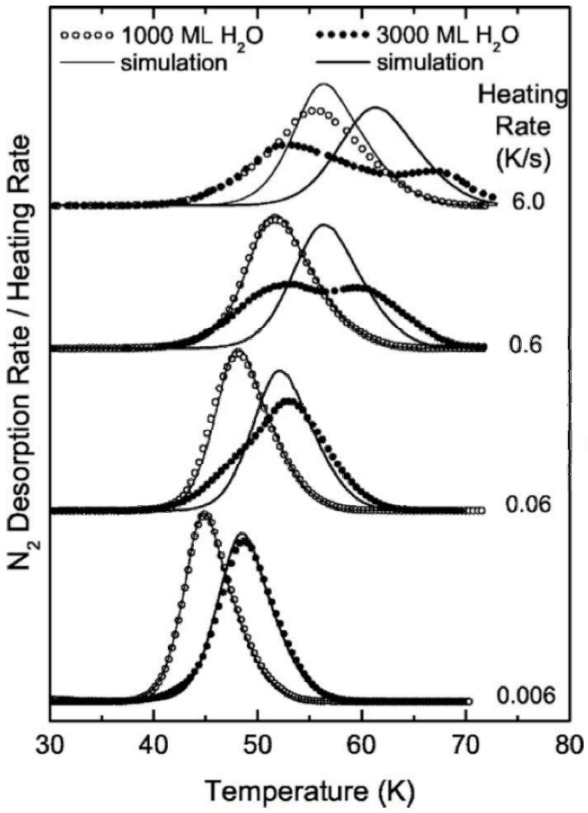

Figure 3.19: TPD profiles of N_2 on thin and thick films of amorphous water. Solid lines are simulated spectra and describe desorption according to the PW equation. Reprinted with permission from Zubkov *et al. J. Chem. Phys.* 2007*, 127(18)*, 184708. Copyright 2007, American Institute of Physics.

Comparing Kubkov's data to the TPD spectra of Figure 3.18, it appears that the silica sample used in our work is thick enough that at the faster ramp rates, desorption may become diffusion-limited. Kubkov explains that in the thick films, a non-uniform distribution of the adsorbate is responsible for producing the bimodal behavior. In order to study desorption without diffusion effects on thick samples, it is necessary to conduct the TPD experiments with only very slow ramp rates. With a slow ramp rate, it becomes possible to maintain a uniform distribution of adsorbates throughout our 50 μm thick silica sample.

Proper application of the Redhead analysis requires the use of ramp rates that vary by at least one order of magnitude and, for extremely accurate data analysis, a span of two orders of magnitude is preferred. Because elevated heating rates produced diffusion-related artifacts in the TPD spectra, a Redhead analysis is not an appropriate approach for learning the adsorption strength of organophosphates on a thick amorphous silica sample.

3.3.2.2 Inversion Analysis

Another common TPD method utilizes inversion analysis. For the inversion analysis experiments, the same slow heating rate is used for all trials, but the initial adsorbate coverage is varied. An advantage of the inversion analysis approach is that the entire TPD spectrum is used in determination of the desorption energy, not just a single temperature value as is the case in the Redhead analysis. According to the inversion analysis, the desorption rate, simply the mass spectrometer signal during TPD, can be described by the PW equation, as in the Redhead analysis.

$$r = -\frac{d\Theta}{dt} = \nu_n(\Theta) \cdot \exp(-\frac{\Delta E_d(\Theta)}{RT}) \cdot \Theta^n \qquad 3.5$$

where Θ is coverage, t is time, T is temperature, ν is the pre-exponential factor (prefactor), E_d is desorption energy, R is the gas constant, and n is desorption order (n=1 for the first-order

desorption of simulant from silica). Rearrangement of the PW equation provides the desorption energy as a function of coverage. In Equation 3.8, the prefactor, ν, is assumed to be independent

$$E_d(\Theta) = -k_B T \ln\left(-\frac{d\Theta/dt}{\nu\Theta}\right) \qquad 3.8$$

of coverage and temperature. Numerical integration of this curve can then provide a simulated set of desorption spectra for lower initial adsorbate coverages. The prefactor is then treated as a variational parameter to provide minimal error between the experimental and simulated TPD spectra. Final agreement of the experimental and simulated spectra confirms applicability of the PW equation, which then provides the desorption energy.

Figure 3.20 shows the TPD spectra of five different initial DMMP coverages. The integral of each TPD spectrum is proportional to the adsorbate coverages. We have defined that a saturated surface, Θ = 1 ML, corresponds to the consumption of every free OH group on the surface.

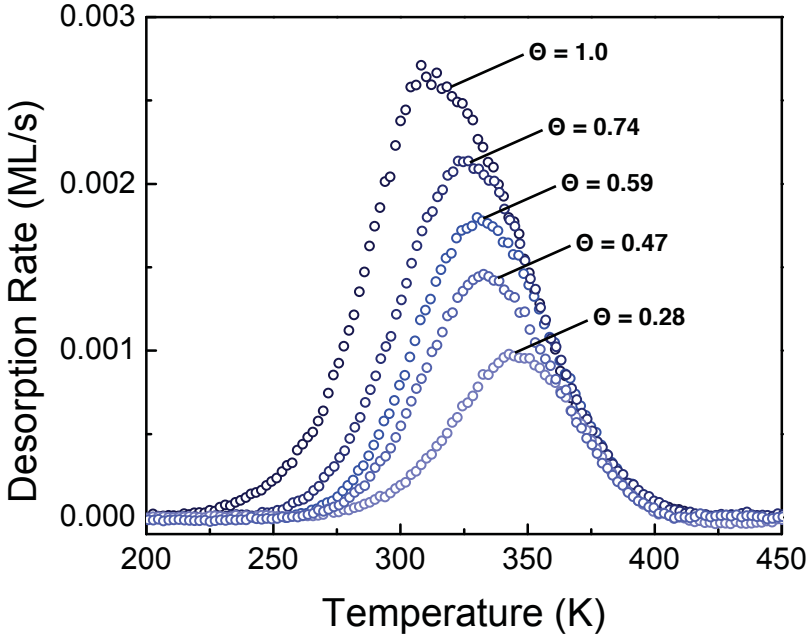

Figure 3.20: TPD spectra of 5 different initial coverages of DMMP (m/z=79) using a heating rate of 0.2 K/s. Initial DMMP coverages are 1.0, 0.74, 0.59, 0.47, and 0.28 ML.

As the initial adsorbate coverage was lowered, the peak area decreased. The integral of a TPD spectrum is proportional to the simulant coverage so the lower intensity spectra are those with lower initial simulant coverages. Also, as the coverages were lowered, the maximum desorption rate temperature, T_p, is shifted to higher temperatures. This temperature shift can provide valuable information about the physical processes on the surface. The T_p shift to higher temperatures with decreasing coverages, as we observe, can describe two distinct scenarios. Firstly, a surface in which there are strong adsorbate-adsorbate interactions can shift the T_p to higher temperatures. A second situation producing the TPD behavior observed here, occurs when there is a distribution of surface sites. For our sample of low surface hydroxyl concentration (2 OH/nm^2) and packed amorphous silica nanoparticles, it is expected that the small distribution of surface sites causes the shift in T_p.

Another key feature of the TPD spectra of different DMMP coverages is the alignment of the high temperature tails. The alignment of the tails indicates that the adsorbates are mobile enough on the surface to find the strongest adsorption sites.[74] It is worth noting here that not all combinations of simulants and coverages provided neatly aligned TPD curves for the initial sample preparation conditions. If the annealing temperature were too low, the high temperature tails of two spectra with different initial coverages would not align, indicating a non-uniform initial distribution of simulant. In those cases, the annealing temperature was increased by 25K until the tails aligned.

The TPD spectra of Figure 3.20 contain information regarding the desorption properties, however the desorption energy is not easily interpreted. Therefore, a plot of desorption energy versus coverage is made by using the TPD data of the highest coverage run. Rearrangement of the PW equation results in equation 3.8, which shows desorption energy as a function of

simulant coverage. This curve (Figure 3.21) shows that there is a wide distribution of surface sites that DMMP adsorbs to with a variety of desorption energies. At low coverages, DMMP can adsorb to the strongest sites, and the desorption energy approaches 58 kJ/mol. At high coverages, where DMMP can only adsorb to the few remaining sites, the desorption energy is 47 kJ/mol. To determine the desorption energy for a single adsorbate on a defect-free surface, the linear region of the E_d curve can be extrapolated to zero coverage. For a single DMMP molecule adsorbed to silica, the activation energy for desorption is 54.5 ± 0.3 kJ/mol.

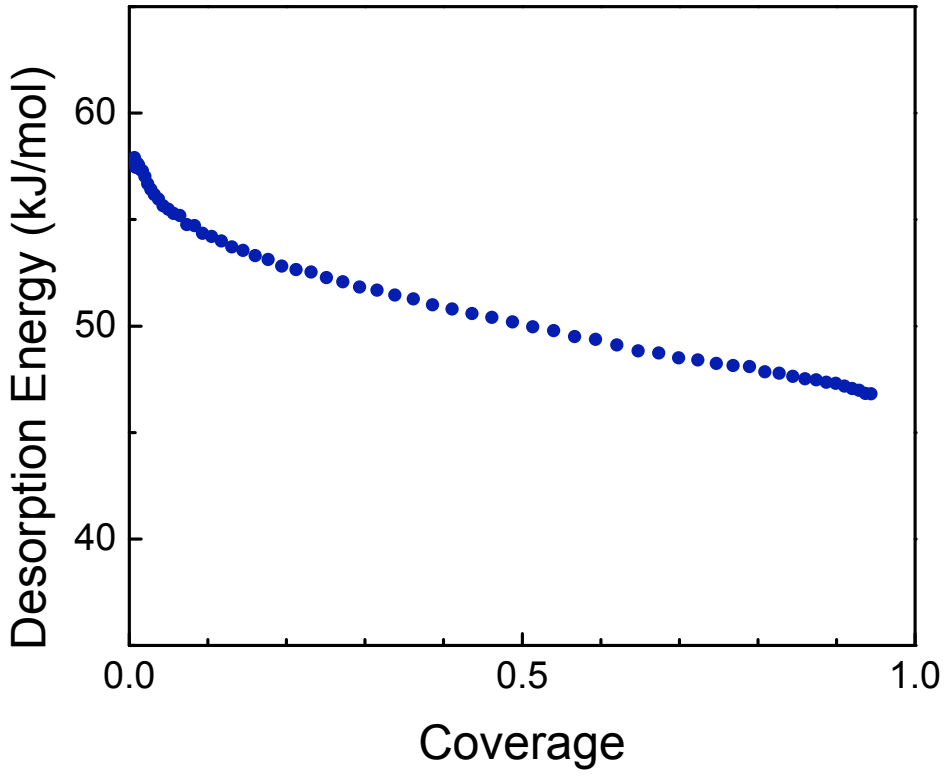

Figure 3.21: The desorption energy of DMMP adsorbed to silica as a function of coverage using a prefactor of 4.0 x 10^6 s^{-1}.[77]

From this primary E_d curve, any lower coverage TPD spectrum can be simulated simply through numerical integration of the E_d curve. Once the E_d curve is obtained, the only variational parameter left in the PW equation is the preexponential factor, ν. The prefactor is

often considered as attempt frequency, or how many times the molecule vibrates before desorbing from the surface. For single crystals, typically a prefactor of 10^{13} s^{-1} is assumed as it is on the order of molecular vibrations. Within transition state theory, the prefactor is related to the entropy of the adsorbate in the gas phase compared to the entropy of the transition state. Experimentally determined prefactors have been shown to vary from as low as $10^{3}s^{-1}$ up to $10^{20}s^{-1}$.[82]

Diffusion effects can also have a large impact on the prefactor. In the field of catalysis, thick sorbent particle beds are often used for TPD measurements. Gorte observed that in these systems the prefactor may fall below 10^{13} s^{-1} by several orders of magnitude.[83] Referring back to the PW equation, we can see that the correct determination of the prefactor has a significant impact on the resulting desorption energy. Figure 3.22 shows the experimental and simulated data with 3 different prefactor choices. The appropriate prefactor was determined by minimizing

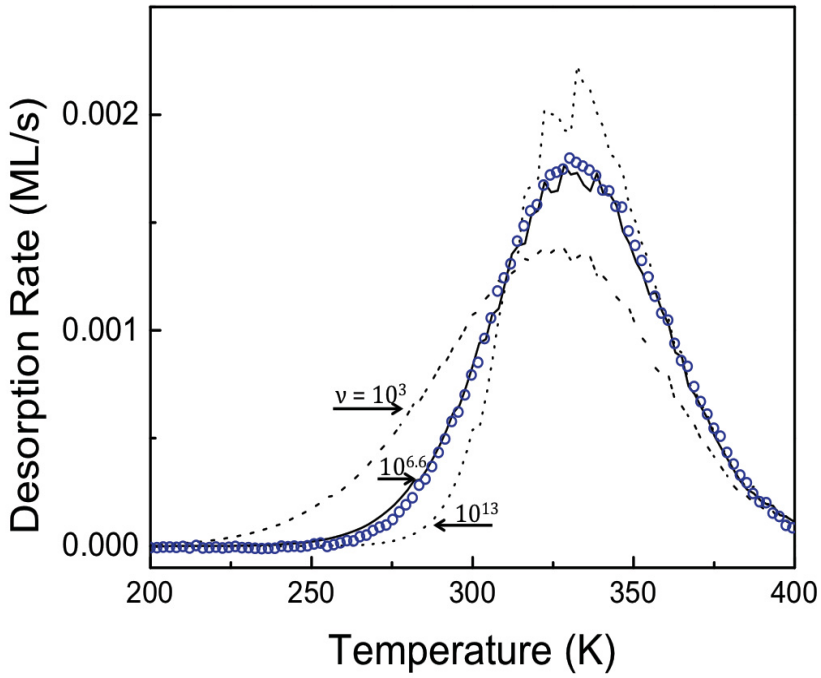

Figure 3.22: Experimental TPD profile of DMMP on silica (blue circles) and simulated fits using three different prefactrs: 1 x 10^{3}, 4 x 10^{6}, and 1 x 10^{13} s^{-1}.

the sum-of-squares of the residuals between the simulated TPD spectra and the experimental data. The prefactors were determined for each simulant independently and were found to be the same within our experimental error. For G-simulants, it was determined that $\nu = 4 \times 10^{6\pm0.8} s^{-1}$ provides the best agreement between the simulated and experimental TPD data.

Confirmation that Polanyi-Wigner desorption kinetics appropriately models our system is shown by the excellent agreement between the experimental and simulated TPD spectra. Figure 3.23 shows five experimental TPD spectra of DMMP adsorbed to silica, as well as the simulated TPD spectra. As discussed previously, when the initial coverage is decreased, the TPD curve shifts to higher temperatures because the adsorbates locate the strongest available sites. The simulated spectra, coming from the inversion analysis of the desorption energy curve (Figure 3.21) appropriately model this behavior.

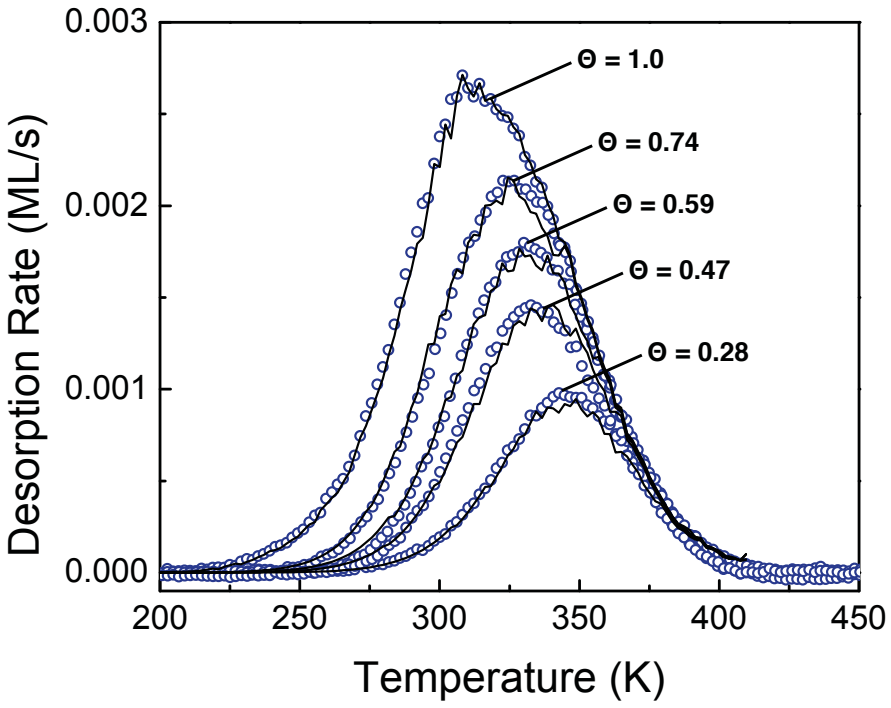

Figure 3.23: Experimental TPD data for five different initial coverages (open circles) and simulated spectra (solid lines) from inversion analysis; all shown with prefactor, $\nu = 4 \times 10^6\ s^{-1}$.[77]

Coverage dependent TPD studies were also completed for DIMP, TMP, DMCP, and MDCP and inversion analysis was preformed to simulate the lower coverage experiments. As with DMMP, excellent agreement between experimental and simulated data is observed, confirming correct prefactor choice and applicability of the PW equation for these systems.

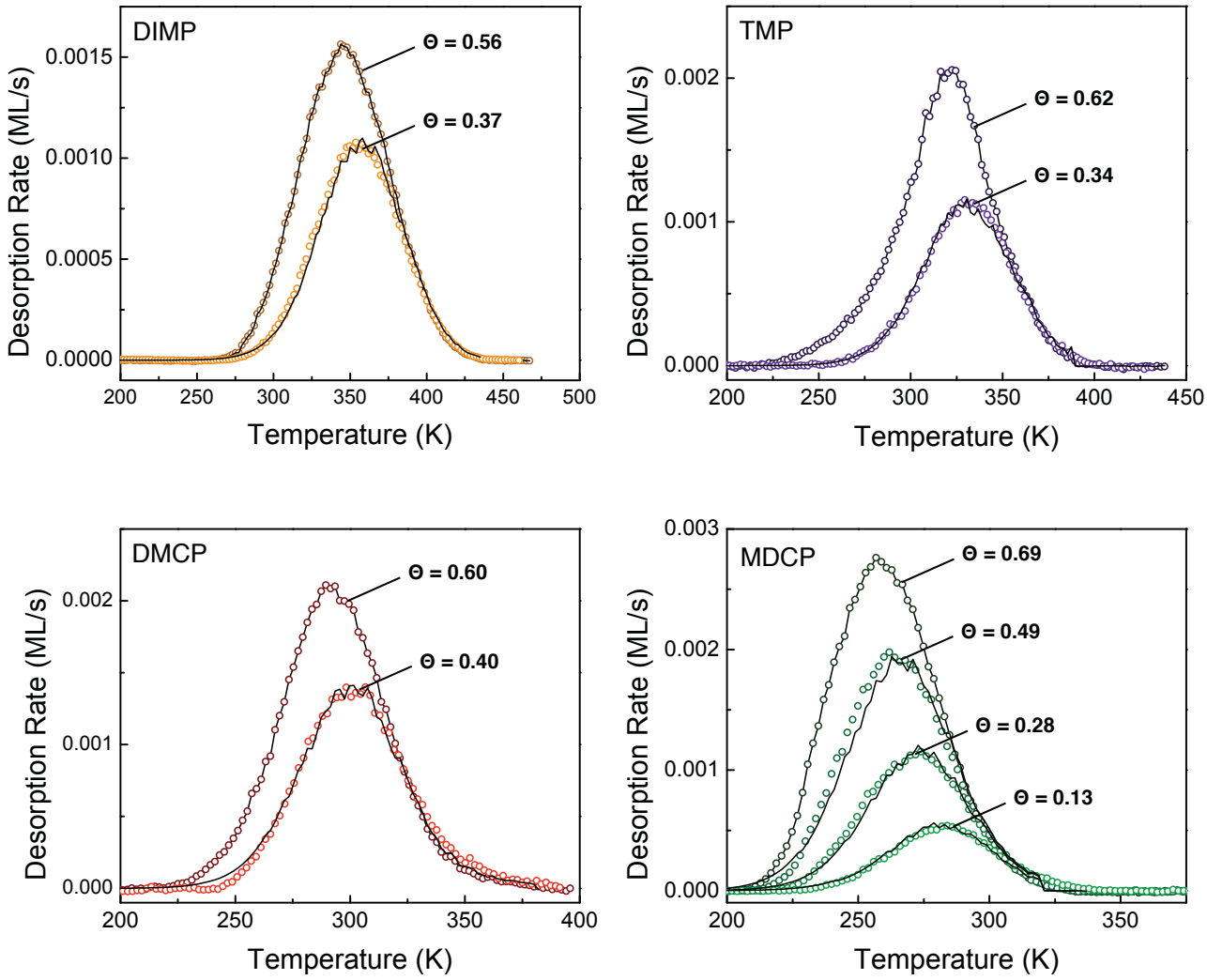

Figure 3.24: Experimental (open circles) and simulated (black lines) TPD profiles for DIMP, TMP, DMCP, and MDCP; all shown with prefactor, $\nu = 4 \times 10^6\ s^{-1}$.[77]

To qualitatively compare the desorption energy of the given simulants, we can compare the temperature required for desorption. Because the initial simulant coverage affects the desorption temperature, the simulated spectra for the same initial coverage of 0.5 ML was plotted (Figure 3.25). Based on the temperature required for desorption, we observe that the relative adsorption strength is the following:

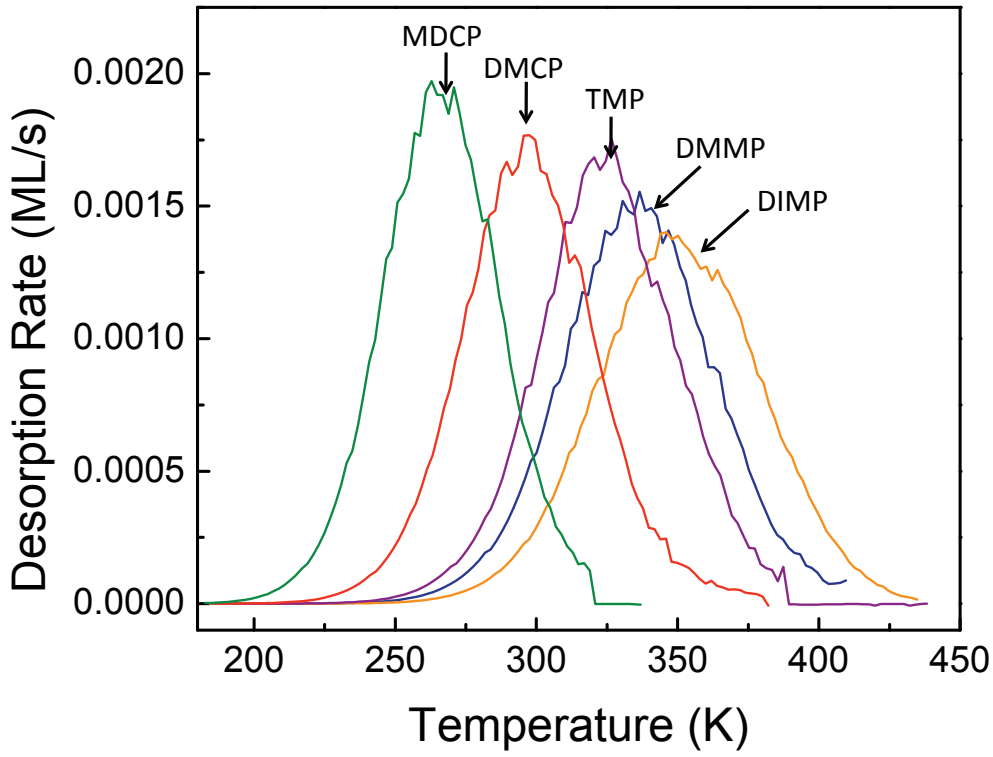

Figure 3.25: Simulated TPD spectra for DIMP, DMMP, TMP, DMCP, and MDCP for an initial coverage of 0.50ML.

DIMP>DMMP>TMP>DMCP>MDCP. This is the same trend as observed by measuring the shift of the SiO-H stretching frequency in the IR data shown previously.

In addition to the shift in temperature, the peaks become broadened for the more strongly adsorbed species. This broadening likely comes from readsorption effects within the silica sample. In order for an adsorbate to leave the silica sample it must desorb from its initial adsorption site; however before leaving the sample, it likely readsorbs to a different silanol site.

This desorption/readsorption process happens numerous times before the simulant leaves the surface and is detected with the mass spectrometer. DIMP has the highest activation energy for desorption from silica and therefore has the longest residence time, as given by equation 3.9 where τ is the residence time, ν is the pre-exponential factor, E_d is the desorption energy, R is the gas constant, and T is temperature.

$$\tau = \frac{1}{\nu}\exp(E_d/RT) \qquad 3.9$$

However, despite readsorption effects, desorption can still be described with Polanyi-Wigner desorption kinetics [84,85]

Using the rearranged PW equation, desorption energy as a function of coverage can be plotted for all of the simulants studied. Figure 3.26 shows the E_d curves for each simulant from zero coverage up to 0.5 ML. All of the curves have a similar shape and span about 5 kJ/mol. For a given simulant, the desorption energy is the lowest at high coverages because there are fewer adsorption sites available. At low coverage, there is a sharp increase in the desorption energy, which can be due to adsorption at uncharacteristically strong adsorption sites, which could either be defects in the silica sample or a location where multiple surface hydroxyls may participate in bonding to a single adsorbate. By extrapolating the linear region of each E_d curve back to the y-intercept we can determine the activation energy for desorption of a single adsorbate in the absence of surface defects. The desorption energy for DIMP is the highest at 57.9 ± 1 kJ/mol. The other simulants, DMMP, TMP, DMCP, and MDCP have desorption energies of 54.5 ± 0.3, 52.4 ± 0.6, 48.4 ± 1, and 43.0 ± 0.8 kJ/mol respectively.

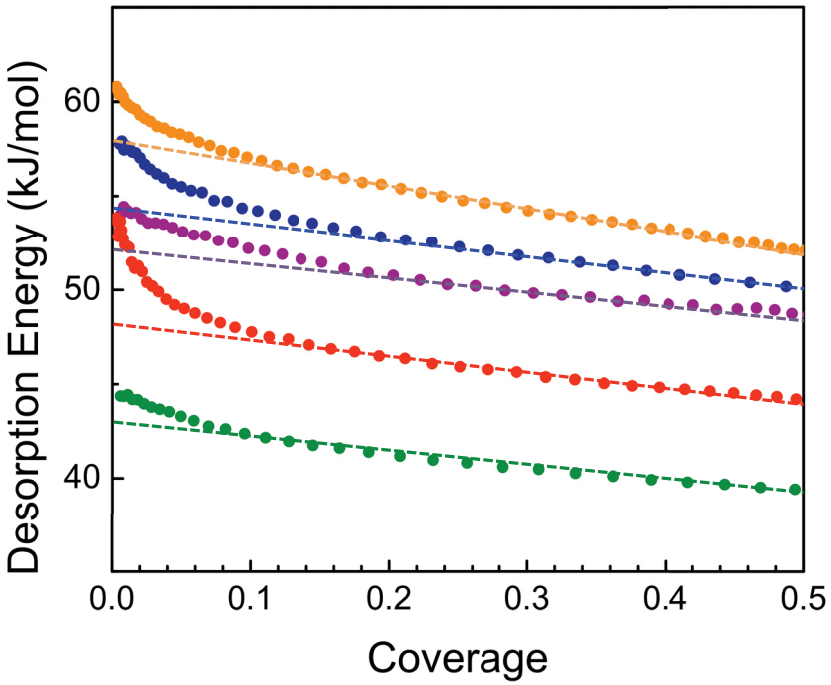

Figure 3.26: Desorption energy as a function of coverage for DIMP, DMMP, TMP, DMCP, and MDCP on silica.[77]

The Badger-Bauer relationship suggests that the measured desorption energy is directly related to the shift of the ν(OH) mode from the IR data.[80] If the empirical observation of Badger and Bauer can be applied to the hydrogen-bonding surface interactions of the organophosphates studied here, we would expect to see a similar linear relationship. Figure 3.27 shows the desorption energy as a function of ν(SiO-H) shift.

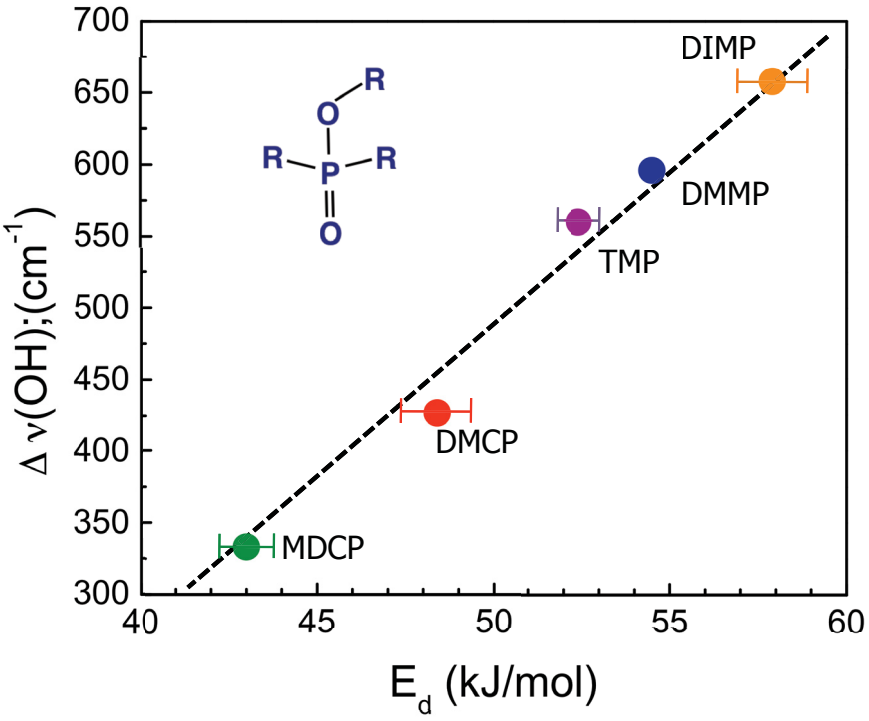

Figure 3.27: Frequency shift of the SiO-H stretching mode upon simulant adsorption as a function of desorption energies measured by TPD.

A more strongly adsorbing species causes a greater weakening of the SiO-H bond. The magnitude to which this O-H bond is weakened is indicated by the magnitude of the frequency shift. The linear relationship observed in Figure 4.27 indicates that the Badger-Bauer relationship can indeed be applied to the system presented here.

3.3.3 Computational Studies

The correlation between bond strength and frequency has been observed previously by Badger and Bauer for hydrogen-bonding systems in solution.[80] While it is clear that the Badger-Bauer relationship is observed for our series of organophosphates adsorbed to silica, it is not immediately apparent why specific substituents affect the adsorption strength. Molecular size, electronegativity, charge, orientation, and polarizability could all play a role in determining the adsorption energy. In order to learn which component of molecular structure had the strongest influence on the adsorption geometry and strength, the experimental TPD measurements were

complemented with computational studies. The Badger-Bauer relationship tells us that the adsorption strength is directly related to the hydrogen-bonding interaction with the silica. Therefore, we will focus on how the phosphoryl substituent, the functionality responsible for hydrogen bonding to the silica surface, is affected by the other substituents.

Figure 3.28 shows the optimized structures of each of the simulants and the Mulliken atomic charges of the phosphorus and oxygen atoms calculated at the MP2/cc-pVTZ//MP2/6-31G* level. One possibility for the difference in adsorption strength is the magnitude of the P=O

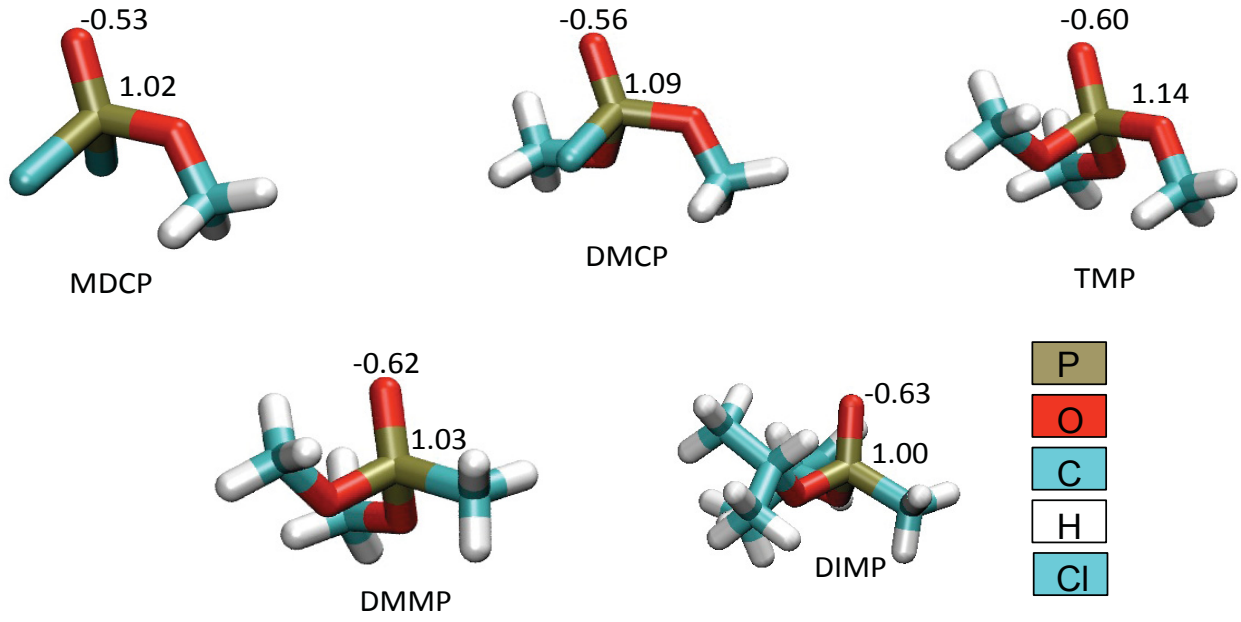

Figure 3.28. Optimized simulant structures and atomic charges calculated at the MP2/cc-pVTZ//MP2/6-31G* level.

dipole. A large dipole of the P=O bond would make oxygen a more effect hydrogen-bond acceptor and increase the simulant adsorption strength. However, comparing the difference in charges between the O and P atoms for each molecule, there is no trend consistent with the adsorption strength data. Looking at just the oxygen atom, we see that the magnitude of this charge is directly related to the simulant adsorption strength. A plot of both the shift of the ν(OH) mode and the calculated negative charge on the phosphoryl oxygen as a function of

experimentally determined desorption energy is shown in Figure 3.29. Again, a linear relationship is observed suggesting that desorption energy depends directly on the electron on the

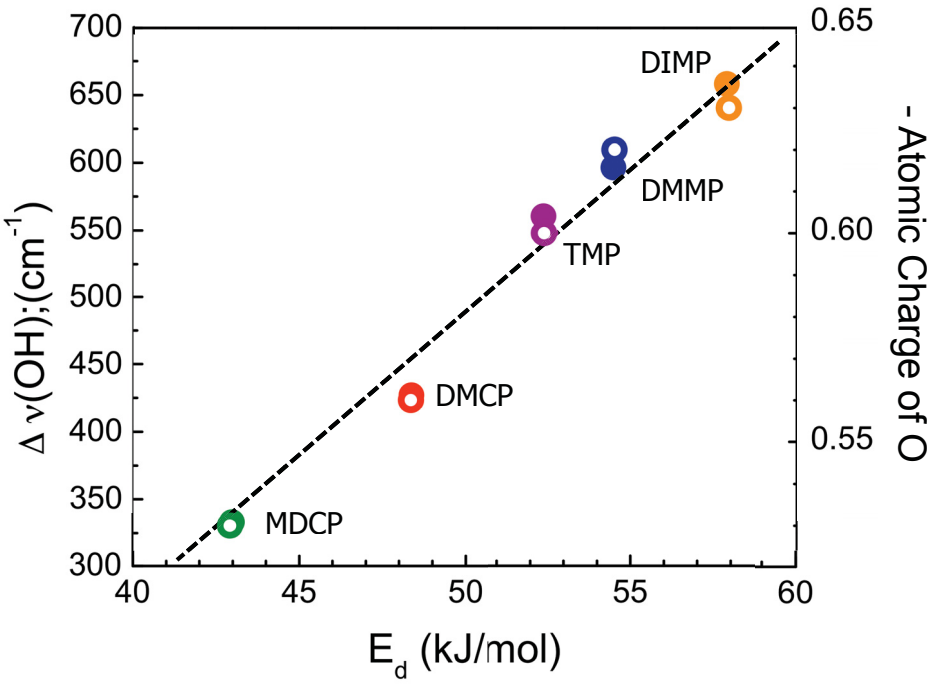

Figure 3.29. Frequency shift of the SiO-H stretching mode upon simulant adsorption (closed circles) and calculated magnitude of the negative charge on the oxygen atom (open circles) as a function of desorption energies measured by TPD.

density on the phosphoryl oxygen atom. More negative charge on the oxygen atom increases its ability to be a hydrogen-bond acceptor and increases the energy required for desorption.

Again, contributing to our experimental results, the adsorption strength of the simulants adsorbed to silanols groups were investigated computationally. The interaction of each simulant with a single silanol ($Si(OH)H_3$) was investigated at the MP2/cc-pVTZ//MP2/6-31G* level (structures shown in Figure 3.30). Both the BSSE corrected bonding strength and the shift of the ν(SiO-H) mode were calculated and the results are shown in table 3.6. The hydrogen-bond strengths determined by theory follow the identical trend of the energies measured

experimentally. However, the calculated bond strengths are all lower than the experimental values. Some of the energy difference is likely due to van der Waals interactions that are not accounted for in the calculations. Typical van der Waals interactions may be as high as 10 kJ/mol. Also by using the cc-pVTZ basis set, it is impossible to describe all possible positions of the electrons so the calculated energies will always be an underestimate. Nonetheless, the trends for similar molecules are expected to be accurately represented by the calculations.

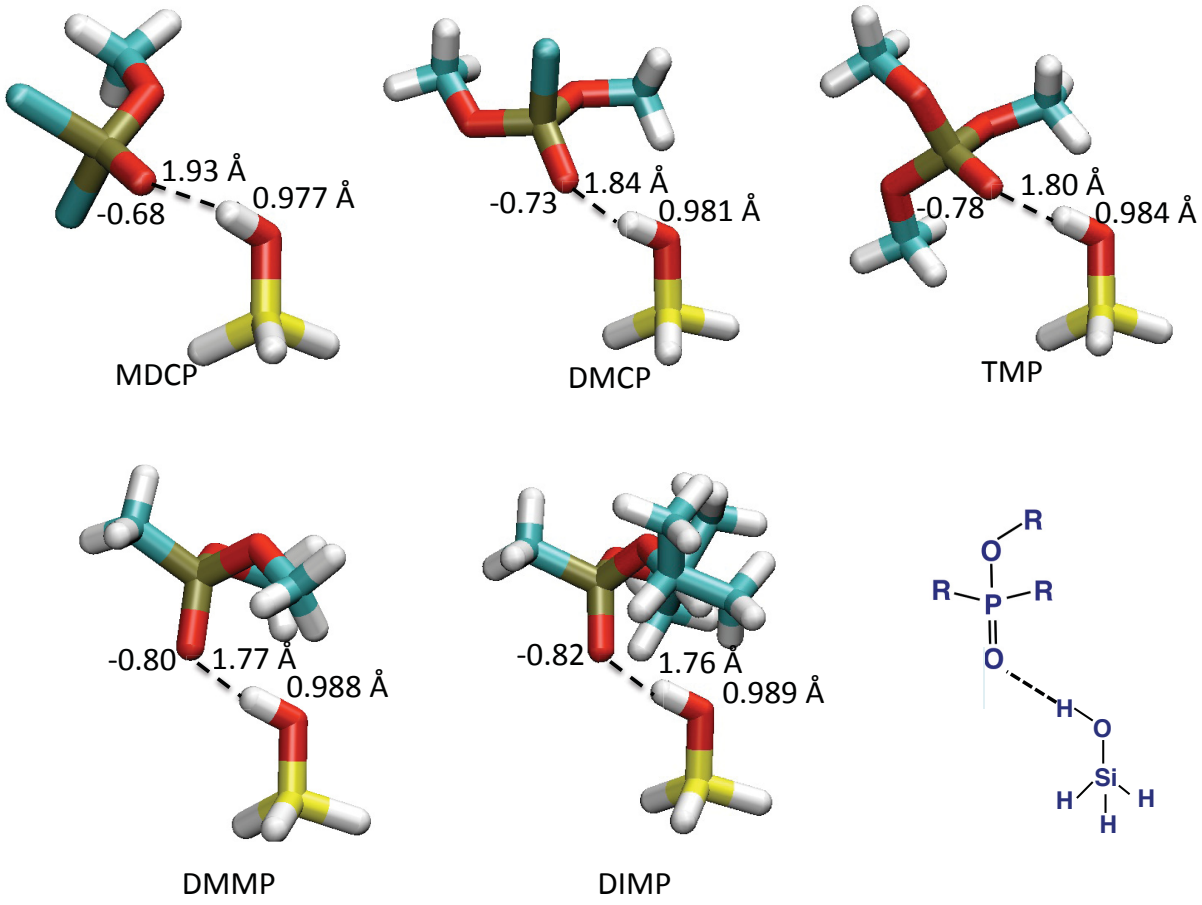

Figure 3.30. Optimized structure of the simulant silanols complex calculated at the MP2/cc-pVTZ//MP2/6-31G* level. Phosphoryl oxygen charge, hydrogen bond distance (~1.8 Å), and SiO-H bond distance (~0.98 Å) are also provided for each complex.

Table 3.6: Calculated and measured properties of simulant-silanol complex. The bond strength is for the hydrogen-bonding interaction between the phosphoryl oxygen and an isolated hydroxyl group of the silica surface. The frequency shift is the red-shift of the SiO-H stretching frequency upon simulant adsorption.

Simulant	Theory		Experimental	
	Bond Strength (kJ/mol)	Δν (OH) (cm^{-1})	Bond Strength (kJ/mol)	Δν (OH) (cm^{-1})
MDCP	25.77	121	43.0	333
DMCP	32.26	206	48.4	427
TMP	36.11	266	52.4	560
DMMP	40.42	348	54.5	596
DIMP	44.89	354	57.9	658

With the help of computation studies, we can see that the magnitude of the partial negative charge of the phosphoryl oxygen atom is key in influencing the strength of hydrogen-bonding. And the other substituents of each simulant all influence the magnitude of that partial negative charge.

3.3.4 Hammett Plot Analysis

Substituents effects on reaction rates and equilibrium constants are often investigated through use of the Hammett equation (Equation 3.10), where k_H and k_X are the reaction rates of an unsubstituted and substituted substrate respectively, ρ is the reaction constant (susceptibility factor), and σ is the empirically derived substituent constant.

$$\log\left(\frac{k_X}{k_H}\right) = \rho\sigma \qquad 3.10$$

Benzoic acid is the standard substrate and its ionization rate is compared to the ionization rate of benzoic acid with substituents at the *meta-* or *para-* position.

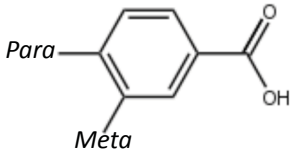

Figure 3.31. Structure of benzoic acid with *para-* and *meta-* positions indicated.

A table of substituent constants is shown in table 3.7. By comparing the constants for substituents at the *meta-* and *para-* positions, the driving force for the interaction can be determined. σ_m constants are caused by inductive effects. σ_p constants are influenced by both inductive and resonance effects. Therefore, resonance effects can be estimated by taking the difference of the σ_p and σ_m.

Table 3.7: Values of Hammett substituent constants.[86]

Substituent	σ_p	σ_m	σ_p-σ_m
CH_3	-0.17	-0.07	-0.10
$OC(CH_3)_2$	-0.45	0.05	-0.50
OCH_3	-0.27	0.12	-0.39
Cl	0.23	0.37	-0.14

Figure 3.32 shows the desorption energies as a function of the sum of the σ values for each simulant. All of the simulants contain the phosphoryl functionality, so σ value plotted is the combination of the other three substituents. For example, in addition to the phosphoryl group, DMMP contains two methoxy groups (2 x 0.12) and one methyl group (-0.07); therefore the Σ σ_m value is 0.17.

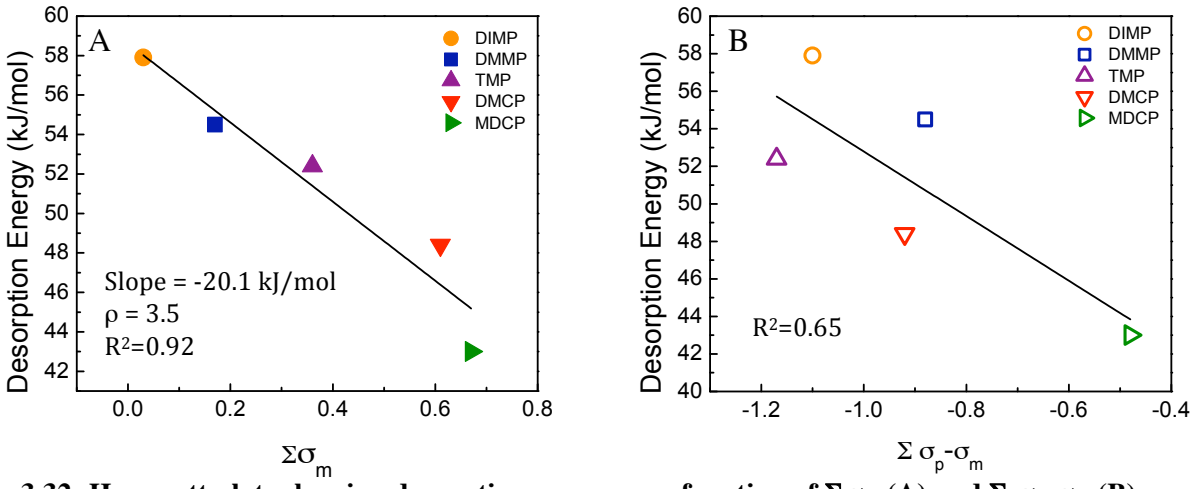

Figure 3.32: Hammett plots showing desorption energy as a function of $\Sigma\sigma_m$ (A) and $\Sigma\ \sigma_p$-σ_m (B).

The Hammett plot using the σ_m values, a measure of inductive effects, shows a linear trend. On the other hand, the Hammett plot demonstrating the resonance effects using σ_p - σ_m, shows a poor linear correlation. This strong degree of linearity using the σ_m constants and the poor correlation using the σ_p - σ_m values suggests that the desorption behavior we observe is dominated by the combined inductive effects of each of the substituents. Therefore, we hypothesize that the inductive effects are responsible for affecting the electron density on the phosphoryl oxygen and furthermore, that these effects ultimately influence the strength of the hydrogen bond formed between the organophosphate and silica surface.

The inductive effects represented by the σ_m constants also represent the electron withdrawing and donating properties of each substituent. More positive σ values correlate to substituents with more strongly electron-withdrawing properties. A methyl and other alkyl groups are weakly electron-donating substituents. Heteroatoms, specifically the oxygens of the methoxy groups, are weakly electron withdrawing. The halogens, often being the most electronegative substituent are commonly the strongest electron- withdrawing substituent.

The magnitude to which the equilibrium is affected by the different substituents is quantified in the slope, ρ, of the Hammett plot. From the slope using the σ_m constants, ρ is equal to 3.5. The positive value for ρ indicates that the hydrogen-bond breaking mechanism is favored by electron-withdrawing substituents. This qualitative trend is supported by the experimental data showing that electron-withdrawing substituents weaken the hydrogen bond, making it easier to break.

Using DMMP as a benchmark, we can systematically see how changing individual functional groups influences the oxygen's atomic charge. Comparing DIMP and DMMP, DIMP has two isopropyl groups in place of two methyl groups. The additional alkyl functionality of

DIMP contributes more electron density to the phosphoryl oxygen, making DIMP the strongest hydrogen bonder of the simulant studied. DMMP and TMP only differ by one substituent; going from DMMP to TMMP, we replace a methyl with a methoxy. TMP, containing the electron withdrawing methoxy group, pulls electron density away from the phosphoryl group making it less effective at hydrogen bonding. Comparing TMP and DMCP, which are just one substituent different, DMCP contains a Cl in place of a methoxy group. The chorine, being strongly electron withdrawing reduces the negative charge of the oxygen. Going from DMCP to MDCP, we replace another methoxy with a chlorine, which further reduces the electron density on the phosphoryl oxygen making it the least effective hydrogen-bonding simulant of the series.

3.3.5 Comparison to Literature

The desorption energies reported in this work are for the adsorption of a series of organophosphates hydrogen bonded to isolated surface silanols and are in the range of 40 to 60 kJ/mol. These values are significantly lower than those previously reported in the literature. Bermudez determined computationally that DMMP hydrogen bonds to amorphous silica with an adsorption strength of 83.7 kJ/mol, nearly 30 kJ/mol higher than the value reported in this work. This difference likely arises from dissimilar degrees of surface hydroxylation. The hydroxylation level of our silica surface was ~2 OH/nm^2, while Bermudez utilized a surface with 4 OH/nm^2. The optimized structures of DMMP adsorbed to silica in his work had two silanols groups participating in hydrogen bonding, which would increase the adsorption strength compared to our studies.

The work of Quenneville *et al*. emphasized that degree of hydroxylation can not only affect adsorption strength, but also the adsorption structure. At high degrees of hydroxylation, the majority of hydrogen bonding occurs between the phosphoryl oxygen and surface silanols.

But as the concentration of hydroxyl groups is decreased, they speculate, that a larger percentage of hydrogen bonding occurs between the methoxy oxygen atoms and surface silanols.

Henderson *et al*. also conducted TPD experiments of DMMP adsorbed to amorphous silica and reported a desorption energy of 70.7 kJ/mol, about 25 kJ/mol higher than measured in the work presented here. Their experimental setup, similar to ours, used a silica sample pressed into a mesh grid. However, in their data analysis, they used the typically assumed prefactor of 10^{13} s^{-1}, which we have shown is not necessarily appropriate, specifically when using samples where readsorption or diffusion effects are important. Diffusion effects have been shown to lower the prefactor of the PW equation, which also leads to a lower calculated desorption energy.

The ultimate goal of much of the simulant research is aimed at developing an understanding of how the live chemical warfare agents interact with different surfaces. We have demonstrated here that the Badger-Bauer relationship applies to organophophate simulants on a surface. Furthermore, we have shown that the strength of the hydrogen-bonding directly depends on the atomic charge of the phosphoryl oxygen. From computational studies, the atomic charge at the phosphoryl oxygen can be calculated and then used to estimate the activation energy for desorption of Sarin from silica. From the linear relationship between computationally determined charge and experimentally measured desorption energy (Figure 3.29), the desorption energy of Sarin is estimated at 53 kJ/mol, based on an atomic charge of -0.60 on the phosphoryl oxygen atom.

3.4 Summary

The goal of this chapter was to investigate the types and strengths of the interactions occurring between organophosphate simulants and a silica surface. We used IR spectroscopy to determine that each of the simulants investigated hydrogen bond to surface silanols through the

simulants' phosphoryl oxygen. TPD experiments were conducted to measure the adsorption strength of each simulant to silica. DIMP, DMMP, TMP, DMCP, and MDCP hydrogen bond to the surface with strengths of 57.9± 1, 54.5 ± 0.3, 52.4 ± 0.6, 48.4 ± 1, and 43.0 ± 0.8 kJ/mol respectively. The magnitude of the OH frequency shift was observed to be linearly related to the adsorption strength where stronger adsorption strengths produced larger frequency shifts as expected with the Badger-Bauer relationship and shown in Figure 3.29.

Computational studies were completed to learn how small structural changes of the different simulants affected their adsorption to silica. These calculations showed that the adsorption strength was directly related to the electron density around the phosphoryl oxygen. Inductive effects relating to the electron donating or withdrawing properties of different substituents are responsible for influencing the oxygen's partial charge, and ultimately a simulant's effectiveness as a hydrogen-bond acceptor. Using the empirical relationships observed for the simulants, the desorption energy for Sarin from silica is estimated to be 53 kJ/mol.

Chapter 4

Adsorption and Desorption of HD Simulants from Amorphous Silica

4.1 Introduction

The fundamental interactions of blister agents, a class of chemical warfare agents, on surfaces needs to be studied to further the development of sorbents, sensors, and effective decontamination strategies. Compared to the nerve agents and simulants discussed in the previous chapters, mustard (HD) is far less studied in the literature. And again, researchers commonly use simulants to infer chemistry about the live agent. The focus of the research presented in this chapter is to describe the fundamental interactions between mustard simulants and amorphous silica.

4.1.1 Silica Surfaces

Silica is a surface that is ubiquitous in our environment. Therefore, understanding how different gases, specifically toxic gases like mustard, interact with this surface is important for learning the environmental fate of these contaminants. Mustard is considered one of the more persistent chemical warfare agents, further emphasizing the need to learn how it interacts with environmentally relevant materials.[5] Additionally, silica, and other hydrogen-bonding surfaces, are being used as sorbents for the development of biosensors and new decontamination strategies.

4.1.2 HD Simulants

Mustard simulants offer an approach to learn about agent chemistry without the need to subject researchers to highly toxic materials. The best simulant would provide the exact same chemical functionality as the agent while exhibiting none of its toxic effects. The simulant 2-chloroethyl ethyl sulfide (2-CEES) has many chemical similarities to the live agent, mustard.

Both compounds have the sulfur and chlorine functionalities separated by a two-carbon chain. The only difference is that the agent has an additional chlorine atom. The similar chemical structures make 2-CEES an ideal simulant from a chemistry perspective; however, 2-CEES is also one of the more toxic simulants used, making it a poor choice for large-scale testing.

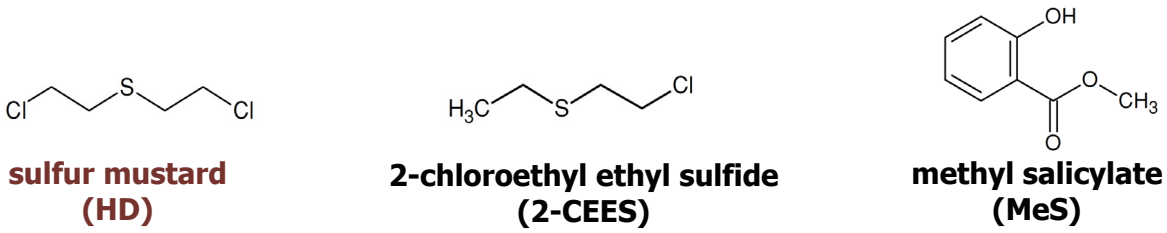

Figure 4.1. Structure of mustard and two common mustard simulants, 2-CEES and MeS, used for this work.

The simulant methyl salicylate (MeS) is a second, possibly surprising, choice for a mustard simulant. Structurally, methyl salicylate and mustard are very different. MeS contains neither the sulfur nor chlorine of mustard. The major functional groups of MeS are the carbonyl, methoxy, hydroxyl, and phenyl groups, none of which are present on the live agent. Despite the different structures, the vapor pressures of mustard and MeS are similar (0.1 and 0.04 torr respectively). The similar vapor pressures make MeS a suitable simulant for studying processes such as the evaporation rate of bulk agent from different materials. Another advantage is that MeS is easily detectable by smell alone. Lastly, MeS, is non-toxic. Also known as wintergreen oil, MeS can be found in many commonly used products including mouthwash, chewing gum, and topical pain ointment.

Key physical properties of the mustard and simulants are provided in the Table 4.1. By examining the physical properties of the two simulants, compared to the live agent mustard, methyl salicylate appears to be more closely related than 2-CEES. However, the data shown

here does not account for key differences in the chemical structure, which are expected to greatly affect the surface chemistry.

Table 4.1: Key physical properties of mustard and two popular mustard simulants, 2-CEES and methyl salicylate.[18]

Molecule	Molecular Weight (g/mol)	Melting Point (°C)	Boiling Point (°C)	Vapor Pressure (torr, 25°C)	Water Solubility (M)	Rate of Hydrolysis (s-1)
HD; mustard; bis(2-chloroethyl) sulfide	159.07	14.45	218	0.11	4.44 x 10-3	0.00129
2-CEES; 2-chloroethyl ethyl sulfide	124.63	-48.6	156.5	3.4	4.85 x 10-2	0.0158
MeS; methyl salicylate	152.15	-8	223	0.04	5.26 x 10 –3	--

4.1.3. HD Simulant Adsorption on Silica

The fundamental interactions of mustard simulants on pure silica have not been previously studied. The majority of fundamental studies of 2-CEES on surfaces utilize modified silica particles aimed at 2-CEES decomposition. Previous work conducted by Panayotov and Yates have focused on the adsorption of 2-CEES on a TiO_2-SiO_2 mixed oxide surface for the potential use as a photocatalyst.[87] Using transmission IR spectroscopy, they observed that 2-CEES adsorbs primarily to the silica surface and forms hydrogen bonds to isolated silanol groups through both the chlorine and sulfur atoms.

Saxena *et al*. have investigated the decomposition reactions of 2-CEES and live mustard using silica nanoparticles impregnated with reactive chemicals, thereby creating a reactive adsorbent.[88] The most promising system that they studied used aerogel silica nanoparticles loaded with trichlorosocyanuric acid (TCCUA). TCCUA has been shown to decompose other CWAs and silica is an effective sorbent for many gases. Using gas chromatography combined

with mass spectrometry, they found that the half-life of mustard was decreased from 1210.0 minutes on the pure silica nanoparticles to only 2.8 minutes with the TCCUA-silica particles. The half-life of the simulant 2-CEES was only decreased from 302 minutes on silica to just 1 minute with the reactive nanoparticles.

The fundamental interactions of another common mustard simulant, MeS, have not been previously studied. Most adsorption studies of MeS have been chromatography studies aimed at separating and identifying essential oils and ointments.[89,90] There are no known reports of the adsorption strength or structure of MeS on surfaces.

While there have not been studies investigating 2-CEES or methyl salicylate on pure silica, the interactions of other small molecules with this material provide insight into these systems. Taylor *et* al. have studied the adsorption of three small molecules, H_2O, NO, and NH_3, with silica using inverse gas chromatography and quantum chemical methods.[60] They observed that the probe molecules bind most strongly to vicinal hydroxyl groups of the silica surface and the binding enthalpy is approximately 1 kcal/mol less for bonds formed with the isolated and geminal silanol groups. The binding enthalpies to isolated silanols groups were reported as -15.55, -13.61, and -4.63 kcal/mol for NH_3, H_2O, and NO respectively. They also calculated the shift of the SiO-H stretching frequency upon adsorption and the data follow the trend that the more strongly adsorbing species induce a greater shift of this stretching mode. These trends are in excellent agreement with our observations with the adsorption of the organophosphates in Chapter 3, and will also be considered for the adsorption of the mustard simulants discussed in this chapter.

4.2. Experimental Details

The experimental approach and instrument setup is described in detail in Chapter 2. Experimental details specific to the studies with mustard simulants are provided here.

4.2.1 Materials

The same silica particles used in the studies with the organophosphates were used for experiments with the mustard simulants. These were Aerosil silica nanoparticles, with a surface area of 200 m^2/g and 12 nm average particle diameter (Spectrum Chemical). We observed that the particles were not altered over time, as identical IR spectra of the silica sample were recorded prior to each experiment. Furthermore, the same desorption energies were measured for old and new silica samples. The simulants 2-CEES (98%) and MeS (99+%), and an analogous molecule methyl 2-methylbenozate (MMB, 99+%), were purchased from Sigma-Aldrich. The simulants were purified via three freeze-pump-thaw cycles prior to use. Liquid nitrogen (LN_2) was obtained from Airgas.

Caution: 2-CEES is highly toxic and special precautions must be taken when handling, storing, and disposing this chemical. Specifically, the 2-CEES sample was prepared in the fume hood and stored in a stainless steel canister sealed with a bellows sealed valve. After experiments, all contaminated lines were heated under vacuum and scrubbed with house nitrogen. Any 2-CEES waste was immediately picked up by Virginia Tech Environmental Health and Safety.

4.2.2 Preparation of Silica Surface

Preparation of the silica sample was previously described in Chapter 3. Briefly, the silica sample was prepared in by pressing approximately 5 mg of silica nanoparticles were pressed into a tungsten mesh grid, clamped between nickel brackets. Immediately prior to each experiment, the sample mesh was resistively heated to 700 K for five minutes to produce a surface hydroxyl

density of about 2 OH/nm^2. The sample was then cooled to 225 K with LN_2. Before simulant exposure, IR reference scans were collected of both a blank spot of the mesh and the silica sample spot.

4.2.3 Surface Exposure

Simulants were stored in stainless steel canisters attached to bellows-sealed valves that were welded to a stainless steel manifold. Immediately prior to dosing, the scroll pump ballast backing the main turbo pump was opened and the stainless steel directional doser with glass capillary array was positioned 3 mm from the center of the silica sample spot.

4.2.4 IR Data Acquisition

Transmission IR spectroscopy was performed with a Nicolet Nexus 670 FTIR spectrometer coupled to the UHV chamber. The light from a SiC globar source was focused at the center of the silica sample, then traveled through an external optics box where the light was focused into a LN_2 cooled mercury telluride cadmium detector. Each spectrum recorded during dosing was the average of 128 scans collected at 4 cm^{-1} resolution, with a 32 mm^2 aperture and 1.89 scanner velocity. During TPD, the spectra were averages of 16 scans and the same previous settings. The spectra presented in this work are shown as difference spectra. For characterization of the silica sample itself, a blank spot on the mesh was used to provide a reference. For surface characterization during dosing, a spectrum of the clean silica sample was used as the background. During TPD studies, the simulant-dosed silica was the reference.

Gas-phase spectra for each of the simulants were collected using a Nicolet Nexus 470 FTIR spectrometer with a home-built high-pressure flow cell. For these measurements, nitrogen was passed through a glass bulb containing ~5 mL of simulant which transported the simulant

vapor into the flow cell. Each spectrum is a compilation of 256 scans collected at 4 cm^{-1} resolution with a 30 mm aperture and 1.89 cm/s scanner velocity.

4.2.5 Mass Spectral Data Acquisition

An axial ionizer mass spectrometer was used to collect all mass spectral data. Data were recorded during simulant dosing to identify major cracks and to confirm the purity of the source. During dosing, mass spectral data were recorded over the mass range 15-160 amu. The filament, multiplier, and dynode were set at 2.0 mA, 1750V, and 4000V respectively. During desorption experiments, mass spectral data were recorded for the five most intense fragments and the multiplier and dynode were increased to 2000V and 5000V, respectively.

4.2.6 Temperature-Programmed Desorption

Temperature-programmed desorption (TPD) experiments were conducted using the coverage dependent approach described in detail in chapter 4. Briefly, all simulants were dosed onto a 225 K silica surface. Following simulant exposure, the surface was annealed to achieve a uniform distribution of simulant. The sample was annealed to 250 K for 2-CEES and 275 K for MeS and MMB.

To begin the TPD with different initial coverages, the sample was annealed for different lengths of time (between 1 second up to 5 minutes). Samples were annealed to both regulate simulant coverage, as well as to ensure a uniform distribution of simulant throughout the particulate silica sample. Immediately following annealing, the sample temperature was dropped to 195 K. At this time, the doser was pulled back as to not obstruct the path between the sample and the mass spectrometer, the sample was realigned to provide the best possible line of sight with the mass spectrometer, and a new silica IR background spectrum was recorded.

The TPD was conducted using a 0.2 K/s ramp controlled with a Honeywell PID and custom power supply. This relatively slow ramp provided sufficient time for molecules to diffuse throughout the silica sample before desorbing. IR and mass spectral data were recorded throughout the temperature ramp until the surface temperature reached 450 K. After the adsorbates had desorbed from the surface, the mass spectrometer settings were reduced to standby conditions, the sample was returned to room temperature, and the LN_2 reservoir was purged with house nitrogen to keep the UHV ceramic seals dry.

4.3. Results and Discussion

As described in chapter 3, IR spectroscopy and TPD studies have shown to be powerful tools in gaining insight into the fundamental adsorption and desorption energies of CWA simulants from silica. The same approach was taken here to investigate mustard simulants.

4.3.1. 2-CEES Adsorption

4.3.1.1 IR Analysis

IR spectra of the cooled silica sample (225 K) were recorded during 2-CEES dosing. Figure 4.2 shows the IR difference spectrum of the silica sample after 15 minutes of 2-CEES dosing. The gas-phase spectrum of 2-CEES is also provided for reference. From the IR data, it is clear that 2-CEES adsorbs to the surface, as evidenced by the development of characteristic vibrational modes of 2-CEES. The C-H stretches of the molecule appear at 2976, 2937, and 2880 cm^{-1} and are unshifted from their gas-phase positions. No 2-CEES peaks are observed if a spectrum is taken of an empty spot on the mesh grid, away from the silica sample, so we can be confident that these peaks are due to adsorbates and not the gas-phase species. Many of the deformation modes that are present in the gas-phase spectrum, are not observed on the silica sample because the silica sample itself absorbs very strongly between 1300-1000 cm^{-1}.

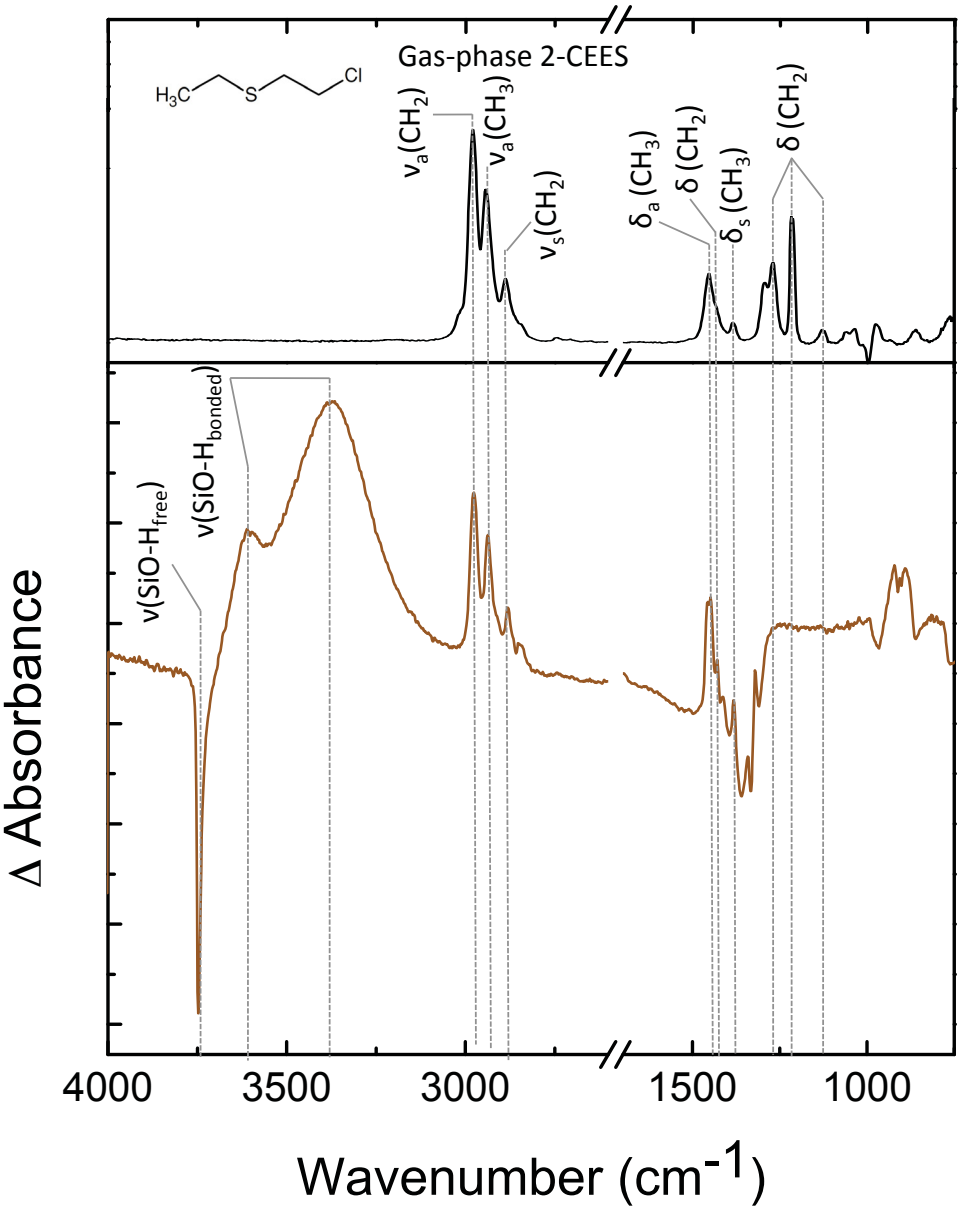

Figure 4.2: IR difference spectrum of 2-CEES adsorbed to a 225 K silica sample after 15 minutes of dosing. The reference spectrum is of the silica sample prior to simulant exposure.

The IR data also provide information about how the silica changes upon 2-CEES adsorption. The sharp, negative peak at 3748 cm^{-1} indicates, that upon adsorption, free hydroxyl groups are consumed. The free hydroxyl groups are converted into two distinct hydrogen-bonded species, as evidenced by the simultaneous growth of two positive broad peaks at 3366

and 3611 cm^{-1}, which suggests that the adsorbates interact with the surface through the formation of two types of hydrogen bonds. We can hypothesize that these interactions are due to the adsorption through both the Cl and S functionalities, which have been observed previously for similar systems.[87] In assigning the two hydrogen-bonding modes, it is predicted that the adsorption via the Cl moiety is the weaker interaction and would therefore be the mode observed at higher wavenumbers. This prediction is based upon the organophosphate work, which showed a surprisingly small negative charge on the halogen atom, which would corresponds to relatively weak hydrogen-bond formation. The electronic character of the C and S atoms can also affect the observed shifts. Hertl and Hair have reported that small shifts are typical when p-orbital electrons participates in hydrogen bonding, and large shifts are observed when hybrid orbital electrons participate in hydrogen bonding.[91] Because the S-C bond has more hybrid character, it may be expected that it would be the mode more strongly shifted.

Work by Panayotov and Yates supports our hypothesis that the IR modes at 3611 cm^{-1} and 3366 cm^{-1} are assigned to the hydrogen bonding via the chlorine and sulfur moieties respectively. They recorded IR spectra of diethyl sulfide and ethyl chloride adsorbed on a sample of mixed titania and silica nanoparticles as shown in Figure 4.3.[87] Adsorption of diethyl sulfide to surface silanol groups shows the growth of a broad peak at 3280 cm^{-1}, which is assigned to the species that forms a hydrogen bond with the sulfur moiety. Adsorption of ethyl chloride to surface silanol groups shows a peak at 3620 cm^{-1}, and is assigned to the formation of a hydrogen bond between hydroxyl groups and the chorine moiety.

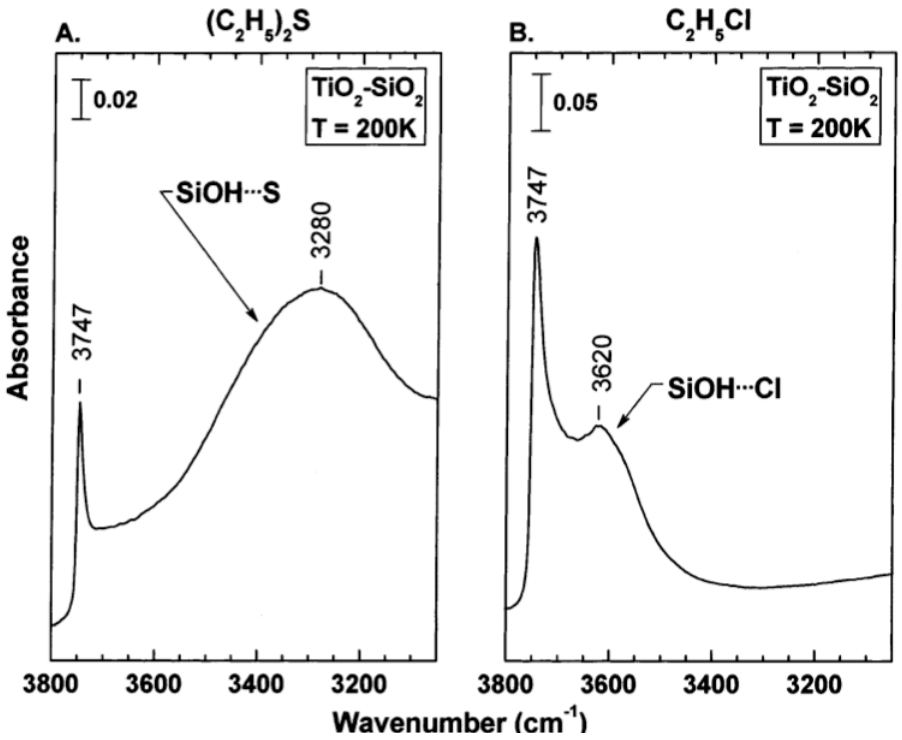

Figure 4.3: IR spectra of the OH groups hydrogen-bonded to S and Cl moieties in diethyl sulfide and ethyl chloride adsorbed on TiO_2-SiO_2.[87] Reprinted with permission from D. Panayotov and J.T. Yates, Jr. *J. Phys. Chem. B*. 2003, *107*, 10560-10564. Copyright 2003 American Chemical Society.

Table 4.2. Mode assignments for 2-CEES in the gas phase and adsorbed on silica.

Mode	2-CEES$_{(g)}$[92,93]	2-CEES$_{(ads)}$
$Si(O-H)_{free}$	--	3748
$Si(O-H)_{bonded-Cl}$	--	3611
$Si(O-H)_{bonded-S}$	--	3366
$\nu_a(CH_2)$	2978	2976
$\nu_s(CH_2)$	2943	2937
$\nu_s(CH_3)$	2888	2880
$\delta_a(CH_3)_{bend}$	1453	1457
$\delta(CH_2)_{scissor}$	1430	1430
$\delta_s(CH_3)_{bend}$	1385	1382
$\delta(CH_2)_{wag}$	1293	*
$\delta(CH_2)_{twist}$	1270	*
$\delta(CH_2)_{wag}$	1217	*
$\delta(CH_2)_{twist}$	1129	*

Comparing the shifts of the ν(OH) mode of these molecules with similar chemical functionalities adsorbed on silica, we hypothesize the IR peaks of 2-CEES adsorbed on silica at 3611 and 3366 cm^{-1} to represent hydrogen bonds involving the chlorine and sulfur moieties, respectively. Table 4.2 provides peak assignments for 2-CEES in the gas phase and adsorbed to silica.

In chapter 3, which describes the adsorption of organophosphates to silica, the magnitude of the shift of the ν(OH) mode was linearly related to the adsorption strength. However, this linear relationship often fails when comparing molecules of significantly different electronic structures.[64,87,91] To estimate the specific contributions to adsorption of the Cl and S individually, TPD experiments could be conducted with diethyl sulfide and ethyl chloride

From the IR spectra, (Figure 4.2), multiple structures of the simulant adsorbed to silica can be proposed. The vibrational modes of the C-S and C-Cl bonds are not within the range of our detector, but the minimal shifts of the observable modes of 2-CEES in the gas phase compared to the adsorbed state suggests that 2-CEES adsorbs molecularly through the formation of hydrogen bonds between surface hydroxyl groups and the 2-CEES molecule. That is, no

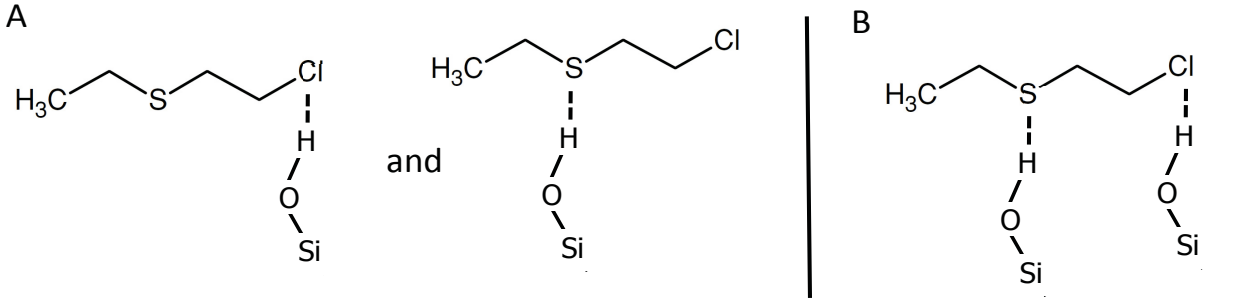

Figure 4.4: Adsorption schematics of 2-CEES to silica. (A) Adsorption of 2-CEES to a free hydroxyl groups through the Cl or S atoms. (B) Adsorption of 2-CEES to free hydroxyl groups through both the Cl and S atoms.

bonds are broken during adsorption, as expected for this relatively inert surface. The two distinct shifts of the ν(OH) mode are consistent with the bifunctional bonding capability of 2-CEES and that hydrogen bonds are likely formed with both the S and Cl moieties of the simulant. However, it is not immediately apparent whether each 2-CEES molecule adsorbs to silica through both the S and Cl atoms (Figure 4.4 B) or if there is a combination of 2-CEES adsorbed through either the S or Cl moieties (Figure 4.4 A).

To help determine if the structure of the 2-CEES adsorbed is hydrogen bonded via one or both of the key functionalities, simulant coverage is considered. It is expected that if each 2-CEES molecule only forms one hydrogen bond to the surface, the concentration of surface silanols should not affect the maximum coverage possible. However, upon exposure of the 225 K silica sample to 2-CEES, the maximum coverage achieved was 0.25 ML, meaning that only 25% of the free hydroxyls were consumed as evidenced by the IR spectra provided in Figure 4.5.

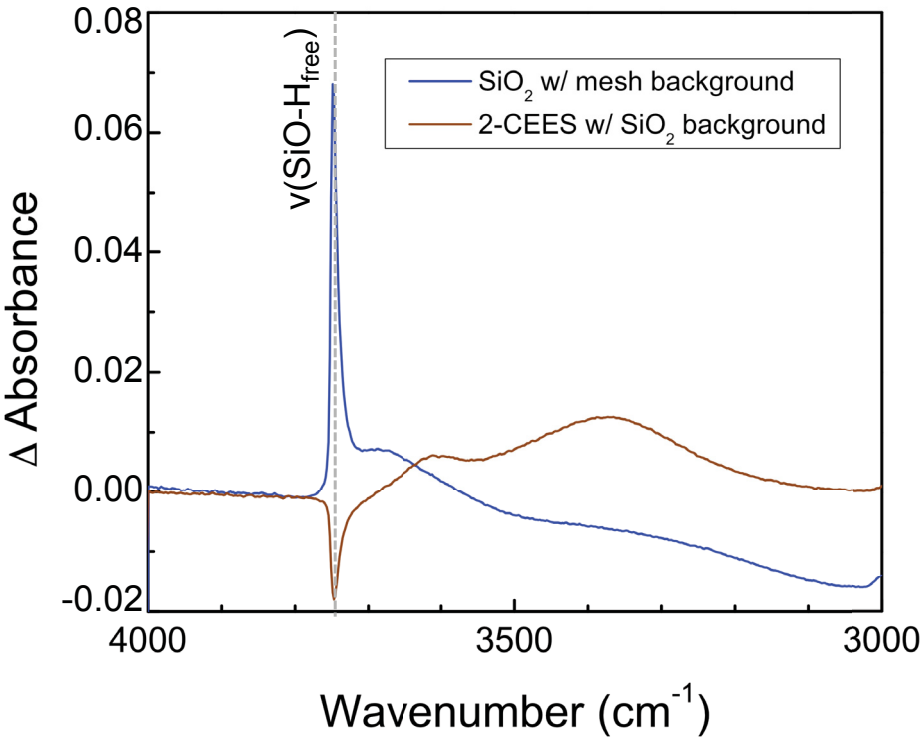

Figure 4.5 IR spectra of the clean silica sample (blue), having a large positive peak for the free OH groups and the silica sample after 2-CEES adsorption (brown), showing minor consumption of the free OH groups.

The low coverage likely arises because only a fraction of the free hydroxyl groups are spaced appropriately so that one hydroxyl group can hydrogen bond to the S, and a second hydroxyl group can hydrogen bond to the Cl. That is, for a hydroxylation level of 2.0 OH/nm^2, the average linear spacing between OH groups is 0.74 nm, compared to the sulfur-chlorine distance of 2-CEES of 0.30 nm. Because, even at extensive dosing times, only a fraction of

hydroxyls are consumed, the structure shown in Figure 4.4B, which shows two hydrogen bonds for each 2-CEES adsorbate, is the more probable structure.

Additional evidence for the structure of adsorbed 2-CEES as shown in Figure 4.4B is provided by the IR spectra recorded during the desorption portion of the experiment. Figure 4.6 shows selected spectra in the high wavenumber region collected during TPD. The background spectrum is the 2-CEES dosed silica sample. During desorption, the peak for the free Si-OH groups becomes positive, indicating that these species are regenerated upon heating. Both of the peaks for hydrogen bonded OH groups become increasingly negative, as the hydrogen bonds between the adsorbate and surface are broken. The signature 2-CEES peak, the $\nu_a(CH_2)$ mode also decreases as 2-CEES desorbs from the surface.

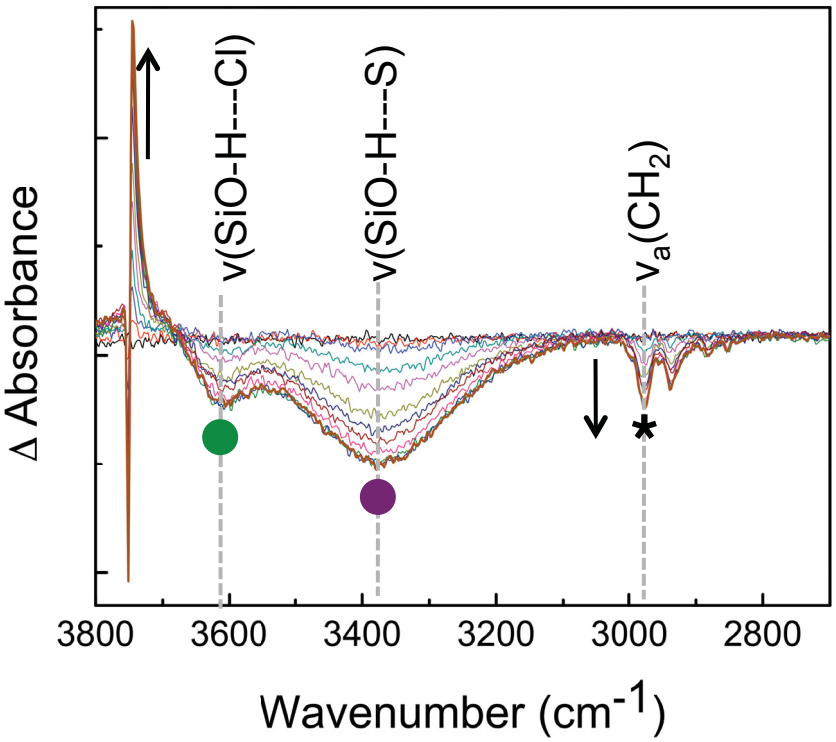

Figure 4.6: IR spectra of 2-CEES dosed sample during TPD. The final spectrum taken during the heating is offset for clarity.

Comparing the rates at which the key spectral features change over time provides information about how each of the hydrogen-bonded modes (via the S and Cl) change as the 2-CEES desorbs from the surface. Figure 4.7 shows the change in absorbance of the SiOH--S, SiOH--Cl, and CH_2 stretching modes as a function of time. The simultaneous decrease of all of these modes suggests that both types of hydrogen bonds are broken at the same time. Given that the interaction of 2-CEES via the sulfur is twice as strong as through the chlorine as provided by calculations, it is expected that both bonds would only break simultaneously if each 2-CEES adsorbate forms two hydrogen bonds with the surface.

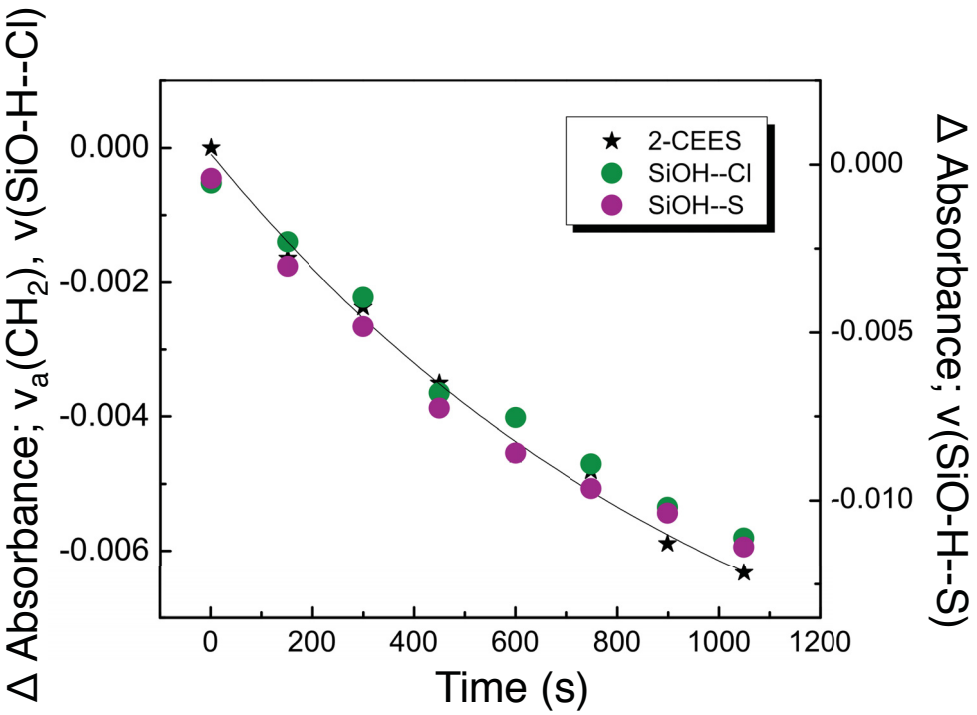

Figure 4.7: Change in absorbance of the SiOH--S, SiOH--Cl, and CH_2 stretching modes as a function time during TPD.

4.3.1.2 Temperature-Programmed Desorption: Inversion Analysis

TPD experiments were conducted to quantitatively measure the simulants' activation energy for desorption from silica. In the case of 2-CEES, this energy correlates to the combined breaking of the hydrogen bonds formed via both the S and Cl moieties. Figure 4.8 shows the full mass spectrum for 2-CEES. The spectra recorded during dosing and during desorption showed identical cracking patterns and ratios, indicating minimal decomposition occurred on the surface. All of the major simulant cracks showed the same behavior; however, only the most intense fragment was used in the data analysis.

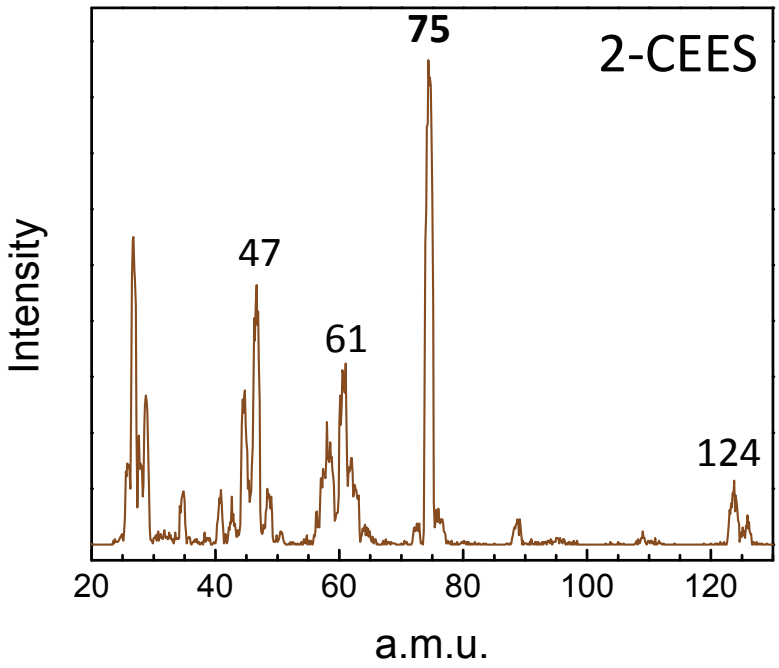

Figure 4.8: Mass spectrum of 2-CEES during dosing. The most intense fragment for each was used in data analysis.

The inversion analysis approach was taken to determine the desorption energy of the simulants from silica as described in detail in chapter 3 (3.3.2.2). Briefly, the desorption rate is described by the Polanyi-Wigner (PW) equation (equation 4.1), where Θ is coverage, t is time, T

4.1

is temperature, ν is the prefactor, E_d is desorption energy, R is the gas constant, and n is desorption order (n=1 for the first-order desorption of simulant from silica).

$$r = -\frac{d\Theta}{dt} = \nu_n(\Theta) \cdot \exp(-\frac{\Delta E_d(\Theta)}{RT}) \cdot \Theta^n \qquad 4.1$$

Rearrangement of the PW equation results in equation 4.2 which provides the desorption energy as a function of coverage. Numerical integration of this curve can then provide a simulated set of

$$E_d(\Theta) = -k_B T \ln\left(-\frac{d\Theta/dt}{\nu\Theta}\right) \qquad 4.2$$

desorption spectra for lower initial adsorbate coverages. The prefactor is then treated as a variational parameter to provide minimal error between the experimental and simulated TPD spectra. Final agreement of the experimental and simulated spectra confirms applicability of the PW equation which then provides the desorption energy.

The experimental and simulated TPD spectra for 2-CEES are shown in Figure 4.9. Each spectrum was collected beginning with a different initial simulant coverage and the integral of each spectrum is proportional to that initial coverage. A saturated surface, Θ = 1 ML, corresponds to the consumption of every free OH group on the surface. As the initial coverage was lowered, the peak area decreased. Also, as the initial coverages were lowered, the maximum desorption rate temperature shifts to higher temperatures. This shift to higher temperatures is consistent with a surface containing a distribution of adsorption sites. The alignment of the high temperature tails indicates that the adsorbates are mobile enough on the surface to locate the strongest adsorption sites.

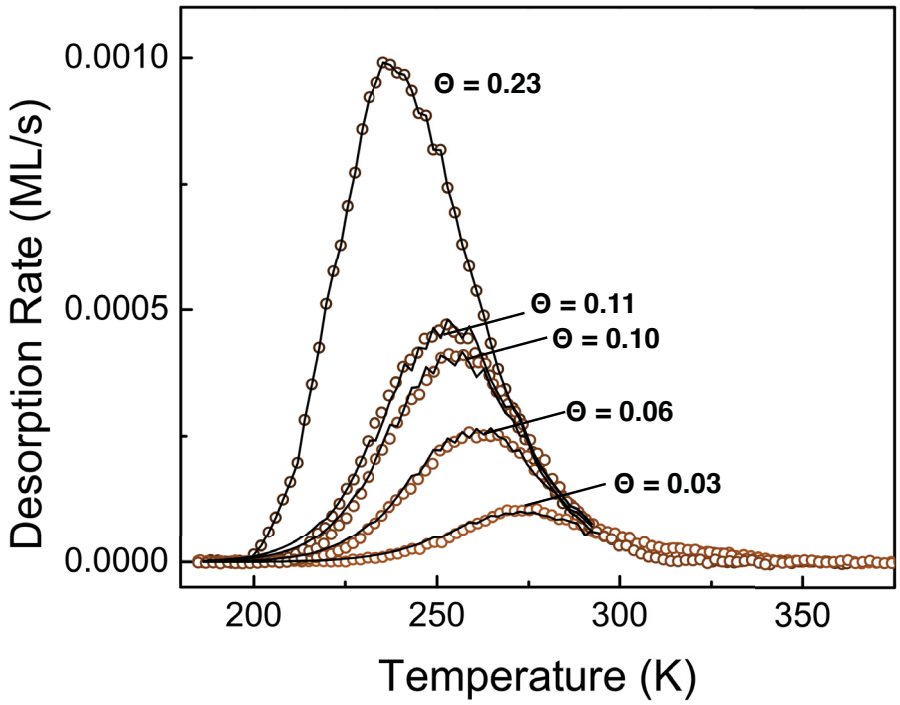

Figure 4.9: Experimental (open circles) and simulated (line) TPD spectra of 2-CEES (ν=1 x 10^7 s^{-1}).

The accurate treatment of the prefactor is essential for determining the value for the desorption energy. The appropriate prefactor for each simulant was determined by minimizing the sum-of-squares of the residuals between the simulated TPD and the experimental data. For 2-CEES, it was determined that $\nu = 1 \times 10^{7\pm0.2} s^{-1}$ provides the best agreement between the simulated and experimental TPD data. This prefactor is significantly smaller than the typically assumed prefactor of 10^{13} s^{-1}, which is on the order of molecular vibrations, and likely reflects that the molecules desorb and readsorb to another particles before reaching the outermost layer of particles and entering the vacuum.[83-85,94-96] However, despite readsorption effects, accurate measurements of the binding strength can be obtained from TPD experiments.[83-85,94,96]

Using the rearranged PW equation, desorption energy as a function of coverage can be plotted. Figure 4.10 shows the E_d curve for 2-CEES adsorbed to silica and shows a broad range of desorption energies, which demonstrates that there is a variety of adsorption sites. This strong

coverage dependence is also consistent with the bifunctional hydrogen boding of 2-CEES to isolated silanol groups. At the highest coverages obtainable, the desorption energy of 2-CEES from silica is about 37 kJ/mol, and at the lowest coverages the desorption energy approaches 44 kJ/mol.

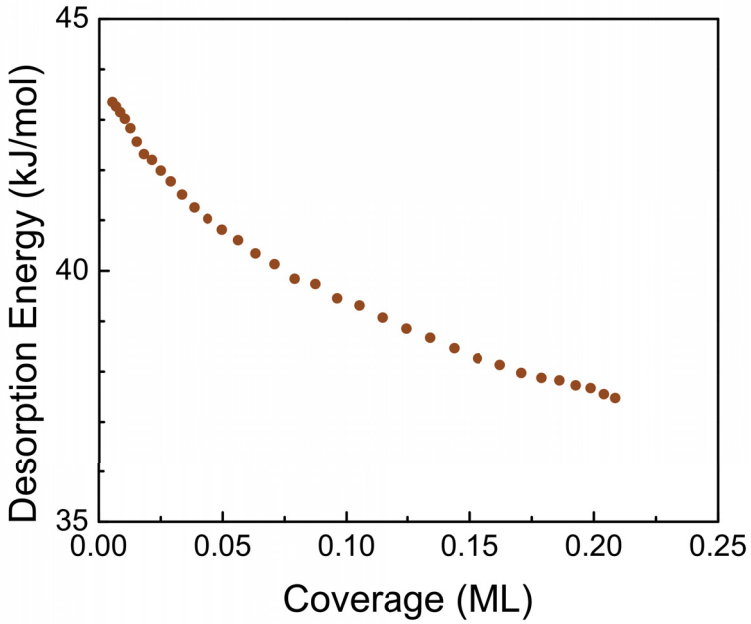

Figure 4.10: Desorption energy as a function of coverage for 2-CEES (v=1 x $10^7 s^{-1}$).

Evaluating 2-CEES as an appropriate simulant for mustard is quite difficult after observing the strong dependence on surface hydroxylation. Given a highly hydroxylated surface, live mustard is expected to adsorb even more strongly than 2-CEES because it has an additional chlorine atom. However, given a surface of equal or lower hydroxyl concentration than that studied here, it is predicted that mustard would adsorb less strongly than 2-CEES. The additional chlorine atom likely pulls electron density away from the other hydrogen bonding moieties, as was observed for the organophosphate simulant series.

4.3.2 MeS Adsorption: IR Analysis

Next, we chose to investigate the adsorption properties of another popular mustard simulant, MeS. IR spectra of the cooled silica sample (225 K) were recorded during initial MeS exposure. Figure 4.11 shows the IR difference spectrum after 15 minutes of MeS dosing.

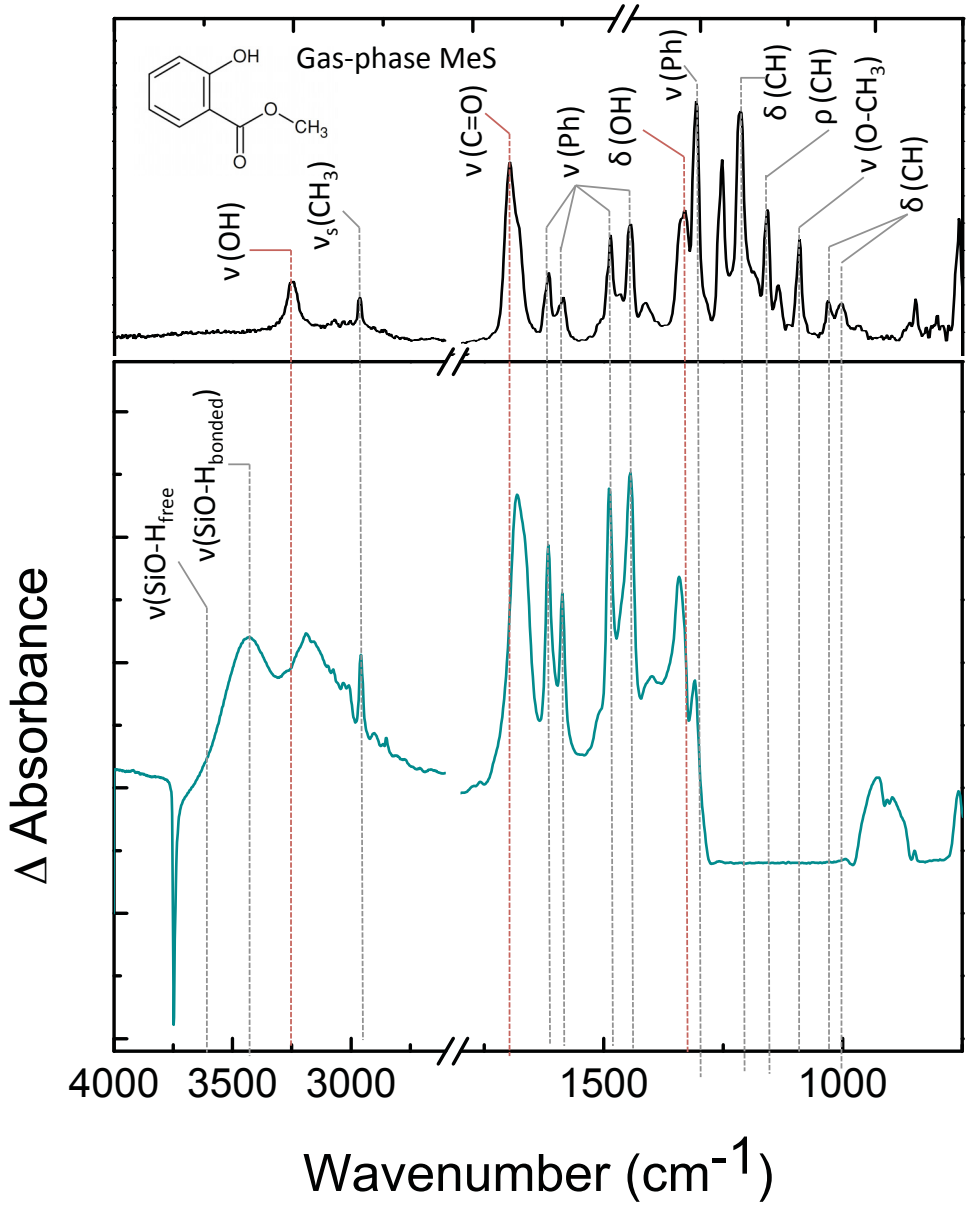

Figure 4.11: IR difference spectrum of MeS adsorbed to a 225 K silica sample after 15 minutes of dosing. The reference spectrum is of the silica sample prior to simulant exposure.

The gas-phase spectrum of MeS is also provided for reference. The conversion of the free OH groups of the silica surface observed at 3748 cm^{-1} to a single surface hydrogen-bonded species at 3431 cm^{-1} is observed, suggesting that MeS forms a single type of bond with the free OH groups of the silica surface. The other broad peak in this region, is hypothesized to be the OH stretching mode of the methyl salicylate. Comparing the frequency of this OH stretching mode to that of the same mode in phenol (3345 cm^{-1}), that for MeS is significantly red-shifted. This shift to lower wavenumbers, is consistant for an intramolecular hydrogen bond possible for MeS in the gas phase. This *cis* conformer, where intermolecular hydrogen bond between the OH and carbonyl groups has been reported as the more stable conformer.[98]

The mode assignments for MeS in the gas phase and adsorbed to silica are shown in Table 4.3. Many of the characteristic MeS modes observed in the gas phase are observed on the simulant dosed silica sample. However, some of the peaks of key MeS modes shift upon adsorption. The ν(OH) mode broadens and red-shifts by about 50 cm^{-1} upon adsorption to silica. The δ(OH) mode is blue-shifted by about 10 cm^{-1}. The ν(C=O) mode also red-shifts, by about 20 cm^{-1}. The stretching modes of the phenyl ring appear in the same position in the gas phase between 1616 and 1445 cm^{-1}. However, in the case of benzene and other aromatics, these modes are

Table 4.3. Mode assignments for MeS in the gas phase and adsorbed on silica.

Mode	$MeS_{(g)}$ [97]	$MeS_{(ads)}$
$Si(O-H)_{free}$	--	3748
$Si(O-H)_{bonded}$	--	3431
ν(OH)	3244	3188
$\nu_a(CH_3)$	2964	2959
ν(C=O)	1698	1681
ν(Ph)	1616	1616
ν(Ph)	1586	1587
ν(Ph)	1487	1488
ν(Ph)	1445	1445
δ(OH)	1331	1342
ν(Ph)	1307	1310
ν(C(=O)-O)	1254	-
δ(CH)	1215	-
ρ(CH)	1159	-
δ(CH)	1136	-
$\nu(O-CH_3)$	1091	-
δ(CH)	1032	-
δ(CH)	1004	-
δ(Ph)	848	

not sensitive to adsorption.[64]

IR spectra recorded during desorption, indicate that MeS desorbs molecularly as no modes for potential decomposition products are observed. Figure 4.12 shows selected spectra of the MeS dosed sample throughout the TPD experiment. Throughout the TPD, the free hydroxyl groups of silica are regenerated as MeS desorbs. The key peaks of MeS become negative as MeS leaves the surface.

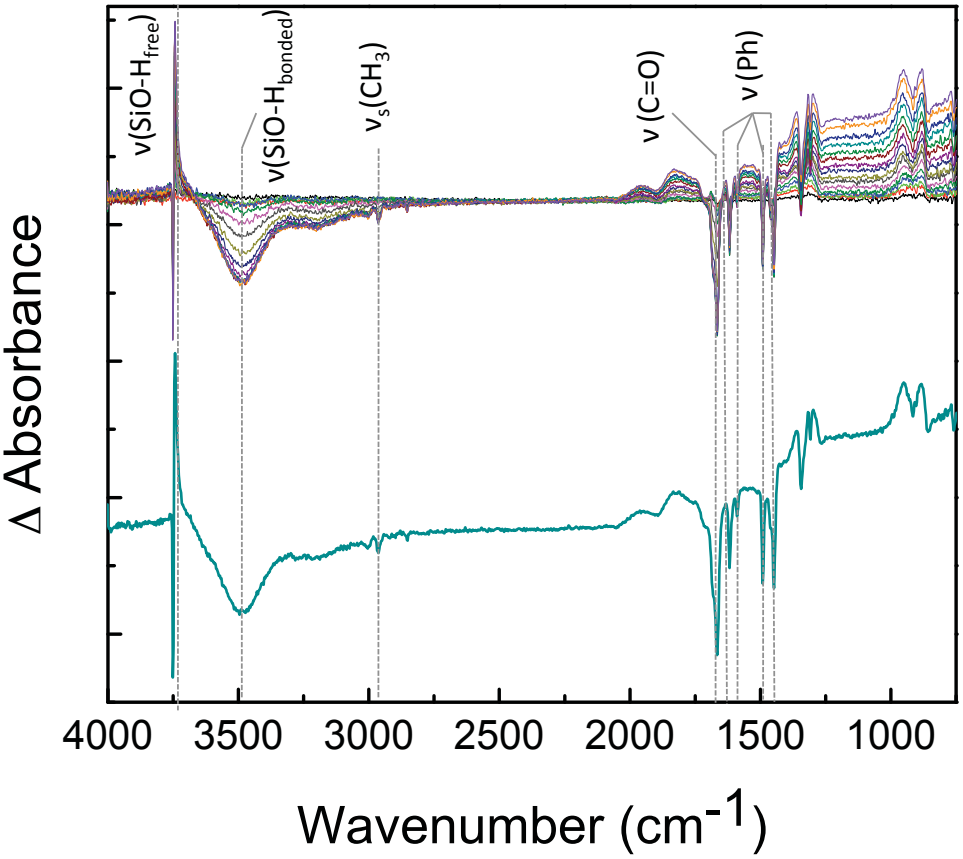

Figure 4.12: IR spectra of MeS dosed sample during TPD. The final spectrum taken during the heating is offset for clarity.

From the IR data alone, the structure of the adsorbed methyl salicylate is not readily apparent. There are four possible types of interaction that could drive adsorption. As shown in Figure 4.13, adsorption may occur via the carbonyl, hydroxyl, or methoxyl oxygens, or through the phenyl ring. Evaluating the probability of adsorption via the carbonyl or methoxyl oxygens,

we refer back to experiments conducted with organophosphates. When the phosphoryl oxygen and methoxyl oxygens were both present, adsorption always occurred through the phosphoryl oxygen. Therefore, we predict that the methoxyl oxygen does not drive the adsorption process. Additionally, the C-H stretches associated with the methoxy group are not shifted upon adsorption, further supporting this hypothesis.

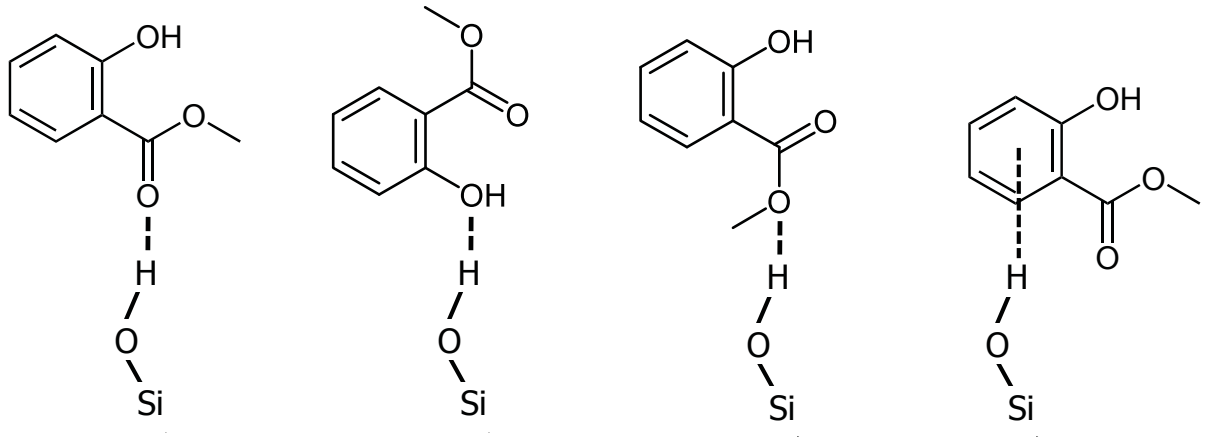

Figure 4.13: Four possible structures for MeS adsorbed to isolated silanol groups. Adsorption may occur via the carbonyl, hydroxyl, methoxyl, or phenyl functionalities.

The phenyl ring of MeS is another functionality that may be important for its interaction with the silica surface, as some of the IR modes associated to the aromatic are shifted upon adsorption. The adsorption of aromatic molecules, including anisole, aniline, styrene, and other halogenobenzenes and methylbenzenes onto silica has been previously studied.[99] Two different structures of the adsorbate were observed depending on the substituents on the aromatic. For the substituents H, CH_3, $CH{=}CH_2$, Cl, Br, and I, the primary interaction with the silica surface was through the π electrons of the phenyl ring. In the case when the substituents contained O and N atoms, adsorption was driven by the formation of a hydrogen bond with these heteroatoms.

A separate experiment investigating the adsorption and reaction of acetophenone on a Pd/SiO_2 surface, reports the adsorption mechanism of the molecule to both the SiO_2 and Pd regions of the surface.[100] While decomposition occurs on the Pd, acetophenone adsorbs molecularly to the inert silica via the carbonyl oxygen. Based on both of these studies, it is expected that the dominating interaction of MeS with silica is not through the phenyl group. The two remaining adsorbate structures are that with MeS forming a hydrogen bond via the carbonyl or hydroxyl oxygen. Thus far, either structure is consistent with our IR data, as modes associated with both of the functionalities shift upon adsorption to silica.

Figure 4.14: Chemical structure of acetophenone.

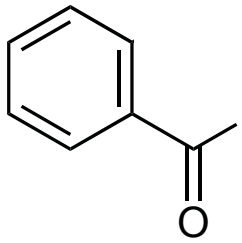

4.3.3 Methyl 2-Methyl Benzoate: IR Analysis

To help learn which structural components of MeS are key to its adsorption on silica, identical experiments were performed with methyl 2-methyl benzoate (MMB). The only structural difference between MeS and MMB is that MMB has a methyl group in place of the hydroxyl group. By changing this single substituent, it is possible to learn how important the OH group is to the adsorption of MeS to silica.

IR spectra of the cooled silica sample were recorded during initial MMB dosing. Figure 4.15 shows the IR difference spectrum of the silica sample after 15 minutes of MMB dosing. The gas-phase spectrum of MMB is also provided for reference. From the IR data, it is clear that MMB adsorbs to the surface as evidenced by the development of characteristic vibrational modes of MMB that grow in intensity during sample exposure. The C-H stretches appear at 3078, 3033, and 2961 cm^{-1}. The stretching modes of the phenyl ring also appear at the same frequencies as they did in the gas phase. The ν(C=O) mode of MMB red-shifts by about 20 cm^{-1}

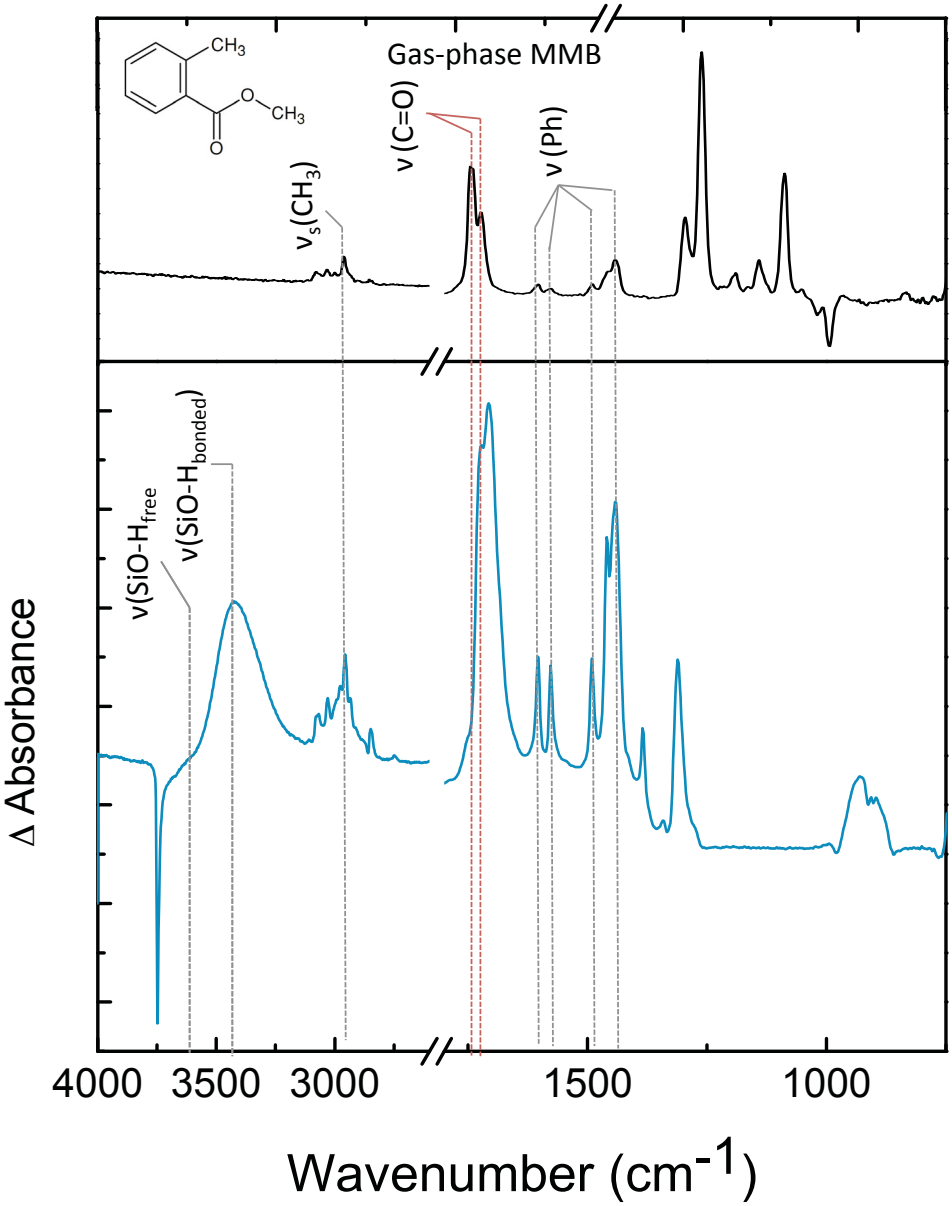

Figure 4.15: IR difference spectrum of MMB adsorbed to a 225 K silica sample after 15 minutes of dosing. The reference spectrum is of the silica sample prior to simulant exposure.

upon adsorption, as was observed in the adsorption of MeS. Other modes appear at 1384, 1342, and 1311 cm^{-1} that are not observed in the gas phase. These are likely also modes associated with the phenyl ring that have significantly shifted from the gas-phase location, which may be caused by the electrostatic interactions of the ring itself with surface silanol groups.[101]

The free OH groups are converted into a single hydrogen bonded species as evidenced by the single broad peak formed at 3425 cm^{-1}. This frequency shift is identical to that observed for MeS (3431 cm^{-1}). If the hydrogen bonding occurs through the same functionality for both MeS and MMB, the strength of the interaction is expected to be very similar, based on the nearly identical shift of the ν(OH) mode.

Table 4.4. Mode assignments for MMB in the gas-phase and adsorbed silica.

Mode	$MMB_{(g)}$	$MMB_{(ads)}$
$Si(O-H)_{free}$	--	3748
$Si(O-H)_{bonded}$	--	3425
$\nu(CH_3)$	3078	3068
$\nu(CH_3)$	3033	3030
$\nu(CH_3)$	2961	2956
$\nu(C=O)_{trans}$	1745	1722
$\nu(C=O)_{cis}$	1723	1707
ν(Ph)	1603	1604
ν(Ph)	1576	1577
ν(Ph)	1490	1491
ν(Ph)	1443	1442
Ph	1296	1384
Ph	1261	1342
Ph	1190	1311

IR spectra were also recorded during the TPD experiments and selected spectra are shown in Figure 4.16. Upon heating, the free hydroxyl groups are regenerated as MMB desorbs. All of the signature modes of MMB remain in the same place as observed in initial MMB adsorption, suggesting that no decomposition occurs during heating.

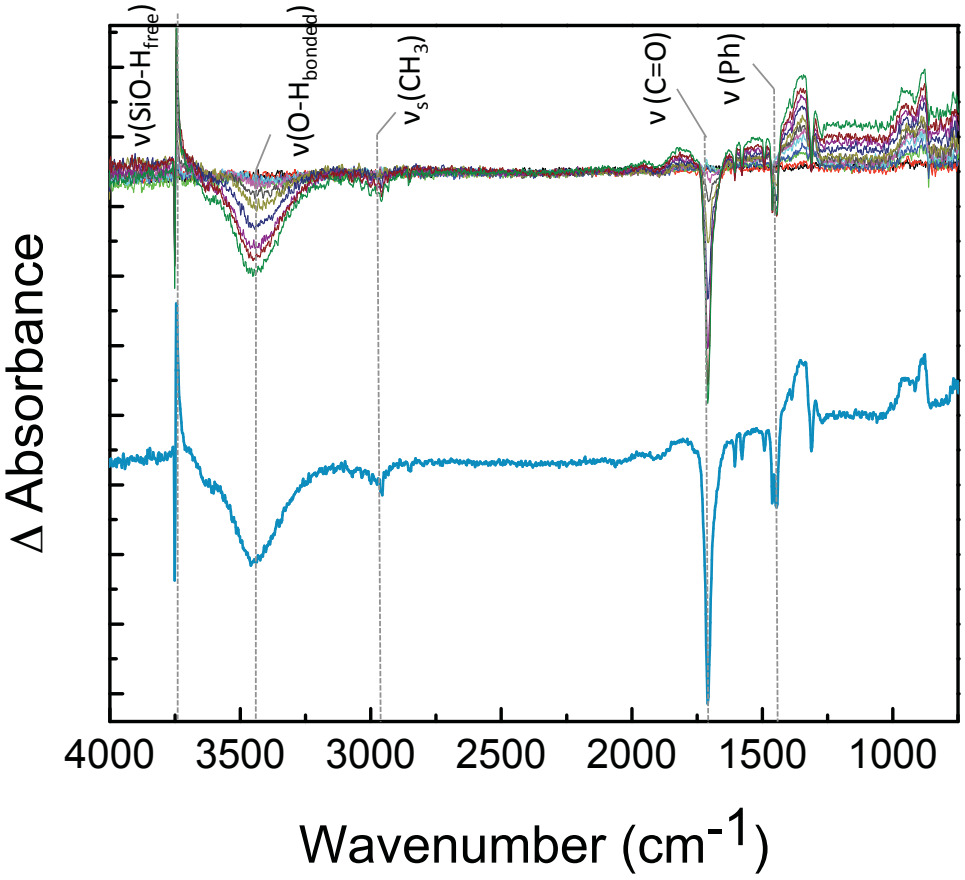

Figure 4.16: IR spectra of MMB dosed sample during TPD. The final spectrum taken during the heating is offset for clarity.

4.3.4 Temperature-Programmed Desorption: Inversion Analysis

TPD experiments were conducted to quantitatively measure the simulants' activation energy for desorption from silica. For all of the TPD experiments, the mass spectrometer was used to measure the simulant desorption rate. Figure 4.17 shows the mass spectra for MeS and MMB. All major cracks were observed in the same ration during sample exposure and TPD, suggesting that both simulants desorb molecularly. While all cracks showed he same behavior, only the most intense fragment was used in the data analysis.

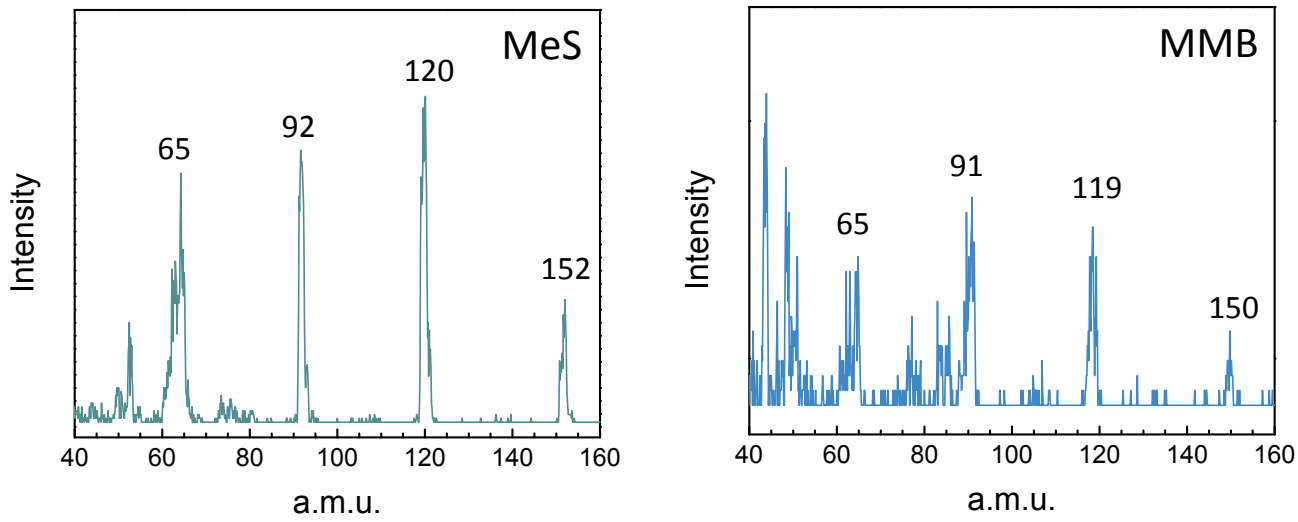

Figure 4.17: Mass spectra of MeS and MMB during dosing. The most intense fragment for each simulant was used in data analysis.

The same type of inversion analysis was conducted for MeS and MMB that was previously described for 2-CEES. The experimental TPD data and simulated fits are shown below using a prefactor of 2 x 10^6 s^{-1}.

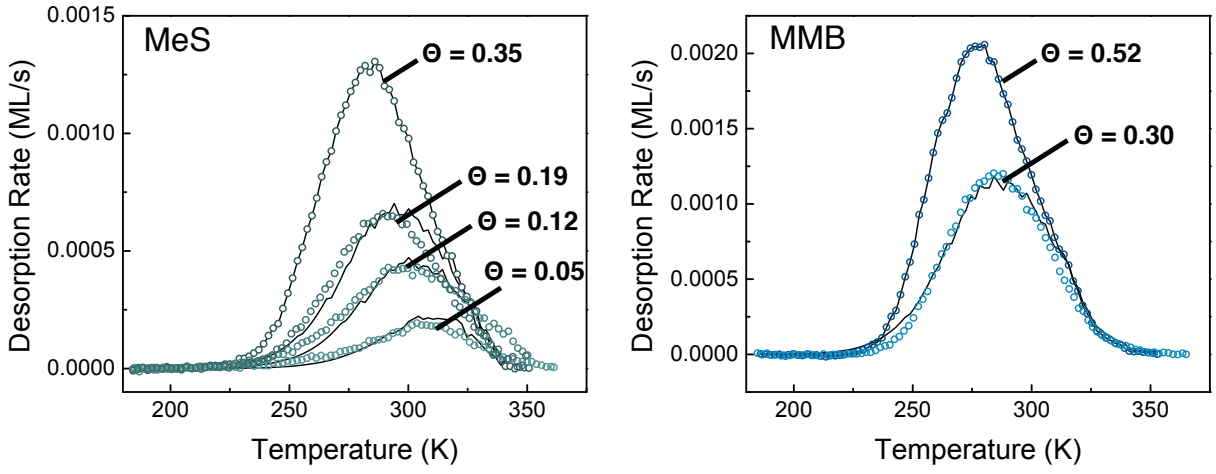

Figure 4.18: Experimental (open circles) and simulated (line) TPD spectra of MeS (left) and MMB (right);(ν=2 x 10^6 s^{-1}).

Using the rearranged PW equation, desorption energy as a function of coverage can be plotted for all of the simulants studied. Figure 4.19 shows the E_d curves for each simulant. For each simulant, there is a broad range of desorption energies, which demonstrates that there is a variety of adsorption sites. However, this dependence is much less pronounced for MeS, MMB, which would be expected for adsorption through a single functionality. The E_d curves for MeS and MMB are nearly identical and are both higher than

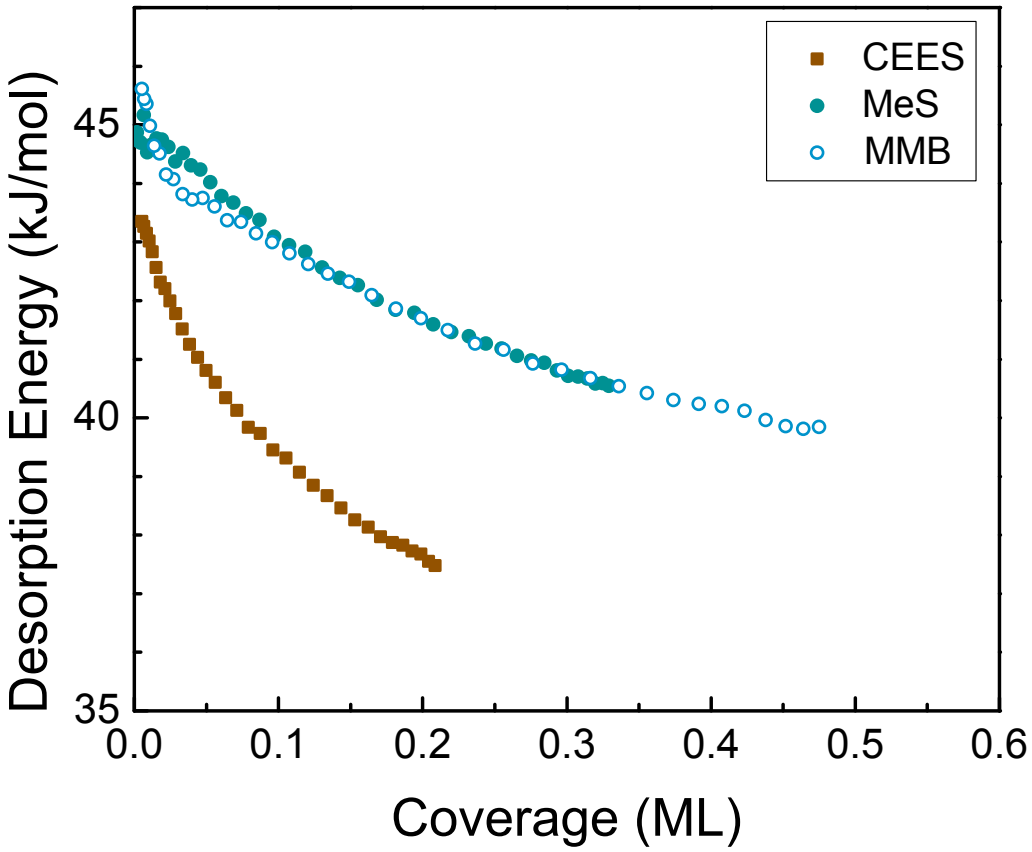

Figure 4.19: Desorption energy as a function of coverage for 2-CEES (1 x $10^7 s^{-1}$), MMB and MeS (2 x $10^6 s^{-1}$).

2-CEES. For MeS and MMB, over the range of zero coverage up to 0.5 ML, the desorption energy approaches 40 kJ/mol and at the lowest coverages, the desorption energy is about 45 kJ/mol. The similarity between the MeS and MMB profiles, suggests that both molecules form the same type of hydrogen bonding interaction, the carbonyl group. However, the data is also

consistent with the possibility that MeS adsorbs via the hydroxyl group and MMB via the carbonyl, provided that the strengths of these interactions are identical. In order to make this determination, additional experiments comparing small-molecule alcohols and carbonyl containing molecules will be completed.

4.4 Summary

The goal of this chapter was to investigate the fundamental interactions between two mustard simulants, 2-CEES and MeS, with silica. IR spectroscopy was used to determine that each of the simulants investigated adsorb through the formation of hydrogen bonds to surface silanols as evidenced by the changes of the ν(OH) modes in the IR spectra. For 2-CEES to adsorb to the 225 K silica surface, two hydrogen bonds must form, one between a free hydroxyl group and the Cl moiety and another between a different free hydroxyl group and the S moiety. The desorption energy of 2-CEES from our surface ranges from 37 to 44 kJ/mol, and is strongly dependent upon coverage. MeS is suspected to adsorb to the silica through the carbonyl oxygen, as supported by the identical desorption energy of the similar molecule, MMB; however, it is not possible rule out adsorption through the hydroxyl group. The desorption energy for MeS and MMB ranges from 40 to 45 kJ/mol in the range of 0.5 to 0 ML coverages.

Beginning to evaluate MeS and 2-CEES as appropriate simulants for studying the interactions of mustard with hydrogen-bonding surfaces, we observe that both simulants adsorb within about 5 kJ/mol of each other. However, a key difference is that MeS only forms one hydrogen bond with the surface, and 2-CEES forms two. For highly hydroxylated surfaces, live mustard is expected to adsorb even more strongly than 2-CEES because it has an additional chlorine atom. Based on the different number of hydrogen bonds possible, the degree of surface hydroxylation can play a large role in the adsorption of mustard and mustard simulants on

surface. At low hydroxylation levels MeS and 2-CEES may both serve as an appropriate simulant; however, at higher hydroxylation levels, mustard may adsorb significantly more strongly than both simulants tested here. To test this hypothesis, as well as explore many other CWA and surface interactions, a new surface science instrument was designed and constructed which is described in the following chapter.

Chapter 5

Experimental Approach for Agent-Surface Studies

5.1 Introduction

The focus of the work presented in this chapter is the development, design, and construction of an instrument for studying the fundamental reactions between chemical warfare agents (CWAs) and militarily or environmentally relevant surfaces. Currently in the literature, nearly all of the experiments with CWAs are conducted in solution or under atmospheric conditions.[6,7] By completing experiments with so many unknown variables it is difficult to understand how the individual components and properties of the reacting species affect the overall reaction pathway. Therefore, for the rational design of next generation of CWA sorbents, sensors, and decontaminants, we need to develop a detailed understanding of the reactions as the gas-surface interface.

Much of the research related to CWA chemistry, including work performed in our group, focuses on using simulants to begin making predictions about how live agent reacts with different surfaces; however, the degree of similarity between agents and their simulants remains largely unknown. Through the development of a new instrument capable of handling live agent experiments, we can learn about the fundamental chemistry of agents, but also make direct comparisons between agent and different simulants. Then, it may be possible to evaluate which simulants are most appropriate for a given system. In addition, the literature contains a great deal of studies with simulants. My goal is to help put this work into context.

To study chemistry at the fundamental level, it is important to have a very clean, well-characterized system. As described in Chapter 2, by conducting experiments in an ultrahigh vacuum (UHV) environment, we achieve a system in which we have high control over the

surface, gas, and their environment. By working in the UHV range, collisions are reduced. A characterized surface sample remains clean throughout the duration of an experiment and does not become contaminated with background gases. For example, at atmospheric pressures, a one-cm^2 sample becomes covered with a monolayer in less than about one nanosecond, assuming a sticking probability of one. However, by working in UHV conditions, 1 x 10^{-9} torr, the monolayer formation time is extended to nearly an hour, which is a reasonable amount of time to conduct an experiment. Also, under UHV conditions, the mean free path of the gas molecules (~50 km at 10^{-9} torr), is sufficiently long so that the majority of gas molecules do not collide with each other, rather only the surface of interest. With these experimental conditions, it becomes possible to learn the basic reactions that occur when a surface is exposed to a CWA agent.

5.2 Description of Chamber

5.2.1 Overview of Chamber Design

The new UHV instrument was designed with the aim of gaining knowledge of the fundamental gas-surface interactions, with particular interests in CWA chemistry. To develop a complete picture of the interfacial chemistry, multiple analytical instruments are coupled to the UHV chamber, allowing for experiments investigating the uptake, diffusion, decomposition, and desorption to be conducted. The following table presents key experimental objectives and the corresponding approaches to help achieve the detailed understanding we desire. An overall schematic of the instrument, which addresses each of these goals, is shown in Figure 5.1.

Table 5.1 Experimental goals and corresponding experimental approaches.

Experimental Objective	Experimental Approach
Complete experiments under a wide pressure range; 10^{-9} to 10^{2} torr	Turbomolecular pumps with valve system
Control surface temperature and position	Precision manipulator with heating and cooling
Rapid sample introduction	Load lock system with transfer arm
Surface characterization (before and after sample exposure)	Reflection absorption infrared spectroscopy, X-ray photoelectron spectroscopy
Controlled agent/simulant/gas flux	Multiple dosers; for high and low vapor pressure molecules, and background or decontamination gases
Monitor surface adsorbates during exposure	Reflection absorption infrared spectroscopy
Monitor gas-phase products during exposure	Mass spectrometry
Measure reaction kinetics	Reflection absorption infrared spectroscopy Mass spectrometry
Measure adsorbate desorption energy	Temperature-programmed desorption
Complete experiments with agent *safely*	Surety fume hood, interlock, burst disc, venturi tube, agent compatible materials

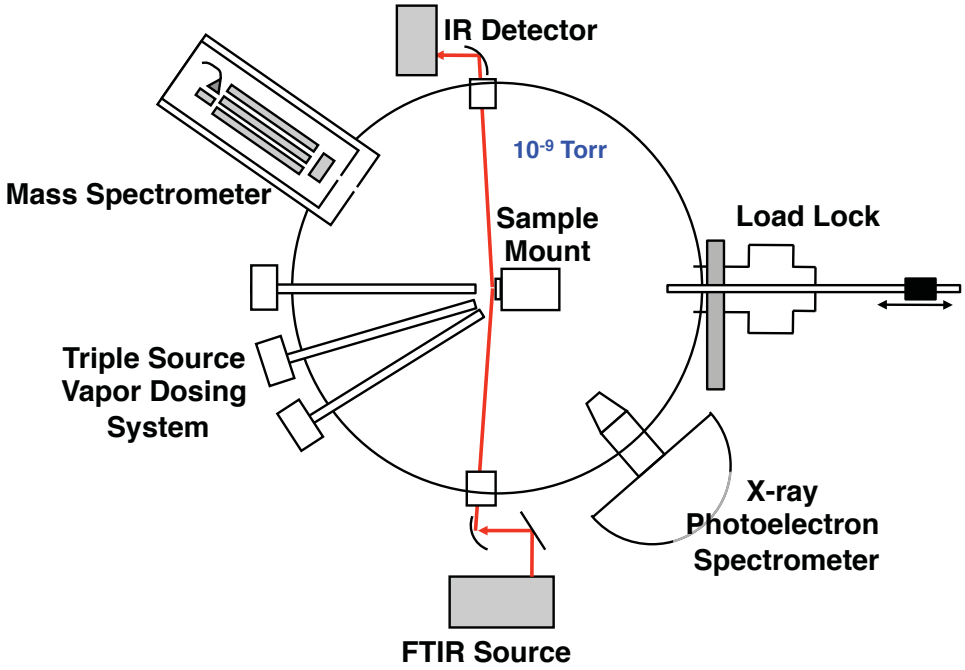

Figure 5.1: Schematic of the surface analysis instrument, showing key design features.

5.2.2 Chamber Construction

The UHV instrument is composed of several custom-designed chambers. Each chamber is constructed of 304 stainless steel. Stainless steel has a low outgassing rate and is mechanically strong, making it an ideal material for many UHV applications. The chambers and other external components are connected to each other by ConFlat™ flanges. ConFlat flanges have a thin knife-edge and are sealed with an oxygen-free, high conductivity, copper gasket. As the flange is tightened, the knife-edge makes a groove into the copper. The copper, being a soft metal, flows and fills small imperfections in the knife-edge, thus creating a leak-tight seal capable of maintaining vacuum levels below 10^{-13} torr.

The main chamber is a cylindrical dome constructed from 1/8" thick 304 stainless steel and has a volume of approximately 23 L. The chamber contains 19 ports. The positions of the ports are provided Figure 5.2 and their sizes, focal lengths, and the equipment to be attached to each flange are provided in Table 5.2.

Table 5.2: Main chamber port dimensions.

Port	Flange Size (inches)	Focal Length (inches)	Azimuthal Angle	Polar Angle	Equipment
A	2 ¾	7.00	0°	90°	IR spectrometer
B	2 ¾	7.00	188°	90°	IR detector
C	14	9.50	0°	180°	Main turbo
D	6	7.00	0°	0°	Manipulator
E	8	7.00	267°	90°	Mass spectrometer
F	6	7.00	132°	90°	Load lock
G	6	6.87*	60°	90°	XPS Analyzer
H	6	8.50	312°	45°	Viewport
J	2 ¾	7.00	200°	45°	Residual gas analyzer
K	6	10.00	95°	45°	Viewport
L	2 ¾	9.50*	60°	45°	X-ray source
M	2 ¾	7.00	312°	90°	Solid sorbent doser
N	2 ¾	7.00	222°	90°	Capillary array doser
P	2 ¾	7.00	245°	45°	Burst disc
Q	2 ¾	9.00	230°	112°	Viewport
T	2 ¾	7.00	155°	45°	Gauge
U	2 ¾	7.00	20°	45°	Gauge
V	2 ¾	8.00	322°	114°	Leak valve doser
X	2 ¾	7.00*	110°	90°	Ion gun

*The focal point of these ports is 4" below the center of the chamber.

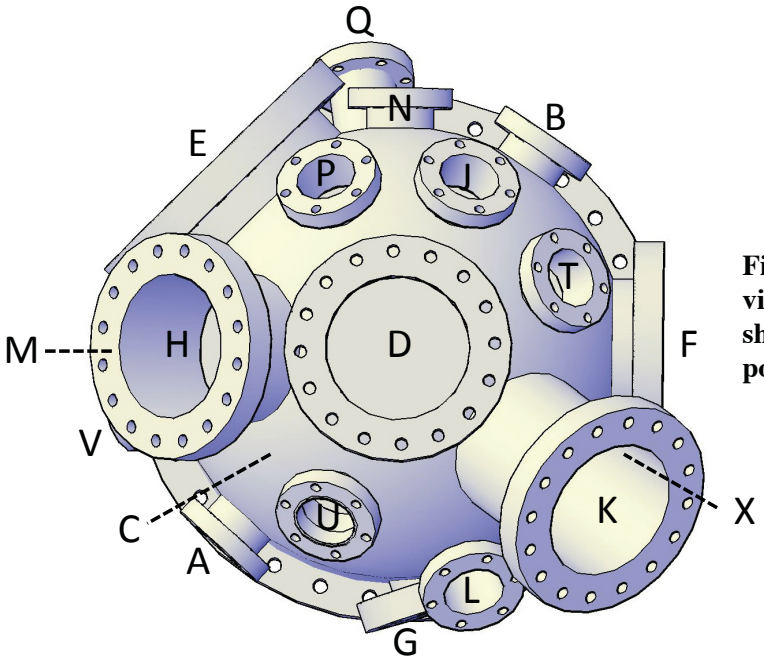

Figure 5.2: Diagram of the top view of the main chamber, showing the locations of the 19 ports.

A schematic showing the chamber assembly, including key instrumental equipment is provided in Figure 5.3.

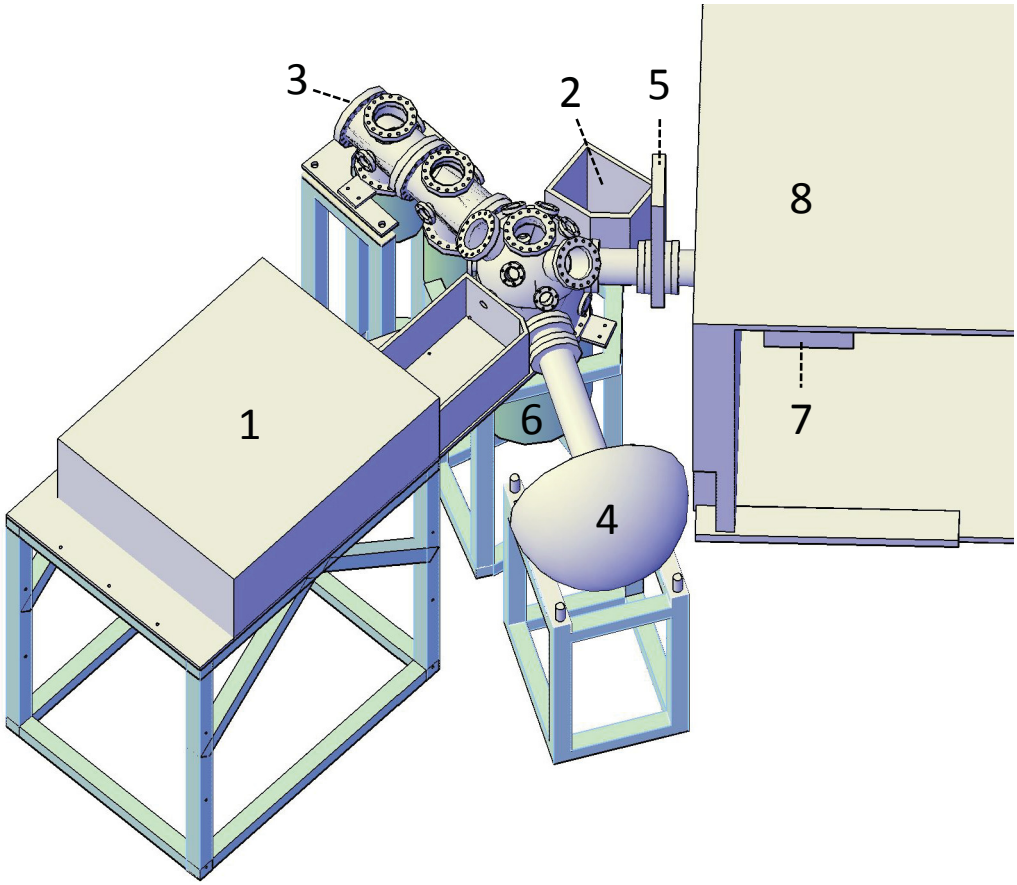

Figure 5.3: Diagram of the entire UHV instrument, including key instrumental equipment. The labeled components are: (1) FTIR spectrometer, (2) IR detector box, (3) mass spectrometer port, (4) XPS hemispherical energy analyzer, (5) manual gate valve, (6) magnetically levitated turbomolecular pump, (7) load-lock chamber, (8) chemical fume hood.

5.2.3 Achieving Vacuum

The first requirement in the instrument design was that experiments must be able to be conducted in UHV conditions. By working at a dynamic range of pressures, we can investigate

the basic interactions, in the absence of background gases, but also at higher, more realistic pressures to study the effects of important atmospheric gases on the interfacial chemistry.

To achieve vacuum, specialized pumps were selected based upon their pumping speeds, reliability, corrosion resistance, materials, and cost. The main chamber is primarily pumped with a 2200 L/s magnetically levitated turbomolecular pump (Edwards Vacuum, A2203C) that is attached to Flange C. Commonly referred to as "turbo" pumps, these pumps are oil-free, can be mounted in many orientations, have minimal vibrations, and can be maintenance free for up to ten years. A turbo pump cannot pump against atmospheric pressures, and needs to be backed by a roughing pump to lower the backing pressure to about 10^{-3} torr. A scroll pump (Edwards, XDS-35i), which can be isolated from the turbo with a pneumatic gate valve (Kurt, J. Lesker, SA0150PVQF), was selected to back the turbo pump. A key advantage of scroll pumps is that they are oil-free. Working with such highly toxic molecules, creating an agent-contaminated oil reservoir would create a significant safety risk.

Another design choice motivated by safety was the selection of the foreline seals. The foreline consists of the hardware connecting the turbo pump and the backing pump. Typically, quick connect (KF) flanges with rubber o-rings are used for the foreline seals and are sufficient at holding the necessary low vacuum. However, in dealing with CWAs, the potential exists for agent to diffuse through the o-ring material and out into the lab space. To eliminate this risk, all-metal seals (Ebara) were used in all of the foreline connections.

The risk of diffusion of agent though o-ring seals was also addressed in regard to the scroll pump. While the scroll pump does not contain oil to act as an agent reservoir, the pump does contain rubber tip-seals that have the potential to accumulate agent. Therefore, to reduce

exposure to agent from the scroll pump, it is located within a surety fume hood, which is within engineering controls.

The pressures in the main chamber and at the scroll pump are continually monitored. The main chamber can be monitored with a full range gauge (Kurt J. Lesker, PTR26002) and nude ion gauge (Kurt J. Lesker, KJLIGC10N). The redundancy in pressure monitoring is used in the case that one gauge malfunctions, experiments can continue without needing to decontaminate the chamber and vent to atmosphere to replace the broken gauge. A pirani gauge (Kurt J. Lesker, KTR32130) is used to monitor the pressure in the foreline.

5.2.4. Sample Control

The next requirement of the instrument design was the incorporation of a sample holder in which we had precise control over the sample position and temperature. Precise sample positioning is essential because a number of the instrumental techniques require a different set of coordinates for ideal operation. Also, the control over sample temperature allows us to study chemistry below and above room temperature. Some adsorbates may not stick to a surface at room temperature, and by cooling the sample, we can still study the adsorption and reactions of these molecules. Heating the sample is used in temperature-programmed desorption experiments to learn the adsorption strength of molecules. Furthermore, rate and diffusion constants, as well as activation energy barriers, can be measured by conducting identical experiments, but with the surface held at different temperatures. These sample control requirements were achieved with a custom manipulator from Thermionics (STLC transfer system). The manipulator is mounted to the 6" flange on the top of the chamber (Flange D) and provides translation of ± 0.5" in the x and y directions, ± 8" in the z direction, 360° rotation, and ± 10° tilt. This wide range and precise

control we have in sample positioning is essential for transferring samples in and out of the chamber and for use with our different pieces of analytical instrumentation.

Sample are mounted onto a molybdenum platen and secured in place with three flexible stainless steel tabs. A thermocouple tab, as part of a transferrable, type-K thermocouple system, can also be secured on top of the sample for monitoring the surface temperature. The platen can accommodate samples as large as 1.5" in diameter, and approximately up to 1/8" thick. To attach the platen to the manipulator, the platen is precisely aligned with four flexible "finger-tabs" located on the manipulator and the platen is rotated clockwise to secure it in place, providing good thermal contact and connection with the thermocouple. A photograph of the sample platen attached to the manipulator is shown in Figure 5.4.

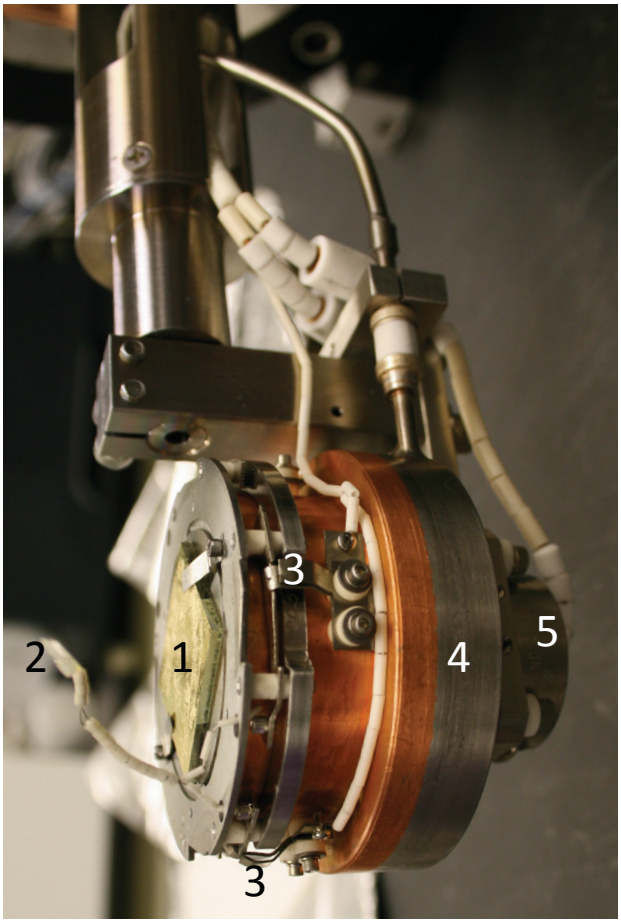

Figure 5.4: Photograph of sample platen and manipulator. The labeled components are: (1) silica coated 1" Au slide sample, (2) unsecured thermocouple tab, (3) finger tabs that secure the sample platen to the manipulator, four total but only two are visible in this photo, (4) LN_2 reservoir, (5) reference thermocouple.

The sample can be heated and cooled to anywhere between 150 and 1000 K. Heating is accomplished through the resistive heating of tungsten filaments located directly behind the sample platen, which is controlled by an integrated power supply and PID controller (Eurotherm). Cooling is achieved by flowing liquid nitrogen or cooled nitrogen through the manipulator reservoir. The surface temperature is monitored by the secured thermocouple tab. Additionally, a thermocouple spot-welded to the manipulator is used as a reference temperature.

5.2.5 Sample Loading

The next key criteria in our design was the implementation of a fast, reliable, and safe method to transfer samples in and out of the main chamber. This goal was achieved by using a load lock chamber that can be isolated from the main chamber with a 6" manual gate valve (Kurt J. Lesker, SG0400MCCF). The load lock chamber can be evacuated with a pumping station (Pfeiffer, HiCube 80 Eco), which consists of a 70 L/s turbo pump backed by a diaphragm pump. Through this approach, the main chamber can be kept under UHV conditions while only the load lock chamber is vented to atmospheric pressures for exchanging samples. Samples are introduced and removed from the main chamber using a linear rotary precision magnetically coupled transfer arm with 52" of linear travel (MDC Vacuum, 665088). To achieve precise alignment when making transfers, a gimbal (McAllister Technical Services, McTilt200) is also used to compensate for drooping of the transfer arm when it is fully extended.

The entire load lock assembly is located in a chemical fume hood. Therefore, any agent used for an experiment is contained within the fume hood or the UHV chamber. To introduce a new sample into the UHV chamber, the 6" gate valve is closed to isolate the main chamber and keep it under UHV. The turbo pump on the load lock chamber is turned off and the load lock is vented with nitrogen. Once at atmospheric pressure, the load lock door is opened, the platen is

removed, and a new sample is secured to the platen. The platen is then replaced onto the transfer arm. When placing the platen on the arm, it is important to note the orientation of the TC leads. These leads must be matched to the TC leads on the manipulator. It is possible to successfully secure the platen to manipulator, without having the TC leads in the proper position, making it impossible to read the sample temperature. After the platen is secured to the transfer arm, the load lock door is closed and the turbo pump is restarted. Once the pressure in the load lock chamber, according to the full range gauge, is below 5×10^{-7} torr, the gate valve is opened and the sample can be loaded into the chamber. When securing the platen to the manipulator, precise alignment is of the upmost importance. Transfers attempted with poor alignment can cause the finger tabs (refer to figure 5.4) to bend, which weakens the contact between sample and manipulator causing a short circuit of the TC and poor sample cooling. However, because the manipulator can be rotated, tilted, and moved in the x, y, and z directions, and the transfer arm can be tilted and moved in the x and y directions, achieving the precise alignment required is only a matter of patience. After successful transfer, the transfer arm is retracted and the gate valve is closed.

5.2.6 Sample Exposure

The next design goal was the need to safely introduce different gases for sample exposure. Potential gases include agents of both high and low vapor pressures, as well as possible oxidizing decontamination formulations. Because the gases have a wide range in physical and chemical properties, three dosers were designed to be well suited for each of the different types of gases.

5.2.6.1 Leak Valve Directional Doser

The first doser is used for the higher vapor pressure agents, including sarin and mustard. The dosing setup begins in the fume hood with a stainless steel agent cartridge. This cartridge is made from drilling out a standard ¼" VCR plug making them relatively cheap and easily disposed of once experiments are completed. Once spiked with agent, the cartridge is attached to a stainless steel manifold also in the fume hood. The manifold is connected to 1/8" stainless steel tubing with VCR fittings and is attached in series to a bellows sealed valve (Dibert Valve, SS-4BG-V51), right angle valve (Agilent, 9515014), variable sapphire-plate precision leak valve (Agilent, 9515106), multiplex flange (Kimball Physics, MCP275), then to the UHV chamber at flange V. As a component of the multiplex flange, a ¼" diameter stainless steel tube is used to provide for directional dosing. The dosing tube is threaded at one end, and is screwed into a tapped, double-sided mini conflat flange. This tube extends to approximately 3" away from the sample surface. A schematic of the dosing assembly is shown in Figure 5.5.

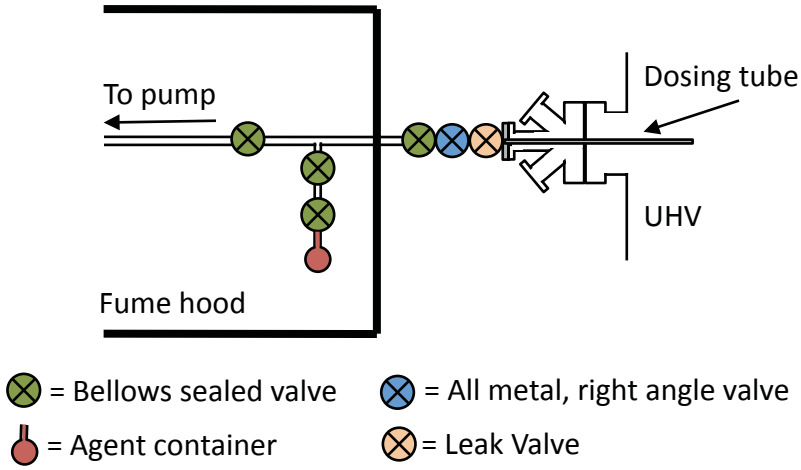

Figure 5.5: Schematic of leak valve directional doser assembly.

Dosing begins by spiking the clean cartridge with approximately 20 μL of agent. The cartridge is then attached to the manifold, which can be evacuated with the same turbo pump used for the load lock chamber. The agent is purified with freeze-pump-thaw cycles. Once the agent is purified, pumping of the dosing line is isolated by closing the valve leading to the turbo pump. Then, all other valves between the agent cartridge and the leak valve are opened. The agent flux into the chamber is regulated by the leak valve. On the vacuum side, agent travels through the dosing tube providing a directional flux of agent.

To address additional safety concerns regarding the directional doser, additional steps were taken in the design process to plan for removal of the dosing line and/or chamber venting. First, the approach of directional dosing, as opposed to backfilling the chamber, is appealing because it limits both the amount of agent required for an experiment and the time it takes to completely an experiment. With the directional dosing tube, the agent flux at the surface is significantly higher, thereby exposing the rest of the chamber to less agent. Also, because the dosing time is shorter, the experimenter is working with neat agent for less time. A second design consideration was preparing the dosing line in a way that it could be safely removed if necessary. In case that the atmospheric side of the dosing line needs to be removed, the 1/8" stainless steel dosing line is wrapped in heat tape to desorb or decompose the contaminated lines. This line is also heated and evacuated when switching agents to avoid unintentional co-dosing. Also, the redundancy in valves (the combination of the bellows sealed valve, right angle valve, and leak valve) makes it possible, that in the need to remove the dosing line, all of these valves could be closed, then the seal between the bellows sealed valve and right angle valve could be broken. The volume between these valves is minimal and would be evacuated and baked-out, reducing the concentration of agent. In case that any of these three valves fails, two valves

remain to isolate the chamber and the dosing line, making safe removal of the line for repair possible. On the vacuum side, the dosing tube itself can be heated to desorb any agent. Heating is done with a coiled nozzle heater (OEM) wrapped around the ¼" diameter dosing tube. At the end of the coil, is an internal type K thermocouple that is connected to a digital PID controller. A photograph of the dosing tube with heater is shown in Figure 5.6.

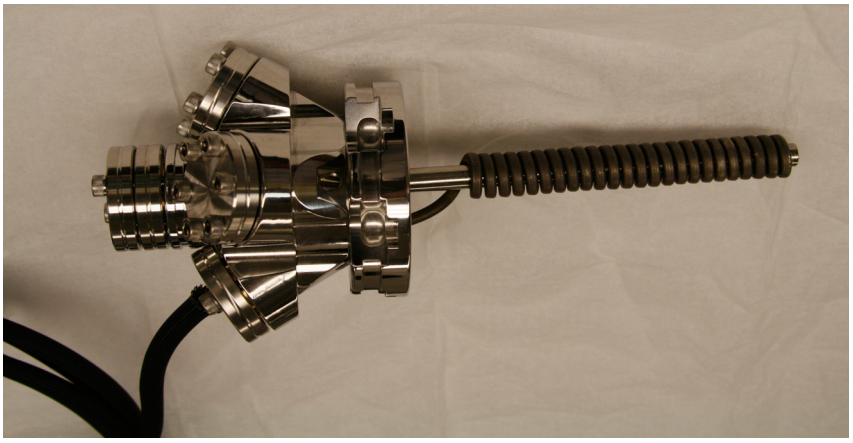

Figure 5.6: Picture of the directional doser with heating coil.

5.2.6.2 Solid Sorbent Doser

The next doser is a solid sorbent doser specifically designed for dosing lower vapor pressure agents, including VX. A key advantage of this doser is that all components are contained within the load lock and main UHV chamber; there are no external dosing lines. The basic principle is that a cartridge spiked with agent can be loaded into the load lock chamber then transferred into the main UHV chamber. Once in the UHV chamber, agent could be dosed with a well-controlled flux.

The solid sorbent doser is positioned at Flange M, which is directly across from the transfer arm. At this flange, is a liquid nitrogen cooled cryostat head (Janis, ST-400-1). The cooling is required for the controlled agent dosing. Once the agent cartridge is loaded, it can be

cooled, then slowly heated with a PID controller (Janis, Lakeshore 331S) to desorb the agent and dose the sample. The cryostat is mounted on a translation stage with 4“ of travel (McAllister part #), which allows for the agent cartridge to be moved to within 1/8” of the sample during dosing. The cryostat is also fitted with a stainless steel piece with a ¼”-20 tapped hole which serves as the cartridge receptacle.

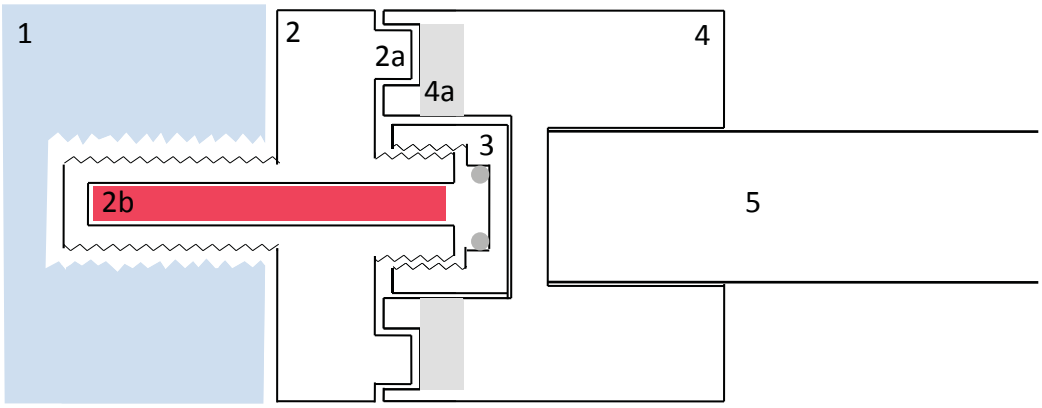

Figure 5.7: Diagram of *in vacuo* solid sorbent doser. The labeled components are: (1) cryostat receptacle, (2) sorbent cartridge including (2a) alignment posts and (2b) sorbent spiked with agent, (3) cap with o-ring, (4) transfer arm adapter including (4a) magnets, and (5) transfer arm.

The cartridge components shown in Figure 5.7 are machined from 400 series, magnetic, stainless steel. The bulk of the cartridge is threaded to match the cryostat receptacle and is bored out to retain the solid sorbent and agent. On the opposite of end of the cartridge are two posts used for alignment and cartridge transfers. There is also a portion that is reverse-threaded to which a cap can be secured. The cap is essential for retaining agent in the cartridge that would otherwise be pumped away during transfer into UHV. The cap is sealed with an o-ring and can be removed in vacuum. For transferring the cartridge in and out of the chamber, and for removing the cap, a custom adapter was machined for the transfer arm. One end of the adapter is machined to mate with the transfer arm and is secured in place with a set screw. The other end is

machined to slip fit the cartridge cap and to fit the alignment posts of the cartridge. Two rare earth magnets are press fit into the adapter to help secure the cap and cartridge during transfers.

The procedure for dosing using the solid sorbent doser is as follows. In the fume hood, the cartridge is spiked with approximately 20 μL of agent. Then the cap is secured. The cartridge/cap assembly is loaded into the load lock and positioned onto the transfer arm adapter. While the magnetic strength of the rare earth magnets is enough to hold the cap in place, it is essential that the posts of the cartridge piece are also aligned with the adapter. These posts are responsible for rotating the cartridge into the cryostat receptacle. If these posts are not aligned with the adapter, dropping the cartridge in the UHV chamber when attempting the cartridge loading is inevitable. Once the cartridge/cap assembly is secured in the load lock, the load lock chamber is evacuated with the turbo pump. During evacuation, the sample in the main chamber needs to be raised to allow for the transfer arm with cartridge to pass beneath it. Once the pressure is below 5×10^{-7} torr, the gate valve between the main chamber and load lock can be opened. The cartridge is transferred into the chamber and aligned with the cryostat. Alignment at this step is relatively easy, as the tapped end of the cartridge is tapered and self-aligns. Then the transfer arm is rotated clockwise to screw the cartridge and cap into the receptacle. When the cartridge is secured the transfer arm is pulled directly back until it is time to remove the cap and begin dosing. The cryostat is cooled so when the cap is removed there is not a large pressure burst of gas in the main chamber and so agent dosing can be well controlled. When it is time to being dosing, the transfer arm is aligned with the cap. Again alignment is relatively easy as the edges are tapered. To remove the cap the arm is again rotated clockwise. This rotation unscrews the cap, which is reverse-threaded, but does not loosen the cartridge. At this stage the sample is lowered into position and the cartridge can be heated to dose the agent. To remove the cartridge,

the same transfer arm adapter is used as for cartridge loading. The transfer arm adapter, which still houses the cap, is aligned with the cartridge and the arm is rotated counter-clockwise. This rotation begins to screw the cap back on, then unscrews the cartridge from the cryostat. The cartridge is then removed from the main chamber and preparations can be made for the next experiment.

5.2.6.3. Capillary Array Doser

The last doser is intended for dosing atmospheric and decontamination gases. This doser, positioned at flange N, is a variable flux microcapillary array doser based on a design by Fisher and Meserole.[102] A schematic of the doser is shown in Figure 5.8.

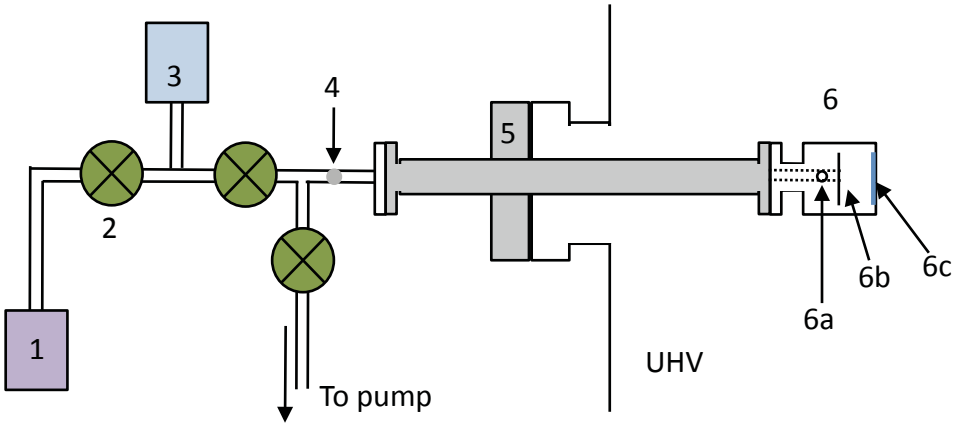

Figure 5.8: Diagram of capillary array doser. The labeled components are: (1) gas container, (2) bellows sealed valve, (3) capacitance manometer, (4) 10 μm aperture (5) hollow linear motion feedthrough, and (6) dosing flange including (6a) 0.10" hole, (6b) baffle plate, and (6c) glass capillary array.

The core component of the doser is a metal-sealed, hollow linear motion feedthrough with 4" stroke (Thermionics,FLMH-275-50-4). On the vacuum side of the doser is a glass capillary array (GCA) that has 10-micron pores with a center-to-center spacing of 12 microns (Photonis, PS310171). The GCA is secured at the end of a hollow stainless steel cylinder with a thin baffle plate to randomize the motion of the gas molecules. On the atmospheric side, the feedthrough is attached to a manifold. The manifold consists of a series of valves and stainless

steel tubing. In line with the tubing is a 10 μm aperture to control the gas flux into the chamber. The manifold can be evacuated, then backfilled with the gas to a known pressure, as measured by a capacitance manometer gauge (MKS instruments). By using a calibrated gas volume and known pressure, it is possible to calculate the flux of gas molecules hitting the surface sample.

5.2.6.4. High Pressure Dosing

For some experiments, the capability to dose or study chemistry at pressures higher than UHV may be desired. The main turbo pump cannot operate at these higher pressures and turning off the pump completely does not provide suitable pumping. Therefore, a 10" manual gate valve (Kurt J. Lesker) was placed between the main chamber and the main turbo pump (Flange C in Figure 3-2). This gate valve can be throttled to vary the conductance and obtain an ideal effective pumping speed for the main chamber for high pressure dosing. An additional feature of the gate valve is in regards to safety. In the event that the turbo pump needs to be replaced or repaired, this gate valve can be closed to isolate the UHV chamber, and any agent it contains, from the lab space.

The main chamber is constructed to withstand the large pressure differential of UHV on the inside and atmosphere on the outside. However, it is not designed to contain extremely high pressures. Therefore to protect sensitive equipment or mechanical failure in the event of over-pressurization, a burst disc is positioned on the main chamber (Flange P in Figure 3.2). If at anytime, the pressure exceeds 1300 torr, the stainless steel disc releases and the gas is exhausted into the chemical fume hood.

5.2.7 Analytical Instrumentation

In order to develop a detailed understanding of the reactions at the gas-surface interface, three key pieces of analytical instrumentation are coupled to the UHV chamber. An FTIR

spectrometer and mass spectrometer can be used to monitor reactions during dosing and an x-ray photoelectron spectrometer (XPS) can be used for surface characterization before and after dosing. The following sections describe each of these key pieces of instrumentation in more detail.

5.2.7.1 FTIR Spectrometer

Fourier transform infrared spectroscopy (FTIR) is used to learn how the vibrational modes of the molecules on the sample surface changes upon exposure to either agent or other gas. By identifying the functional groups on the surface, reaction products, mechanisms, and rates can often be determined.

A Bruker Vertex 80V vacuum FTIR spectrometer is coupled to the main UHV chamber as shown in Figure 3-9. The spectrometer itself is kept under low vacuum, and the external optics are housed in nitrogen purged enclosures. Within the spectrometer, light from a SiC, mid IR source passes through an aperture wheel then through a Michelson interferometer with KBr beamsplitter. A gold-coated flat mirror directs the beam out of the spectrometer and into the first external optics enclosure. This enclosure houses a flat mirror and parabolic mirror to focus the beam onto the sample in the center of the UHV chamber. A KBr window positioned at Flange A enables the beam to pass into the UHV chamber. After the beam is focused on the sample, it begins to diverge as it leaves the chamber though a second KBr window and into the second nitrogen purged optics enclosure. Here, an ellipsoidal mirror focuses the diverging beam onto a mid-range (750-4000 cm^{-1}), liquid nitrogen cooled mercury-cadmium-telluride (MCT-A) detector. Typical spectrometer settings for our setup produce spectra that are the average of 100 scans, collected with 2 cm^{-1} resolution, 3 mm diameter aperture, and 20 kHz scanner velocity.

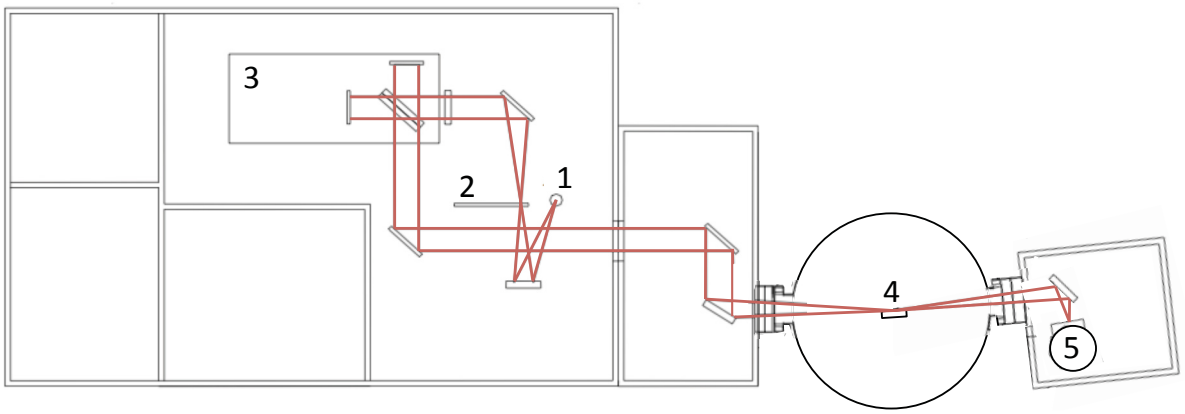

Figure 5.9: Schematic of the IR path through the spectrometer, optics enclosure, UHV chamber, and detector box. The labeled components are: (1) SiC globar source, (2) variable aperture wheel, (3) interferometer, (4) sample within the UHV chamber, and (5) MCT detector.

5.2.7.2 Mass Spectrometers

A mass spectrometer is used to monitor any gas-phase products or molecules desorbing from the sample surface. A key advantage of using the mass spectrometer in conjunction with the IR, is that it is often difficult to determine the identity of surface species when IR is the only spectroscopic tool. Although IR can give useful information about which bonds are present, not all bonds are IR active and it is not always possible to know exactly what the adsorbed molecule is, even if many of its bonds are known. The mass spectrometer can detect the gas-phase reaction fragments, which will provide information about what remains on the surface.

The mass spectrometer used for much of this work is an Extrel quadrupole mass spectrometer (Extrel, MAX1000880APP3/4P8), which has a 2-1000 amu range with better than 1 amu resolution. The axial ionizer of the mass spectrometer breaks apart the gas-phase molecules into characteristic fragments that are separated base on their mass to charge ratio over the length of the quadrupole rods. The fragments are then detected with a channel electron multiplier.

This spectrometer is doubly differentially pumped. The two differential stages are separated from the main chamber with a 0.106" and 0.019" diameter aperture and each stage is pumped with a 480 L/s magnetically levitated turbomolecular pump (Edwards STP-451C). The configuration is identical to that described in Chapter 2 (see figure 2.7). Through differential pumping, the main chamber pressure can be above 10^{-6} torr, which may occur during dosing, but the mass spectrometer chamber stays under UHV conditions, which are essential for its operation. If at anytime the full range gauge positioned on the mass spectrometer chamber reads a pressure above 10^{-7} torr, the mass spectrometer is programmed to turn off. Additionally, the small apertures provide that the mass spectrometer only has a line of sight with the sample, ensuring that the molecules detected are those in the region of the sample surface.

A second mass spectrometer is also used. This residual gas analyzer (RGA) (Stanford Research Systems, RGA300) is attached directly to the main chamber at Flange J. The RGA has a 2-300 amu range with 1 amu resolution. This mass spectrometer is used to determine the purity of dosed gases. It is also scanned over the full mass range during dosing and desorption experiments. The Extrel mass spectrometer on the other hand, is often set to scan specific masses and because of the apertures, it is significantly more sensitive to species desorbing from the surface. Using both spectrometers together helps provide a complete picture of the molecules present in the chamber and specifically at the surface.

5.2.7.3 X-ray Photoelectron Spectrometer

X-ray photoelectron spectroscopy (XPS) is a surface sensitive analytical technique that provides information about which elements are present on a sample, as well as the chemical environment of those species. According to the photoelectric effect, core level electrons can be ejected from a sample when exposed to high-energy photons. The kinetic energy of the ejected

electrons is then used to determine the element and even oxidation state of the elements being analyzed.

In the field of chemical warfare agent decontamination, XPS can be a very powerful tool in not only understanding reaction mechanisms, but also evaluating the efficacy of decontamination formulations. Different samples may be exposed to agent, then a decontamination treatment, either in UHV or at atmospheric pressures. XPS could then be used to analyze how much agent remains on the surface and how effective the decontamination treatment was.

The XPS of our UHV instrument uses a dual anode (Al/Mg) x-ray source operating at up to 15 kV and 400 W (Sphera, B002096 DAR 400). The source emits monochromatic radiation at 1486.8 eV or 1253.6 eV for the Al or Mg anodes respectively. The ejected electrons are detected with a 17" hemispherical analyzer with a five-channel multiplier. (Sphera, B002026)

While XPS only provides information regarding the chemical identity of species at the surface, the identity of components within the bulk of the material can also be important. To obtain this type of information, an ion gun is positioned at Flange X to be used in conjunction with the XPS. The ion gun (Sphera, B002291), focuses a fine beam of ions into a 150 μm region which can sputter away layers of the sample. By rastering the region being sputtered, a three-dimensional elemental map could be generated. Experiments conducted using the ion gun with XPS could provide information about how agent diffuses through different materials.

5.2.8 UHV Instrument Interlock

When working with UHV equipment, especially equipment exposed to agent, it is essential that there is a system in place to protect the instrument and personnel in case of mechanical failure, power outages, or other unforeseen events. This protection is accomplished

through the implementation of a custom interlock program. The interlock program is written in the graphical programming software, Labview, which serves as an interface between pressure gauges, switches, Fieldpoint relays, valves, and pumps. The program continually monitors the pressure at different regions of the instrument and is designed such that if the pressure in any region is abnormally high, the chambers are isolated and equipment automatically shuts down. The program and appropriate equipment can then be restarted once the initial problem causing the shut down is remedied.

5.3 Summary

In this chapter, the design and construction of a new UHV surface science instrument has been described. This instrument has unique capabilities allowing for experiments with live chemical warfare agents to be safely conducted. In order to develop better sorbents and decontaminants, the fundamental reactions and interactions of agents on surface needs to be studied. Each of the components described above have been extensively tested and operate as described. Additionally, experiments with live CWAs, specifically Sarin, have been conducted successfully and we are now contributing to the development of this basic agent-surface chemistry knowledge.

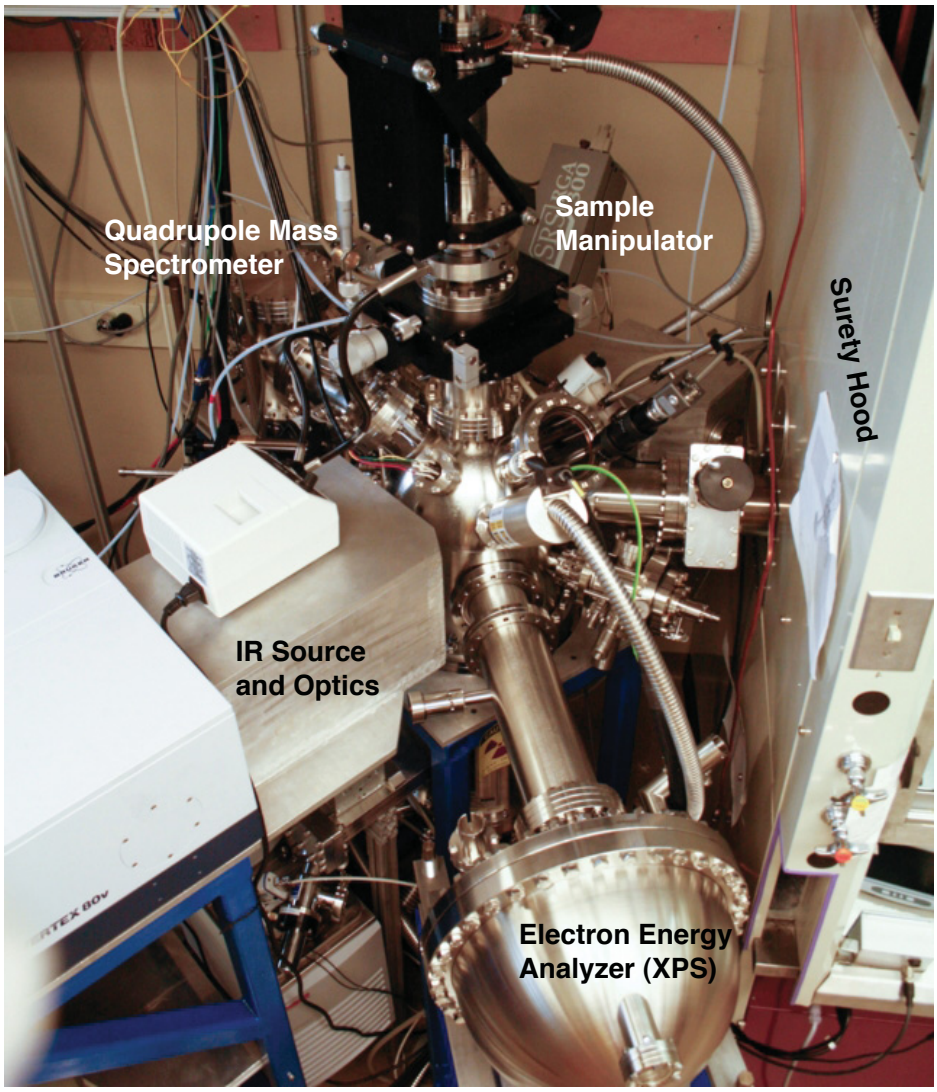

Figure 5.10: Photograph of the assembled UHV instrument at Edgewood Chemical Biological Center.

Chapter 6

Summary and Conclusions

6.1 Summary of Results

The main goal of my research was to develop a fundamental understanding of the interactions of CWA with amorphous silica. Developing a complete picture of the uptake, bonding, and chemistry of CWAs on surfaces is essential for the rational design of new sorbents, sensors, and decontamination strategies. Silica is specifically important because it is material that is prevalent in our environment. Also, it serves as a useful model for any surface where hydrogen-bonding interactions dominate. Many researchers use CWA simulants, chemicals chosen to mimic either the chemical or physical properties of agent without the high toxicity, to make predictions about the chemistry of live agents. However, few studies have been conducted that investigate how these structural and chemical differences affect the overall surface chemistry. Therefore, this thesis was aimed at developing an understanding of how small changes in simulant structure affect the overall chemistry, then correlate that knowledge to the chemistry of live agents. Additionally this work has described tools developed for studying many types of surface chemistry using live agents.

In order to study chemistry at such a fundamental level, experiments were conducted in a UHV environment. By working in UHV, we achieve a system in which we have high control over the surface, gas, and their environment. Modifications were made to the original UHV instrument to complete temperature-programmed desorption experiments to measure the activation energies for desorption for a variety of adsorbates. The surface and adsorbates were also characterized with transmission IR to gain insight into the adsorption mechanism.

The interactions of a series of organophosphate nerve agent simulants with amorphous silica were studied to learn how small changes in simulant structure affect their adsorption properties. For each of the simulants studied (DIMP, DMMP, TMP, DMCP, and MDCP), adsorption occurs through the formation of a hydrogen bond between the phosphoryl oxygen of the simulant and a free hydroxyl group of the silica surface. The activation energies for desorption where measured to be in the range of 43 to 60 kJ/mol. These energies were determined to be directly proportional to the charge of the phosphoryl oxygen. The magnitude of this negative charge is affected by the electron donating or withdrawing properties of the different substituents. From this relationship, and the contributions of computational work, the adsorption strength for the live agent, Sarin, is predicted to be 53 kJ/mol. The strength of the adsorbate-surface interaction was also observed in the IR spectra. The more strongly adsorbing simulants caused a greater shift of the SiO-H stretching frequency. This linear relationship of hydrogen-bonding strength and shift of the SiO-H mode, an empirical relationship first observed in the solution phase by Badger and Bauer, may enable others to make quantitative energy comparison based solely upon IR data.

Extending our work to a different class of CWAs, the interactions of two common mustard simulants with silica were also investigated. The IR data suggests that 2-CEES adsorbs to isolated silanols groups through the formation of two hydrogen bonds, one via the S and another through the Cl moiety. The desorption energy was found to be strongly dependent upon coverage, which is consistent with the observation of the bifunctional hydrogen bonding. At the coverages studied (0 ML to 0.20 ML) the desorption energy spanned from 37 to 43 kJ/mol. The other simulant, methyl salicylate, adsorbs to silica slightly more strongly. Over the same coverage range, the desorption energy was between 40 and 45 kJ/mol. The functional group

primarily responsible for adsorption is likely the carbonyl oxygen or hydroxyl oxygen. Extending the simulant data to live mustard is rather difficult, as the degree of surface hydroxylation plays a large roll in how many hydrogen bonds can form with the surface. For a highly hydroxylated surface, three hydrogen bonds may form between mustard and silica; however for a mostly dehydroyxlated surface only one bond may form.

In order to put the plethora of simulant work into context, a new surface science instrument was designed and constructed for work with live agent studies. The instrument allows for some of these most detailed agent studies possible. Combined with the simulant work, we can make direct comparisons between simulants and agents that will aid in choosing which simulants best model live agent chemistry for a given system. These fundamental studies will also contribute to the development of new agent detection and decontamination strategies.

6.2 Future Studies

Future studies are focused on concluding which functionality of the common mustard simulant, methyl salicylate, is responsible for adsorption. Studying the adsorption of benzene, methyl benzoate, phenol, formaldehyde, and methanol may help deduce which functional group is key for adsorption in methyl salicylate. This information is not only relevant to the field of CWA, but also for those interested in the adsorption of small molecules in general.

While the simulant work conducted thus far has contributed to the understanding of these small molecules to silica, the next step is to conduct parallel experiments using the live agents themselves. The first agent, currently being studied, is Sarin and was chosen because it has one of the simplest structures of the CWAs. Next, the interactions of Soman, VX, and mustard with silica will be investigated. Once these key studies have been completed, the chemistry of these

agents on other militarily and environmentally relevant surfaces can be explored, including other metal oxides, metals, and polymeric coatings.

6.3. Concluding Remarks

The ultrahigh vacuum studies presented here, have been conducted to develop a detailed understanding of the fundamental interactions of chemical warfare agent simulants with amorphous silica. The simulants can adsorb to isolated silanol groups of the silica surface as monitored with infrared spectroscopy and the strength of these interactions has been measured with temperature-programmed desorption techniques. Additionally, we have provided the necessary tools for conducting similar experiments with the actual chemical warfare agents. These studies can provide the tools for the next generation of detection and decontamination strategies.

References:

(1) Kolasinski, K. W. *Surface Science: Foundations of Catalysis and Nanoscience*; 2nd ed.; John Wiley & Sons Ltd: West Sussex, 2008.
(2) Somorjai, G. A.; Li, Y. *Introduction to Surface Chemistry and Catalysis*; 2nd ed.; John Wiley & Sons: Hoboken, 2010.
(3) Zaera, F. The Surface Chemistry of Catalysis: New Challenges Ahead. *Surface Science* **2002**, *500*, 947-965.
(4) Somorjai, G. A. Modern Concepts in Surface Science and Heterogeneous Catalysis. *Journal of Physical Chemistry* **1990**, *94*, 1013-1023.
(5) Talmage, S. S.; Watson, A. P.; Hauschild, V.; Munro, N. B.; King, J. Chemical Warfare Agent Degradation and Decontamination. *Current Organic Chemistry* **2007**, *11*, 285-298.
(6) Yang, Y. C.; Baker, J. A.; Ward, J. R. Decontamination of Chemical Warfare Agents. *Chemical Reviews* **1992**, *92*, 1729-1743.
(7) Kim, K.; Tsay, O. G.; Atwood, D. A.; Churchill, D. G. Destruction and Detection of Chemical Warfare Agents. *Chemical Reviews* **2011**, *111*, 5345-5403.
(8) *The Surface Properties of Silicas*; John Wiley & Sons: New York, 1998.
(9) *Adsorption on Silica Surfaces*; Marcel Dekker, Inc: New York, 2000; Vol. 90.
(10) *Colloidal Silica: Fundamentals and Applications*; CRC Press: New York, 2006; Vol. 131.
(11) Delfino, R. T.; Ribeiro, T. S.; Figueroa-Villar, J. D. Organophosphorus Compounds as Chemical Warfare Agents: A Review. *Journal of the Brazilian Chemical Society* **2009**, *20*, 407-428.
(12) Szinicz, L. History of Chemical and Biological Warfare Agents. *Toxicology* **2005**, *214*, 167-181.
(13) Kroening, K. K.; REaster, R. N.; Richardson, D. R.; Willison, S. A.; Caruso, J. A. *Analysis of Chemical Warfare Degredation Products*; John Wiley & Sons, Ltd.: West Sussex, 2011.
(14) Marrs, T. C. *Chemical Warfare Agents - Toxicology and Treatment*; 2nd ed.; John Wiley & Sons: West Sussex, 2007.
(15) Sidell, F. R. *Medical Aspects of Chemical and Biological Warfare-Texbook of Military Medicine*; Surgeon General, US Army: Washinton D.C., 1997.
(16) Lewis, R. J. *Sax's Dangerous Properties of Industrial Materials*; Van Nostrand Reinhold: New York, 1996.
(17) Munro, N. B.; Ambrose, K. R.; Watson, A. P. Toxicity of the Chemical Warfare Agents GA, GB, and VX: Implications for Public Protection. *Environmental Health Perspective* **1994**, *102*, 18-38.
(18) Bartelt-Hunt, S. L.; Knappe, D. R. U.; Barlaz, M. A. A Review of Chemical Warfare Agent Simulants for the Study of Environmental Behavior. *Critical Reviews in Environmental Science and Technology* **2008**, *38*, 112-136.
(19) Shakarjian, M. P.; Heck, D. E.; Gray, J. P.; Sinko, P. J.; Gordon, M.; Casillas, R. P.; Heindel, N. D.; Gerecke, D. R.; Laskin, D. L.; Laskin, J. D. Mechanisms Mediating the Vesicant Actions of Sulfur Mustard after Cutaneous Exposure.*Toxicological Sciences* **2010**, *114*, 5-19.
(20) Clayton, G. D.; Clayton, F. E. *Patty's Industrial Hygiene and Toxicology*; John Wiley and Sons: New York, 1993.

(21) Vijayaraghavean, R.; Kulkarni, A.; Pant, S. C.; Kumar, P.; Rao, P. V.; Gupta, N.; Gautam, A.; Ganesan, K. Differential Toxicity of Sulfur Mustard Administered through Percutaneous, Subcutaneous, and Oral Routes. *Toxicology and Applied Pharmacology* **2005**, *202*, 180-188.
(22) Dwyer, A. J.; Lewis, F. A.; Patrick, W. D.; Sidell, F. R. *Jane's Chemical-Biological Defense Guidebook*; Jane's Information Group: Alexandria, VA, 1999.
(23) Kuo, I. W.; Grant, C. D.; Gee, R. H.; Chinn, S. C.; Love, A. H. Determination of the Surface Effects on Sarin Degradation. *Journal of Physical Chemistry C* **2012**, *116*, 9631-9635.
(24) Aurian-Blajeni, B.; Boucher, M. M. Interaction of Dimethyl Methylphosphonate with Metal Oxides. *Langmuir* **1989**, *5*, 170-174.
(25) Henderson, M. A.; Jin, T.; White, J. M. A TPD/AES Study of the Interaction of Dimethyl Methylphosphonate with Iron Oxide (alpha-Fe_2O_3) and Silicon Dioxide. *Journal of Physical Chemistry* **1986**, *90*, 4607-4611.
(26) Kanan, S. M.; Tripp, C. P. An Infrared Study of Adsorbed Organophosphonates on Silica: A Prefiltering Strategy for the Detection of Nerve Agents on Metal Oxide Sensors. *Langmuir* **2001**, *17*, 2213-2218.
(27) Li, Y. X.; Klabunde, K. J. Nano-scale Metal Oxide Particles as Chemical Reagents. Destructive Adsorption of a Chemical Agent Simulant, Dimethyl Methylphosphonate on Heat-Treated Magnesium Oxide. *Langmuir* **1991**, *7*, 1388-1393.
(28) Li, Y. X.; Koper, O.; Atteya, M.; Klabunde, K. J. Adsorption and Decomposition of Organophosphorus Compounds on Nanoscale Metal Oxide Particles. In situ GC-MS Studies of Pulsed Microreactions over Magnesium Oxide. *Chemistry of Materials* **1992**, *4*, 323-330.
(29) Li, Y. X.; Schlup, J. R.; Klabunde, K. J. Fourier Transform Infrared Photoacoustic Spectroscopy Study of the Adsorption of Organophosphorus Compounds on Heat-Treated Magnesium Oxide. *Langmuir* **1991**, *7*, 1394-1399.
(30) Lin, S. T.; Klabunde, K. J. Thermally Activated Magnesium Oxide Surface Chemistry. Adsorption and Decomposition of Phosphorus Compounds. *Langmuir* **1985**, *1*, 600-605.
(31) Mitchell, M. B.; Sheinker, V. N.; Mintz, E. A. Adsorption and Decomposition of Dimethyl Methylphosphonate on Metal Oxides. *Journal of Physical Chemistry B* **1997**, *101*, 11192-11203.
(32) Obee, T. N.; Satyapal, S. Photocatalytic Decomposition of DMMP on Titania. *Journal of Photochemistry and Photobiology A: Chemistry* **1998**, *118*, 45-51.
(33) Rusu, C. N.; Yates, J. T. Adsorption and Decomposition of Dimethyl Methylphosphonate on TiO_2. *Journal of Physical Chemistry B* **2000**, *104*, 12292-12298.
(34) Templeton, M. K.; Weinberg, W. H. Adsorption and Decomposition of Dimethyl Methylphosphonate on an Aluminum Oxide Surface. *Journal of the American Chemical Society* **1985**, *107*, 97-108.
(35) Templeton, M. K.; Weinberg, W. H. Decomposition of Phosphonate Esters Adsorbed on Aluminum Oxide. *Journal of the American Chemical Society* **1985**, *107*, 774-779.
(36) Gordon, W. O.; Tissue, B. M.; Morris, J. R. Adsorption and Decomposition of Dimethyl Methylphosphonate on Y_2O_3 Nanoparticles. *Journal of Physical Chemistry C* **2007**, *111*, 3233-3240.
(37) Kanan, S. M.; Lu, Z. X.; Tripp, C. P. A Comparative Study of the Adsorption of Chloro- and Non-Chloro-Containing Organophosphorus Compounds on WO_3. *Journal of Physical Chemistry B* **2002**, *106*, 9576-9580.

(38) Bermudez, V. M. Computational Study of the Adsorption of Trichlorophosphate, Dimethyl Methylphosphonate, and Sarin on Amorphous SiO_2. *Journal of Physical Chemistry C* **2007**, *111*, 9314-9323.
(39) Bermudez, V. M. Quantum-Chemical Study of the Adsorption of DMMP and Sarin on gamma-Al_2O_3. *Journal of Physical Chemistry C* **2007**, *111*, 3719-3728.
(40) Kuiper, A. E. T.; Vanbokhoven, J.; Medema, J. The Role of Heterogeneity in the Kinetics of a Surface Reaction: I. Infrared Characterization of the Adsorption Structures of Organophosphonates and their Decomposition. *Journal of Catalysis* **1976**, *43*, 154-167.
(41) Wagner, G. W.; Bartram, P. W.; Koper, O.; Klabunde, K. J. Reactions of VX, GD, and HD with Nanosize MgO. *Journal of Physical Chemistry B* **1999**, *103*, 3225-3228.
(42) Wagner, G. W.; Koper, O. B.; Lucas, E.; Decker, S.; Klabunde, K. J. Reactions of VX, GD, and HD with Nanosize CaO: Autocatalytic Dehydrohalogenation of HD. *Journal of Physical Chemistry B* **2000**, *104*, 5118-5123.
(43) Wagner, G. W.; Procell, L. R.; O'Connor, R. J.; Munavalli, S.; Carnes, C. L.; Kapoor, P. N.; Klabunde, K. J. Reactions of VX, GB, GD, and HD with Nanosize Al_2O_3. Formation of Aluminophosphonates. *Journal of the American Chemical Society* **2001**, *123*, 1636-1644.
(44) Ekerdt, J. G.; Klabunde, K. J.; Shapley, J. R.; White, J. M.; Yates, J. T. Surface Chemistry of Organophosphorus Compounds. *Journal of Physical Chemistry* **1988**, *92*, 6182-6188.
(45) Panayotov, D. A.; Morris, J. R. Cataltyic Degradation of a Chemical Warfare Agent Simulant: Reaction Mechanisms on TiO_2-Supported Au Nanoparticles. *Journal of Physical Chemistry C* **2008**, *112*, 7496-7502.
(46) Ratliff, J. S.; Tenney, S. A.; Hu, X.; Conner, S. F.; Ma, S.; Chen, D. A. Decomposition of Dimethyl Methylphosphonate on Pt, Au, and Au-Pt Clusters Supported on TiO_2 (110). *Langmuir* **2009**, *25*, 216-225.
(47) Haruta, M. When Gold is Not Noble: Catalysis by Nanoparticles. *Chemical Record* **2003**, *3*, 75-87.
(48) Haruta, M.; Tsubota, S.; Kobayashi, T.; Kageyama, H.; Genet, M. J.; Delmon, B. Low-Temperature Oxidation of CO over Gold Supported on TiO_2, alpha-Fe_2O_3, and Co_3O_4. *Journal of Catalysis* **1993**, *144*, 175-192.
(49) Chen, M.; Goodman, D. W. Catalytically Active Gold: From Nanoparticles to Ultrahin Films. *Accounts of Chemical Research* **2006**, *39*, 739-746.
(50) Baier, R. W.; Weller, S. W. Catalytic and Thermal Decomposition of Isopropyl Methyl Fluorophosphate. *Industrial and Engineering Chemistry Process Design and Development* **1967**, *6*, 380-385.
(51) Paddle, B. M. Biosensors for Chemical and Biological Agents of Defense Interest. *Biosensors & Bioelectronics* **1996**, *11*, 1079-1113.
(52) Yaroslavsky, N. G. *Zh. Fiz. Khim.* **1950**, *24*, 68.
(53) Pimental, G. C.; McClellan, M. L. *The Hydrogen Bond*; W.F. Freeman: San Francisco, 1960.
(54) Zhuravlev, L. T. The Surface Chemistry of Amorphous Silica. Zhuravlev Model. *Colloids and Surfaces A* **2000**, *173*, 1-38.
(55) Morrow, B. A.; McFarlan, A. J. Infrared and Gravimetric Study of an Aerosil and a Precipitated Silica Using Chemical and Hydrogen/Deuterium Exchange Probes. *Langmuir* **1991**, *7*, 1695-1701.

(56) Morrow, B. A.; Cody, I. A. Infrared Studies of Reactions on Oxide Surfaces. 6. Active Sites on Dehydroxylated Silica for the Chemisorption of Ammonia and Water. *Journal of Physical Chemistry* **1976**, *80*, 1998-2004.
(57) Morrow, B. A.; Cody, I. A.; Lee, L. S. M. Infrared Studies of Reactions on Oxide Surfaces. 7. Mechanism of the Adsorption of Water and Ammonia on Dehydroxylated Silica. *Journal of Physical Chemistry* **1976**, *80*, 2761-2767.
(58) West, R.; Barney, R. H. Hydrogen Bonding Studies. II. The Acidity and Basicity of Silanols Compared to Alcohols. *Journal of the American Chemical Society* **1959**, *81*, 6145-6148.
(59) Klier, K.; Zettlemoyer, A. C. Water at Interfaces: Molecular Structure and Dynamics. *Journal of Colloid and Interface Science* **1977**, *58*, 216-229.
(60) Taylor, D. E.; Runge, K.; Cory, M. G.; Burns, D. S.; Vasey, J. L.; Hearn, J. D.; Henley, M. V. Binding of Small Molecules to a Silica Surface: Comparing Experimental and Theoretical Results. *Journal of Physical Chemistry C* **2011**, *115*, 24734-24742.
(61) Borello, E.; Zecchina, A.; Morterra, C.; Ghiotti, G. Infrared Study of Methanol Adsorption on Aerosil. II. Physical Adsorption at Room Temperature. *Journal of Physical Chemistry* **1967**, *71*, 2945-2951.
(62) McDonald, R. S. Study of the Interaction between Hydroxyl Groups of Aerosil Silica and Adsorbed Non-polar Molecules by Infrared Spectrometry. *Journal of the American Chemical Society* **1957**, *79*, 850-854.
(63) Curthoys, G.; Davydov, V. Y.; Kiselev, A. V.; Kiselev, S. A.; Kuznetsov, B. V. Hydrogen Bonding in Adsorption on Silica. *Journal of Colloid and Interface Science* **1974**, *48*, 58-72.
(64) Galkin, G. A.; Kiselev, A. V.; Lygin, V. I. *Russian Journal of Physical Chemistry* **1967**, *41*, 20.
(65) Moore, J. H.; Davis, C. C.; Coplan, M. A. *Building Scientific Apparatus*; 3 ed.; Perseus Books: Cambridge, MA, 2003.
(66) Uzarski, J. Reflection Absorption Infrared Spectroscopic Studies of Surface Chemistry Relevant to Chemical and Biological Warfare Agent Defense. Virginia Polytechnic Institute and State University, 2009.
(67) Panayotov, D. A.; John T. Yates, J. Spectroscopic Detection of Hydrogen Atom Spillover from Au Nanopaticles Supported on TiO_2: Use of Conduction Band Electrons. *Journal of Physical Chemistry C* **2007**, *111*, 2959-2964.
(68) Fiegland, L. R.; Ultrahigh Vacuum Studies of the Reaction Mechanisms of Ozone with Saturated and Unsaturated Self-Asembled Monolayers. Virginia Polytechnic Institute and State University, 2008.
(69) Vansant, E. F.; Voort, P. V. D.; Vrancken, K. C. *Characterization and Chemical Modification of the Silica Surfaces*; Elsevier: New York, 1995; Vol. 93.
(70) Kanan, S. M.; Tripp, C. P. Prefiltering Strategies for Metal Oxide Based Sensors: The Use of Chemical Displacers to Selectively Dislodge Adsorbed Organophosphonates from Silica Surfaces. *Langmuir* **2002**, *18*, 722-728.
(71) Uzarski, J. Reflection Absorption Infrared Spectroscopic Studies of Surface Chemistry Relevant to Chemical and Biological Warfare Agent Defense. Virginia Polytechnic Institute and State University, 2009.
(72) Quenneville, J.; Taylor, R. S.; van Duin, A. C. T. Reactive Molecular Dynamics Studies of DMMP Adsorption and Reactivity on Amorphous Silica Surfaces. *Journal of Physical Chemistry C* **2010**, *114*, 18894-18902.

(73) Nadler, M. P.; Nissan, R. A.; Hollins, R. A. FT-IR and FT-NMR Study of Organophosphorus Surface Reactions. *Applied Spectroscopy* **1988**, *42*, 634-642.
(74) Zubkov, T.; Smith, R. S.; Engstrom, T. R.; Kay, B. D. Adsorption, Desorption, and Diffusion of Nitrogen in a Model Nanoporous Material. II. Diffusion Limited Kinetics in Amorphous Solid Water. *Journal of Chemical Physics* **2007**, *127*, 184708.
(75) Buccuzzi, F.; Coluccia, S.; Ghiotti, G.; Morterra, C.; Zecchina, A. Infrared Study of Surface Modes on Silica. *Journal of Physical Chemistry* **1978**, *82*, 1298-1303.
(76) Tripp, C. P.; Hair, M. L. Reaction of Chlromethylsilanes with Silica: A Low-Frequency Infrared Study. *Langmuir* **1991**, *7*, 923-927.
(77) Wilmsmeyer, A. R.; Uzarski, J.; Barrie, P. J.; Morris, J. R. Interactions and Binding Energies of Dimethyl Methylphosphonate and Dimethyl Chlorophosphate with Amorphous Silica. *Langmuir* **2012**, *28*, 10962-10967.
(78) Schuster, P.; Zundel, G.; Sandorfy, C. *The Hydrogen Bond: Recent Developments in Theory and Experiment*; American Elsevier: New York, 1976; Vol. 3.
(79) Crooks, R. M.; Yang, H. C.; McEllistrem, L. J.; Thomas, R. C.; Ricco, A. J. Interactions between Self-Assembled Monolayers and an Organophosphonate. Detailed Study using Surface Acoustic Wave-Based Mass Analysis, Polarization Modulation-FTIR Spectroscopy and Ellipsometry. *Faraday Discussions* **1997**, *107*, 285-305.
(80) Badger, R. M.; Bauer, S. H. Spectroscopic Studies of the Hydrogen Bond. II. The Shift of the O-H Vibrational Frequency in the Formation of the Hydrogen Bond. *Journal of Chemical Physics* **1937**, *5*, 839-851.
(81) Redhead, P. A. *Vacuum* **1962**, *12*, 203.
(82) Sanchez, J. R.; Aldao, C. M. Monte Carlo Study of Thermal Desorption Curves of Water from Zeolite Type A. *Langmuir* **1996**, *12*, 36-39.
(83) Gorte, R. J. Design Parameters for Temperature Programmed Desorption from Porous Catalysts. *Journal of Catalysis*. **1982**, *75*, 164-174.
(84) Palmero, A.; Aldao, C. M. Readsorption and Diffusion-Limited TPD of Water from Zeolite Linde 4A. *Thermochimica Acta* **1998**, *319*, 177-184.
(85) Palmero, A.; Loffler, D. G. Kinetics of Water Desorption from Pelletized 4A and 5A Zeolites. *Thermochimica Acta* **1990**, *159*, 171-176.
(86) Dean, J. A. *Lange's Handbook of Chemistry*; Fifteenth Edition ed.; McGraw-Hill Handbooks, 1998.
(87) Panayotov, D.; J.T. Yates, J. Bifunctional Hydrogen Bonding of 2-Chloroethyl Ethyl Sulfide on TiO_2-SiO_2 Powders. *Journal of Physical Chemistry B* **2003**, *107*, 10560-10564.
(88) Saxena, A.; Srivastava, A. K.; Sign, B.; Goyal, A. Removal of Sulphur Mustard, Sarin and Simulants on Impregnated Silica. *Journal of Hazardous Materials* **2012**, *211-212*, 226-232.
(89) Cheng, Y.; Huang, Y.; Alexander, K.; Dollimore, D. A Thermal Analysis Study of Methyl Salicylate. *Thermochimica Acta* **2001**, *367*, 23-28.
(90) Pauwels, J.; D'Autry, W.; Bossche, L. V. d.; Dewever, C.; Forier, M.; Vanderwaeyenberg, S.; Wolfs, K.; Hoogmartens, J.; Schepdael, A. V.; Adams, E. Optimization and Validation of Liquid Chromatography and Headspace-Gas Chromatography Based Methods for the Quantitative Determination of Capsaicinoids, Salicylic Acid, Glycol Monosalicylate, Methyl Salicylate, Ethyl Salicylate, Camphor and L-Menthol in a Topical Formulation. *Journal of Pharmaceutical and Biomedical Analysis* **2012**, *60*, 51-58.
(91) Hertl, W.; Hair, M. L. Hydrogen Bonding between Adsorbed Gases and Surface Hydroxyl Groups on Silica. *Journal of Physical Chemistry* **1968**, *72*, 4676-4682.

(92) Sosa, C.; Bartlett, R. J.; KuBulat, K.; Person, W. B. A Theoretical Study of the Harmonic Vibrational Frequencies and Infrared Intensities of XCH2CH2SCH2CH2X and XCH2CH2SH (X=H, Cl). *Journal of Physical Chemistry* **1989**, *93*, 577-588.
(93) Stout, S. C.; Larsen, S. C.; Grassian, V. H. Adsorption, Desorption and Thermal Oxidation of 2-CEES on Nanocrystalline Zeolites. *Microporous and Mesoporous Materials* **2007**, *100*, 77-86.
(94) Rieck, J. S.; Bell, A. T. Influence of Adsorption and Mass Transfer Effects on Temperature-Programmed Desorption from Porous Catalysts. *Journal of Catalysis* **1984**, *85*, 143-153.
(95) Kanervo, J. M.; Keskitalo, T. J.; Slioor, R. I.; Krause, A. O. I. Temperature-Programmed Desorption as a Tool to Extract Quantitative Kinetic or Energetic Information for Porous Catalysts. *Journal of Catalysis* **2006**, *238*, 382-393.
(96) Muhler, M.; Rosowski, F.; Ertl, G. The Dissociative Adsorptoin of N_2 on a Multiply Promoted Iron Catalyst Used for Ammonia Synthesis: A Temperature Programmed Desorption Study. *Catalysis Letters* **1994**, *24*, 317-331.
(97) Varghese, H. T.; Panicker, C. Y.; Philip, D.; Mannekutla, J. R.; Inamdar, S. R. IR, Raman and SERS Studies of Methyl Salicylate. *Spectrochimica Acta Part A: Molecular Spectroscopy* **2007**, *66*, 959-963.
(98) Radhi, M. M.; El-Bermani, M. F. Infrared Studies of the Conformation in Salicyladehyde, Methylsalicylate and Ethylsalicylate. *Spectrochimica Acta Part A: Molecular Spectroscopy* **1990**, *46*, 33-42.
(99) Phole, W. Infrared Study of the Adsorption of Aromatic Molecules onto Silica and Chlorinated Silica. Application of the Charge-Transfer Theory to the Data. *Journal of the Chemical Society, Farady Transactions* **1982**, *78*, 2101-2109.
(100) Chen, H. W.; Chen, C. S.; Harn, S. J. Infrared and Temperature-Programmed Desorption Study of Acetophenone on Pd/SiO_2. *Journal of Physical Chemistry* **1995**, *99*, 10557-10564.
(101) Anderson, J. H.; Lombarid, J.; Hair, M. L. The Influence of Hydroxyl Groups on the Ultraviolet Spectra of Substituted Aromatic Molecules Adsorbed on Silica Surfaces. *Journal of Colloid and Interface Science* **1975**, *50*, 519-524.
(102) Fisher, G. L.; Meserole, C. A. Design for a Kinematic, Variable Flux Microcapillary Array Molecular Beam Doser. *Journal of Vacuum Science and Technology A* **2005**, *23*, 722-724.